

HIGHWAY RESEARCH RECORD

Number | Highway Soils Engineering
345 | 11 Reports

Subject Areas

25	Pavement Design
61	Exploration-Classification (Soils)
62	Foundations (Soils)
63	Mechanics (Earth Mass)

HIGHWAY RESEARCH BOARD

DIVISION OF ENGINEERING NATIONAL RESEARCH COUNCIL
NATIONAL ACADEMY OF SCIENCES—NATIONAL ACADEMY OF ENGINEERING

WASHINGTON, D.C.

1971

ISBN 0-309-01956-7

Price: \$3.80

Available from

Highway Research Board
National Academy of Sciences
2101 Constitution Avenue
Washington, D.C. 20418

GROUP 2—DESIGN AND CONSTRUCTION OF TRANSPORTATION FACILITIES

John L. Beaton, California Division of Highways, Sacramento, chairman

SECTION K—SOIL MECHANICS

Carl L. Monismith, University of California, Berkeley, chairman

John W. Guinnee, Highway Research Board staff

Committee 1—Strength and Deformation Characteristics of Pavement Sections

John A. Deacon, University of Kentucky, Lexington, chairman

Richard D. Barksdale, B. E. Colley, Hsai-Yang Fang, Frank L. Holman, Jr., W. Ronald Hudson, Melvin H. Johnson, Bernard F. Kallas, William J. Kenis, Wolfgang G. Knauss, Milan Krukar, H. G. Larew, Fred Moavenzadeh, Carl L. Monismith, William M. Moore, Keshavan Nair, Eugene L. Skok, Jr., Ronald L. Terrel

Committee 2—Embankments and Earth Slopes

Lyndon H. Moore, N. Y. State Department of Transportation, Albany, chairman

Philip P. Brown, Raymond A. Forsyth, David S. Gedney, Wilbur M. Haas, C. W. Heckathorn, Raymond C. Herner, Wm. P. Hofmann, Henry W. Janes, Martin S. Kapp, Philip Keene, Richard E. Landau, Ivan C. MacFarlane, Harry E. Marshall, Glen L. Martin, Melvin W. Morgan, Robert L. Schuster, Robert T. Tierney, David J. Varnes, Walter C. Waidelich, William G. Weber, Jr.

Committee 4—Subsurface Soil-Structure Interaction

Ernest T. Selig, State University of New York, Buffalo, chairman

Jay R. Allgood, Mike Bealey, Bernard E. Butler, T. Y. Chu, T. F. deCapiteau, Kenneth S. Eff, L. H. Gabriel, Delon Hampton, D. A. Linger, F. Dwayne Nielson, Harry H. Ulery, Jr., Reynold K. Watkins, Howard L. White

Committee 5—Mechanics of Earth Masses and Layered Systems

Russell A. Westmann, University of California, Los Angeles, chairman

Richard G. Ahlvin, Richard D. Barksdale, A. A. Fungaroli, Delon Hampton, Milton E. Harr, R. L. Kondner, Raymond J. Krizek, Fred Moavenzadeh, Keshavan Nair, Robert L. Schiffman, Frank H. Scrivner, Robert D. Stoll, Aleksandar S. Vesic, Harvey E. Wahls, William G. Weber, Jr.

SECTION L—SOIL AND ROCK PROPERTIES AND GEOLOGY

L. F. Erickson, Idaho Department of Highways, Boise, chairman

Committee 2—Soil and Rock Properties

William H. Perloff, Purdue University, Lafayette, Indiana, chairman

John W. Guinnee, Highway Research Board staff

William F. Brumund, Richard W. Christensen, George B. Clark, Wilbur I. Duvall, Charles L. Emery, Emmericus C. W. A. Geuze, Bernard B. Gordon, James P. Gould, Ernest Jonas, Robert L. Kondner, Charles C. Ladd, G. A. Leonards, Vladimir Obrcian, Shailer S. Philbrick, Gerald P. Raymond, Hassan A. Sultan, Harvey E. Wahls, T. H. Wu

FOREWORD

The first five papers of this RECORD deal with the information necessary to help perfect our concept of pavement action, reaction, and performance and to provide that which is helpful to all who are interested in the structural design and performance of a roadway. Huang, Hicks and Monismith, and Barksdale present concepts of criteria using deflection and curvature, resilient response, and dynamic pulse times. Elliott and Moavenzadeh present a highly theoretical approach to the analysis of stress and displacements, while Chou makes a valuable contribution in pointing up the difference between stresses and displacements under assumed and actual tire pressures.

A new method involving a double punch test is described by Fang and Chen for determining the tensile strength of soils. Fundamental relationships are developed and comparisons with other tensile tests are discussed.

Kay and Krizek apply probability functions to uncertainty considerations and cost considerations to obtain a rational procedure for determining safety factors associated with the bearing capacity of cohesive soils.

Practical "chart" solutions for slope stability problems have been compiled by Hunter and Schuster. These cover a wide variety of conditions and can be used in rapid investigation of preliminary designs.

The papers by Hall and Smith and by Smith and Kleiman are a series covering the special design of a 383-ft-high earth embankment and its subsequent behavior. A comparison of design strength values with "as-built" strength values is presented.

Green determines stress distribution around circular tunnels using a conformal mapping technique that applies complex variables to this special stress analysis problem.

CONTENTS

DEFLECTION AND CURVATURE AS CRITERIA FOR FLEXIBLE PAVEMENT DESIGN AND EVALUATION

Y. H. Huang	1
Discussion	
N. K. Vaswani.	12
Closure	14

FACTORS INFLUENCING THE RESILIENT RESPONSE OF GRANULAR MATERIALS

R. G. Hicks and C. L. Monismith.	15
--	----

COMPRESSIVE STRESS PULSE TIMES IN FLEXIBLE PAVEMENTS FOR USE IN DYNAMIC TESTING

Richard D. Barksdale	32
--------------------------------	----

ANALYSIS OF STRESSES AND DISPLACEMENTS IN THREE-LAYER VISCOELASTIC SYSTEMS

J. F. Elliott and F. Moavenzadeh.	45
---	----

STRESSES AND DISPLACEMENTS IN AN ELASTIC MASS UNDER ASSUMED AND MEASURED TIRE PRESSURES

Y. T. Chou	58
----------------------	----

NEW METHOD FOR DETERMINATION OF TENSILE STRENGTH OF SOILS

H. Y. Fang and W. F. Chen	62
-------------------------------------	----

PROBABILISTIC APPROACH TO THE DETERMINATION OF SAFETY FACTORS FOR THE BEARING CAPACITY OF COHESIVE SOILS

J. Neil Kay and Raymond J. Krizek.	69
--	----

CHART SOLUTIONS FOR ANALYSIS OF EARTH SLOPES

John H. Hunter and Robert L. Schuster	77
---	----

SPECIAL TESTS FOR DESIGN OF HIGH EARTH EMBANKMENTS ON US-101

Earl B. Hall and Travis Smith	90
---	----

BEHAVIOR OF HIGH EARTH EMBANKMENT ON US-101

Travis Smith and William F. Kleiman	100
---	-----

DETERMINATION OF STRESS DISTRIBUTION AROUND CIRCULAR TUNNELS USING CONFORMAL MAPPING TECHNIQUE

William E. Green	111
----------------------------	-----

DEFLECTION AND CURVATURE AS CRITERIA FOR FLEXIBLE PAVEMENT DESIGN AND EVALUATION

Y. H. Huang, University of Kentucky

The excessive plastic deformation of the subgrade and the fatigue cracking of asphalt surfaces are two major causes of pavement failures. One of the methods to preclude such failures is to consider the pavement as a three-layer elastic system by limiting the vertical compressive strain on the surface of the subgrade and the horizontal tensile strain at the bottom of the asphalt-bound layer. The disadvantage of this method is that these strains cannot be easily measured in the field, so the adequacy of the method cannot be properly evaluated. The purpose of this study is to find the relationships among deflection, curvature, compressive strain on the subgrade, and tensile strain in the asphalt layer so that deflection and curvature, instead of compressive and tensile strains, can be used as criteria for pavement design and evaluation. These relationships are expressed as dimensionless ratios and presented in tabular forms. The application of these tables to pavement design and evaluation is illustrated. The study shows that, for thinner pavements, curvature is a better indicator of the compressive strain on the subgrade and, for thicker pavements, deflection is the better indicator. The tensile strain in the asphalt layer is related to the curvature and the thickness of the asphalt layer, essentially independent of the thickness of untreated base courses and the properties of paving materials.

•THE application of rational methods to flexible pavement design and evaluation has received a great deal of attention in recent years. One of the methods that has been used most frequently is the three-layer linear elastic theory originally developed by Burmister (1). It is generally agreed that pavement behavior under the repeated application of transient wheel loads is essentially linearly elastic in the sense that the deflection is not only nearly proportional to the wheel load but also almost completely recoverable after each load application. Comparisons of the stresses and strains computed by the layered theory with those measured in prototype pavements, as undertaken by Whiffin and Lister (2) in England, Gusfeldt and Dempwolf (3) in West Germany, and Klomp and Niesman (4) and Nijboer (5) in The Netherlands, have more or less indicated the validity of the theory. If the stresses and strains in a pavement can be predicted theoretically, it is possible to design the pavement so that the stresses and strains at certain critical points will not exceed the allowable values. This rational method has long been used for the design of structures and has also been recommended recently by Shell International Petroleum for the design of flexible pavements.

In the design and evaluation of pavements, two major modes of failure must be considered, namely, rutting and fatigue. Rutting is due to permanent deformations in the pavement, particularly in the subgrade, resulting from a combination of consolidation and shear failure. There are no rational methods of practical significance for predicting the rut depth or the magnitude of permanent deformations. However, by keeping the stresses and strains on the surface of the subgrade to a low level, rut depth can be

reduced to a tolerable limit so that it will neither cause the pavement to crack nor seriously impair its riding quality. Fatigue is caused by the repetitive application of wheel loads that induce fluctuating stresses and strains in the asphalt layer. Laboratory investigations of asphalt mixtures under bending stresses show that under a given number of load repetitions there exists a limiting tensile strain below which fatigue will not occur (6, 7). If this limiting strain under a given number of load repetitions can be determined in the laboratory, it is possible to design the pavement so that the maximum tensile strain at the bottom of the asphalt layer will not exceed the limiting value.

Peatti (8) suggested the use of the vertical compressive stress on the surface of the subgrade in conjunction with the horizontal tensile strain at the bottom of the asphalt layer as the two design criteria for flexible pavements. A relationship between the permissible value of the vertical stress on the subgrade and the CBR value of the soil was developed from an analysis of road structures known to be satisfactory in practice. He indicated that a relationship connecting the vertical strain at the top of the subgrade with the CBR value of the soil might also be derived, and that designs based on vertical strain as a criterion would be very similar to those developed from the vertical stress criterion. Skok and Finn (9) used the three-layer elastic theory to compute the maximum vertical stress on the subgrade and the maximum horizontal tensile stress and strain in the asphalt layer of the AASHO and WASHO test roads. They found that the rut depth and pavement serviceability were closely related to the vertical stress, and that the initial occurrence of cracking was related to the maximum horizontal stress and strain. Dorman (10) analyzed the U.S. Corps of Engineers CBR design charts and found that, irrespective of the construction, the allowable vertical compressive strain on the surface of the subgrade was practically a constant. Later, in cooperation with Metcalf (11), he developed a series of design charts based on the consideration of the vertical compressive strain on the subgrade and the horizontal tensile strain at the bottom of the asphalt layer. The permissible compressive strain on the subgrade, corresponding to a given number of equivalent 18,000-lb axle load applications, was obtained from an empirical correlation with the results of the AASHO Road Test, and the permissible tensile strain of the asphalt layer was obtained from laboratory fatigue data.

The foregoing literature review, even though quite brief, clearly indicates that the use of three-layer elastic theory by limiting the vertical compressive strain on the subgrade and the horizontal tensile strain at the bottom of the asphalt layer is a valid method of pavement design. However, the specification of these strains as design criteria suffers from the disadvantage that they cannot be easily measured in the field. It is desirable to use the surface deflection or curvature as the design criterion, rather than the vertical strain on the surface of the subgrade and the horizontal strain at the bottom of the asphalt layer, because the surface deflection and curvature can be easily measured. This is particularly true in the evaluation of existing pavements. If the relationships among deflection, curvature, compressive strain on the subgrade, and tensile strain in the asphalt layer under a design wheel load can be established theoretically, the permissible deflection or curvature corresponding to any given permissible compressive and tensile strains can then be determined. It is the purpose of this paper to investigate these relationships and present them in tabular forms. The application of these tables to the practical design and evaluation of flexible pavements is also presented.

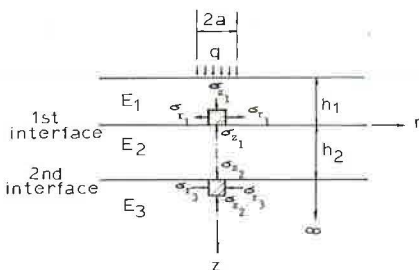


Figure 1. Three-layer elastic system.

DESCRIPTION OF METHOD

In the analysis, the pavement is considered a three-layer elastic system (Fig. 1). Layer 1, which is composed of asphalt-treated surface, binder, and base courses, has a thickness h_1 and an average modulus of elasticity E_1 . Layer 2, which consists of untreated granular base and subbase courses, has a thickness h_2 and an average modulus E_2 . These two layers are placed on a subgrade of infinite thickness with a modulus of elasticity E_3 . A Poisson's ratio of

0.5 is assumed for all three layers. As is usually done in pavement design, it has been assumed that a wheel load having a uniform pressure q is applied on the surface over a circular area of radius a . In the discussions that follow, the surface course includes all the asphalt-treated courses on the upper portion of a pavement, while the base course refers to the untreated granular base and subbase only.

The maximum vertical compressive strain on the subgrade and the maximum horizontal tensile strain at the bottom of layer 1 occur at the axis of symmetry and can be determined by Eqs. 1 and 2 respectively.

$$\epsilon_z = \frac{q(\sigma_{z_2} - \sigma_{r_3})}{E_3} \quad (1)$$

$$\epsilon_r = \frac{q(\sigma_{z_1} - \sigma_{r_1})}{2E_1} \quad (2)$$

where

ϵ_z = vertical strain on the surface of the subgrade, or layer 3;

ϵ_r = horizontal strain at the bottom of layer 1;

q = applied pressure;

E_1 and E_3 = moduli of elasticity of layers 1 and 3 respectively;

σ_{z_1} and σ_{z_2} = vertical stress factors at the first and second interfaces respectively (Fig. 1); and

σ_{r_1} and σ_{r_3} = interface radial stress factors for layers 1 and 3 respectively.

Values of $\sigma_{z_2} - \sigma_{r_3}$ and $\sigma_{z_1} - \sigma_{r_1}$ can be obtained from Jones's tables (12).

Because values of surface deflections for a Poisson's ratio of 0.5 are not available, a computer program was developed for determining the surface deflections at the center of the loaded area as well as at other radial distances from the center. The surface deflection can be determined from Eq. 3.

$$w = \frac{qa}{E_3} F_w \quad (3)$$

where

w = surface deflection;

a = radius of loaded area; and

F_w = deflection factor, which can be determined from Eq. 3a.

$$F_w = \frac{1.5}{\left(\frac{E_1}{E_2}\right)\left(\frac{E_2}{E_3}\right)} \int_0^\infty J_0(mr) J_1(ma) \left[\frac{\text{Numerator}}{\text{Denominator}} \right] \frac{dm}{m} \quad (3a)$$

where

r = radial distance at which deflection is computed;

m = a parameter of integration; and

J_0 and J_1 = Bessel functions of the first kind, order 0 and 1 respectively.

The expressions for the numerator and denominator are functions of the thickness and modulus of each layer as well as the parameter m . They can be found in Burmister's original paper (1) and elsewhere (13). Because the expressions are quite long, they are not presented here. To compute the maximum deflection, r can be set to zero or $J_0(mr)$ to 1.

The infinite integral in Eq. 3a was evaluated numerically using Gaussian quadratures. The zeros of one of the Bessel functions were found, and the integration between two zeros was carried out using an 8-point formula. It was found that when h_1/a or h_2/a was relatively large, the integrand diminished very rapidly and the use of an 8-point formula could not give the desired precision. For this reason, a 32-point formula was employed for the first interval of integration and the 8-point formula for all subsequent intervals. The integration was continued until the deflection converged to a specified tolerance.

The curvature can be determined from the differential deflection, Δ , for a given chord length, l . When $l = 2a$, as has been assumed in preparing the tables in the Appendix, the differential deflection can be determined by

$$\Delta = \frac{qa}{E_3} F_C \quad (4)$$

where

$$F_C = \frac{1.5}{\left(\frac{E_1}{E_2}\right)\left(\frac{E_2}{E_3}\right)} \int_0^\infty [1 - J_0(ma)] \left[\frac{\text{Numerator}}{\text{Denominator}} \right] \frac{dm}{m} \quad (4a)$$

It is generally assumed that the deflection profile is a sine curve, so the maximum curvature is

$$\frac{1}{R} = \frac{\pi^2 \Delta}{l^2} \quad (5)$$

Combining Eqs. 4 and 5, and letting $l = 2a$, we get

$$a \left(\frac{1}{R} \right) = \frac{\pi^2 q}{4E_3} F_C \quad (6)$$

To determine the relationships among deflection, curvature, compressive strain on the subgrade, and tensile strain in the asphalt layer, the following dimensionless ratios were used:

$$\frac{w}{a^2 \left(\frac{1}{R} \right)} = \text{deflection-curvature ratio} = \frac{4}{\pi^2} \frac{F_W}{F_C} \quad (7a)$$

$$\frac{w}{a \epsilon_z} = \text{deflection-compressive strain ratio} = \frac{F_W}{\sigma_{z_2} - \sigma_{r_3}} \quad (7b)$$

$$\frac{a \left(\frac{1}{R} \right)}{\epsilon_z} = \text{curvature-compressive strain ratio} = \frac{\pi^2}{4} \frac{F_C}{\sigma_{z_2} - \sigma_{r_3}} \quad (7c)$$

$$\frac{w}{a \epsilon_r} = \text{deflection-tensile strain ratio} = \frac{2F_W}{\sigma_{z_1} - \sigma_{r_1}} \frac{E_1}{E_2} \frac{E_2}{E_3} \quad (7d)$$

$$\frac{a \left(\frac{1}{R} \right)}{\epsilon_r} = \text{curvature-tensile strain ratio} = \frac{\pi^2}{2} \frac{F_C}{\sigma_{z_1} - \sigma_{r_1}} \frac{E_1}{E_2} \frac{E_2}{E_3} \quad (7e)$$

All terms on the right side of Eqs. 7 either are given or can be determined from Eqs. 3a, 4a, or Jones's tables, so these ratios can be computed.

DISCUSSION OF RESULTS

The relationships among deflection, curvature, compressive strain on the subgrade, and tensile strain in the asphalt layer, as expressed by their ratios, are tabulated in the Appendix. In order to save space, not all these ratios are tabulated. Although the deflection-tensile strain ratios are not shown, they can be easily obtained by multiplying the curvature-tensile strain ratios by the deflection-curvature ratios. Also included are the deflection factor, F_w , and the curvature factor, F_c , as determined from Eqs. 3a and 4a respectively.

In the computation, a wide range of thicknesses and modulus ratios was used. The values of h_1/a range from 0.31 to 2.5 and those of h_2/a from 0.63 to 5. The contact radius, a , for a conventional 18,000-lb design axle load is about 6 in., so the thicknesses of the asphalt layer range from 2 to 15 in. and those of the granular bases and subbases from 4 to 30 in. Some values of h_1/a or h_2/a are awkward because of the necessity to match them with values in Jones's tables in which the stresses are given in terms of h_1/h_2 and a/h_2 .

Relationship Between Deflection and Curvature

A study of the deflection-curvature ratios tabulated in the Appendix shows that the ratios generally increase with increasing E_1/E_2 , E_2/E_3 , or h_1/a , indicating that the change in curvature is much more rapid than the change in deflection. In other words, curvature is more sensitive to the change in surface thickness and modulus ratios than to the deflection. Furthermore, the thickness of the untreated base, or layer 2, has practically no effect on the deflection-curvature ratio, as is shown in Figure 2 for a typical case with $E_1/E_2 = 20$ and $E_2/E_3 = 2$. Figure 2 also shows that when the surface is thin, say 2 in. or less, the thickness of surface course has very little effect on deflection-curvature ratios. These theoretical findings are important because they can explain why, under certain circumstances, both deflection and curvature can be used for pavement evaluation with no differences. Dehlen (14) investigated the deflections and curvatures of roads in South Africa and showed that, for the 1- to 2-in. premix surfacings, both deflection and curvature could be used equally well as an indicator of pavement conditions. This conclusion is valid only when the pavements are of the same type with the same materials, the only difference being the thickness of granular base. If the pavements are of different types with a wide variety of surface thickness and modulus ratios, the deflection-curvature ratio will no longer be a constant, and the evaluation based on deflection will surely be different from that based on curvature.

Relation of Compressive Strain to Deflection and Curvature

The relation of the compressive strains on the subgrade to the deflections and curvatures on the surface is quite erratic. The deflection-compressive strain ratios and the curvature-compressive strain ratios vary significantly with the change in thickness and

modulus ratios, and there are no general trends to be traced. For a given permissible compressive strain, the only way to find the corresponding permissible deflection and curvature is to go through the table in the Appendix. When h_2/a is less than or equal to 1.25, which is equivalent to a base course about 8 in. thick, only the curvature-compressive strain ratio, but not the deflection-compressive strain ratio, is tabulated because the former does not change very much with the change in modulus ratios and is, therefore, a better indicator of the compressive strain. It is well-known that the moduli of elasticity of the pavement component layers are quite difficult to determine because they change appreciably

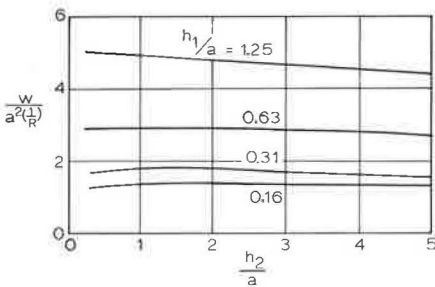


Figure 2. Effect of thickness of deflection-curvature ratio ($E_1/E_2 = 20$, $E_2/E_3 = 2$).

with loading and environment conditions, such as temperature, moisture content, rate of loading, and state of stress. Consequently, a measurement that does not change with the change in modulus ratios is more reliable and should be used whenever possible. When h_2/a is equal to or greater than $2.5a$, the reverse is true; i. e., the deflection is a better indicator of the compressive strain, so the deflection-compressive strain ratio, instead of the curvature-compressive strain ratio, is tabulated.

Relation of Tensile Strain to Deflection and Curvature

A study of the data in the Appendix indicates that both the deflection-tensile strain and the curvature-tensile strain ratios are practically independent of the base course thickness or h_2/a . Therefore, a typical h_2/a of 1.25 can be used to illustrate the factors that affect these ratios.

Figure 3 shows the effect of surface course thickness and modulus ratios on deflection-tensile strain ratios. The deflection-tensile strain ratio increases with increasing E_2/E_3 because of the more rapid decrease in tensile strains at the bottom of the asphalt layer as compared to the decrease in deflections. The effect of E_1/E_2 is erratic when h_1/a is less than 0.6, which is equivalent to a surface course of 4 in. or less. In this practical thickness range, the deflection-tensile strain ratio decreases with the increase in surface course thickness unless E_1/E_2 is exceedingly large. If fatigue is done to excessive tensile strains at the bottom of asphalt layers, for a given permissible tensile strain the permissible deflection should decrease with the increase in surface thickness. This is in agreement with the method used by the California Division of Highways (15) that tolerable deflections to preclude fatigue failures decrease with increasing thickness. However, the strong dependence of the deflection-tensile strain ratio on the modulus ratios indicates that deflection is not a good measure of fatigue.

Figure 4 shows the effect of surface course thickness and modulus ratios on curvature-tensile strain ratios for $h_2/a = 1.25$. Unless E_1/E_2 is exceedingly small, the curvature-tensile strain ratio is practically independent of modulus ratios and varies only with the surface course thickness. This is in conformity with the well-known beam theory that the strain in a beam under pure bending depends only on the curvature and the thickness. However, unlike the beam theory, the strain is not proportional to the thickness because the pavement is considered as a continuum in which the effect of vertical stress is also considered. The independence of the curvature-tensile strain ratio on the modulus ratios indicates that the tensile strain at the bottom of an asphalt layer can be easily determined by measuring the curvature. Knowing the curvature and the thickness of the surface course, the tensile strain can be estimated by using Figure 4.

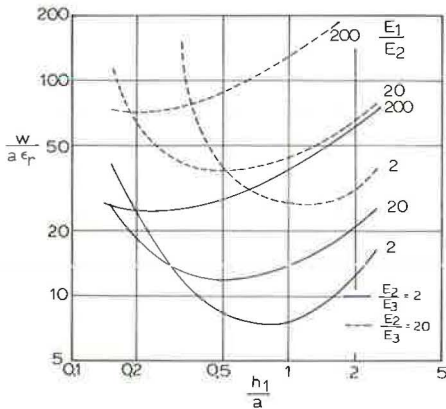


Figure 3. Effect of surface course thickness and modulus ratios on deflection-tensile strain ratio ($h_2/a = 1.25$).

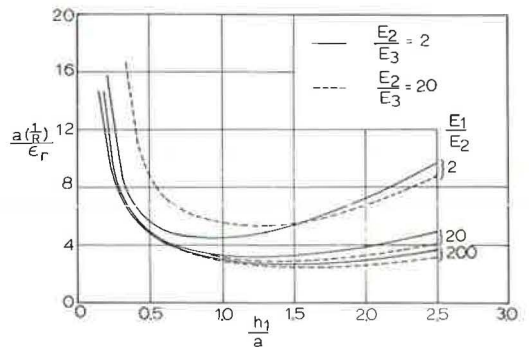


Figure 4. Effect of surface course thickness and modulus ratios on curvature-tensile strain ratio ($h_2/a = 1.25$).

APPLICATIONS TO PAVEMENT DESIGN AND EVALUATION

The data tabulated in the Appendix are based on a single wheel load. If a single wheel load is actually applied to a pavement and the deflection and curvature are measured, the corresponding compressive and tensile strains in the pavement can be determined from the tables. Because the deflection and curvature are generally measured by placing a Benkelman beam (16) or a curvature meter (17, 18) between a set of dual tires, the deflection and curvature thus measured would be somewhat different from those based on a single wheel load. Thus, a correction factor is needed to convert the deflection or curvature based on a single wheel load to that based on a dual wheel load. By simply multiplying the deflection or curvature under a single wheel load by its respective correction factor as tabulated in the Appendix, the corresponding deflection or curvature for a dual wheel load is obtained. The correction factors are based on the three-layer theory by considering each tire having a radius $a/\sqrt{2}$ and spaced at $3a/\sqrt{2}$ apart. The curvature for dual tires is also based on a chord length of $2a$.

Pavement Evaluation

In the evaluation of existing pavements, it is necessary to know the thickness of the surface and base courses and the modulus ratios. The thickness of the pavement components can be measured or obtained from construction records, and the modulus ratios for pavements of conventional types can be reasonably estimated. The Shell vibration machines (19) have been used in various countries for determining the in situ moduli of surface and base courses as well as the subgrade, and typical values have been suggested (7). In pavement evaluation, it is not necessary to know the modulus of each layer; only their ratios are needed. The relationships among deflection, curvature, compressive strain on the subgrade, and tensile strain in the asphalt layer, as expressed by their ratios, can then be determined from the table in the Appendix. Once the deflection and curvature are measured in the field, the corresponding compressive and tensile strains can be computed. By comparing these strains with the permissible strains, the adequacy of the pavement can be evaluated. Table 1 gives the permissible compressive strains on the subgrade and the tensile strains in the asphalt layer corresponding to different equivalent 18,000-lb axle load applications, as suggested by Dormon and Metcalf (11).

For predicting rutting or plastic deformation of the subgrade, it is desirable to measure the deflection and curvature during the summer when the asphalt layer has a smaller modulus and the compressive strain on the subgrade is relatively high; whereas for predicting fatigue, measurements should be made during the winter because the asphalt layer will crack only when the temperature is low. The permissible strains given in Table 1 were determined at low temperatures. However, by conducting the same measurements both in the summer and in the winter, it is possible to establish the correlation between summer and winter measurements so that the deflection and curvature determined during one season can be converted to the other for design and evaluation purposes.

Because the values of h_1/a , h_2/a , E_1/E_2 , and E_2/E_3 in actual cases may not be the same as those tabulated in the Appendix, interpolations of data are usually needed. A three-point Lagrange interpolation formula (20) based on logarithmic scales may be used, or a curve may be plotted through the three given points. As only two points are available for E_2/E_3 , a straight-line interpolation based on logarithmic scales is suggested.

As an illustrative example, suppose an existing pavement having a 4-in. asphalt surface course and an 8-in. untreated base course is to be evaluated. The deflection profile under an 18,000-lb single axle load with dual tires of 80-psi pressure is measured by a Benkelman beam. If the radius

TABLE 1
PERMISSIBLE STRAINS UNDER DIFFERENT
LOAD APPLICATIONS

No. of Load Applications	Compressive Strain on Subgrade	Tensile Strain in Asphalt Layer
10^5	1.05×10^{-3}	2.3×10^{-4}
10^6	6.5×10^{-4}	1.45×10^{-4}
10^7	4.2×10^{-4}	9.2×10^{-5}
10^8	2.6×10^{-4}	5.8×10^{-5}

of curvature determined from the deflection profile for a chord length of 12 in. is 1,000 ft, what are the compressive strain on the subgrade and the tensile strain in the asphalt layer?

First, replace the dual wheel load by a single wheel load with a contact radius of 6 in., so $h_1/a = 0.667$ and $h_2/a = 1.333$. If it is assumed that $E_1/E_2 = 5$ and $E_2/E_3 = 2$, by successive interpolations the following values are obtained: $[a(1/R)]/\epsilon_z = 2.46$, $[a(1/R)]/\epsilon_r = 4.31$, and the correction factor for curvature = 0.62. Converting the radius of curvature to single wheel load, $R = 0.62 \times 1,000 = 620$ ft. Substituting $R = 620$ ft and $a = 0.5$ ft into the above ratios, $\epsilon_z = 3.28 \times 10^{-4}$ and $\epsilon_r = 1.87 \times 10^{-4}$. Compared with the permissible strains in Table 1, it can be concluded that the pavement can sustain more than 10,000,000 load applications without rutting and less than 1,000,000 applications without fatigue. The latter conclusion is obviously not correct because, for predicting fatigue, curvatures must be measured during the winter. If the radius of curvature measured during the winter is 2,000 ft, by assuming $E_1/E_2 = 20$, $E_2/E_3 = 2$ and a correction factor of 0.74, it can be found that $\epsilon_r = 8.2 \times 10^{-5}$, so the pavement can also sustain 10,000,000 applications without fatigue.

Pavement Design

The use of the table in the Appendix for pavement design differs from that for pavement evaluation in two major respects: (a) it is necessary to know the modulus of each layer, not just the modulus ratios, and (b) a trial-and-error process must be employed to determine the thickness of surface and base courses required.

The thickness of surface course is generally governed by fatigue, i. e., by considering the tensile strain at the bottom of the asphalt layer. For ease of illustration, it is assumed that $E_1/E_2 = 200$ and $E_2/E_3 = 2$, so no interpolations of modulus ratios are needed. If $E_3 = 10,000$ psi, $q = 80$ psi, $a = 6$ in., and the permissible tensile strain is 9.2×10^{-5} , the thickness of the surface course can be easily determined.

As a first step, it is assumed that the pavement has the following thickness-radius ratios: $h_1/a = 0.625$ and $h_2/a = 1.25$. From the Appendix, the curvature-tensile strain ratio is 4.01, so $a(1/R) = 4.01 \times 9.2 \times 10^{-5} = 3.69 \times 10^{-4}$, which, when substituted into Eq. 6, results in a permissible curvature factor, F_C , of 0.0187. The actual curvature factor for this design as obtained from the Appendix is 0.0177, which is smaller than the permissible value, and the design is considered satisfactory. It should be noted that the thickness of the base course has only little effect on the thickness of the surface course required.

The thickness of the base course is generally governed by rutting, i. e., by considering the compressive strain on the surface of the subgrade. Using a lower modulus ratio of 20 for E_1/E_3 , the curvature-compressive strain ratio obtained from the Appendix is 1.80. If the permissible compressive strain is 4.2×10^{-4} , the corresponding permissible curvature factor is 0.0383, which is much smaller than the actual value of 0.0856. The design is, therefore, unsatisfactory, and a thicker base course should be used.

Next assume h_2/a to be 2.5. For such a thick base course, it is preferable to use the deflection rather than the curvature as a design criterion. The deflection-compressive strain ratio obtained from the Appendix is 7.92, so $w/a = 7.92 \times 4.2 \times 10^{-4} = 3.326 \times 10^{-3}$, which, when substituted into Eq. 3, results in a permissible deflection factor, F_W , of 0.416. The actual deflection factor for this design is 0.5610, so a still thicker base should be used.

The final design adopted consists of a 4-in. surface course ($h_1/a = 0.667$) and a 20-in. base course ($h_2/a = 3.333$). By proper interpolations of the data in the Appendix, it is found that for $E_1/E_2 = 20$, $w/(a\epsilon_z) = 10.49$, and that for $E_1/E_2 = 200$, $a(1/R)/\epsilon_r = 3.84$. The permissible F_W and F_C are 0.5508 and 0.0179 respectively, which are slightly greater than the actual values of 0.5167 and 0.0148 as determined by interpolations.

This design procedure is very similar to the conventional method of using directly the permissible compressive and tensile strains as design criteria. However, the conversion of strains into deflections and curvatures has the apparent advantage that the latter can be measured in the field, so the method of design can be evaluated.

Although the method presented is based on linear theory, it can also be applied to nonlinear materials if their moduli of elasticity are determined by a method of successive approximations as suggested by Monismith et al. (21). In predicting pavement deflections from laboratory tests, Monismith et al. used a Poisson's ratio of 0.5 for stress computations and 0.35 for deflection computations because these were the only data readily available. The inclusion of the deflection factors in the Appendix is a supplement to Jones's tables and makes available the maximum deflections for a Poisson's ratio of 0.5.

CONCLUSIONS

Based on the three-layer elastic theory, the relationships among deflection, curvature, the compressive strain on the surface of the subgrade, and the tensile strain at the bottom of the asphalt layer, in terms of various dimensionless ratios, are investigated. These dimensionless ratios together with the deflection and curvature factors are presented in tabular forms for a wide range of layer thicknesses and modulus ratios so that the permissible deflection and curvature corresponding to any given permissible compressive and tensile strains can be determined. This makes possible the use of deflection and curvature, instead of compressive and tensile strains, as criteria for pavement design and evaluation. The advantage of using deflection and curvature is that they can be easily measured in the field. The method is particularly suited for the evaluation of existing pavements. By simply measuring the deflection or curvature of a pavement under a given design wheel load, the compressive strain on the surface of the subgrade and the tensile strain at the bottom of the asphalt layer can be estimated. The adequacy of the pavement to carry the design wheel load can be evaluated by comparing the estimated compressive and tensile strains with established permissible values.

A study of the data results in the following conclusions. It should be borne in mind that deflections and curvatures are not exact measurements because they vary a great deal depending on environmental conditions. These conclusions are valid only under general conditions, sometimes in a qualitative sense, and should not be interpreted with exactitude.

1. The deflection-curvature ratio is independent of the base course thickness. The contention that both deflection and curvature can be used equally well as a measure of pavement conditions is valid only when the pavements evaluated are of the general types and composed of the same materials, the only difference being the base course thickness.
2. Curvature is a better indicator of the compressive strain on the subgrade, when the base course is thin, say 10 in. or less. For thicker base courses, deflection is the better indicator.
3. The thickness of base course has very little effect on the deflection-tensile strain ratio, but the thickness of surface course has a tremendous effect. Unless the surface course is exceedingly thick and strong, the deflection-tensile strain ratio decreases with the increase in surface course thickness. If the tensile strain at the bottom of the surface course is a factor controlling fatigue, the permissible deflections should decrease with the increase in surface thickness.
4. Curvature is definitely related to the tensile strain in the asphalt layer. The curvature-tensile strain ratio depends primarily on the surface course thickness, independent of the base course thickness. The use of curvature, instead of deflection, as a criterion for controlling fatigue is highly desirable because the curvature-tensile strain ratios are not affected by the modulus ratios.

ACKNOWLEDGMENTS

Acknowledgment is made to the University of Kentucky Computing Center for the use of the IBM 360 computer and related technical service.

REFERENCES

1. Burmister, D. M. The General Theory of Stresses and Displacements in Layered Soil Systems, III. *Jour. of Applied Physics*, Vol. 16, 1945, pp. 296-302.
2. Whiffin, A. C., and Lister, N. W. The Application of Elastic Theory to Flexible Pavements. *Proc. Internat. Conf. on Structural Design of Asphalt Pavements*, Univ. of Michigan, 1962, pp. 499-521.
3. Gusfeldt, K. H., and Dempwolff, K. R. Stress and Strain Measurements in Experimental Road Sections Under Controlled Loading Conditions. *Proc. Second Internat. Conf. on Structural Design of Asphalt Pavements*, Univ. of Michigan, 1967, pp. 663-669.
4. Klomp, A. J. G., and Niesman, Th. W. Observed and Calculated Strains at Various Depths in Asphalt Pavements. *Proc. Second Internat. Conf. on Structural Design of Asphalt Pavements*, Univ. of Michigan, 1967, pp. 671-688.
5. Nijboer, L. W. Testing Flexible Pavements Under Normal Traffic Loadings by Means of Measuring Some Physical Quantities Related to Design Theories. *Proc. Second Internat. Conf. on Structural Design of Asphalt Pavements*, Univ. of Michigan, 1967, pp. 689-705.
6. Heukelom, W., and Klomp, A. J. G. Dynamic Testing as a Means of Controlling Pavements During and After Construction. *Proc. Internat. Conf. on Structural Design of Asphalt Pavements*, Univ. of Michigan, 1962, pp. 667-679.
7. Heukelom, W., and Klomp, A. J. G. Road Design and Dynamic Loading. *Proc. AAPT*, Vol. 33, 1964, pp. 92-123.
8. Peattie, K. R. A Fundamental Approach to the Design of Flexible Pavements. *Proc. Internat. Conf. on Structural Design of Asphalt Pavements*, Univ. of Michigan, 1962, pp. 403-441.
9. Skok, E. L., and Finn, F. N. Theoretical Concepts Applied to Asphalt Concrete Pavement Design. *Proc. Internat. Conf. on Structural Design of Asphalt Pavements*, Univ. of Michigan, 1962, pp. 412-440.
10. Dorman, G. M. The Extension to Practice of a Fundamental Procedure for the Design of Flexible Pavements. *Proc. Internat. Conf. on Structural Design of Asphalt Pavements*, Univ. of Michigan, 1962, pp. 785-793.
11. Dormon, G. M., and Metcalf, C. T. Design Curves for Flexible Pavements Based on Layered System Theory. *Highway Research Record* 71, 1965, pp. 69-84.
12. Jones, A. Tables of Stresses in Three-Layer Elastic Systems. *HRB Bull.* 342, 1962, pp. 176-214.
13. Ashton, J. E., and Moavenzadeh, F. Analysis of Stresses and Displacements in a Three-Layered Viscoelastic System. *Proc. Second Internat. Conf. on Structural Design of Asphalt Pavements*, Univ. of Michigan, 1967, pp. 209-219.
14. Dehlen, G. L. Flexure of a Road Surfacing, Its Relation to Fatigue Cracking, and Factors Determining Its Severity. *HRB Bull.* 321, 1962, pp. 26-39.
15. Hveem, F. N. Pavement Deflections and Fatigue Failures. *HRB Bull.* 114, 1955, pp. 43-73.
16. Vaswani, N. K. Design of Pavements Using Deflection Equations From AASHO Road Test Results. *Highway Research Record* 239, 1968, pp. 76-92.
17. Dehlen, G. L. A Simple Instrument for Measuring the Curvature Induced in a Road Surfacing by a Wheel Load. *Trans., South Africa Inst. of Civil Engineers*, Sept. 1962, p. 189.
18. Russam, K., and Baker, A. B. Using a Curvature Meter to Measure Transient Deflections of Road Surfaces. *Civil Engineering and Public Works Review*, Nov. 1964, p. 1427.
19. Heukelom, W., and Foster, C. R. Dynamic Testing of Pavements. *Jour. Soil Mech. and Found. Div., ASCE*, Vol. 86, No. SM1, Feb. 1960, pp. 1-28.
20. Salvadori, M. G., and Baron, M. L. *Numerical Methods in Engineering*. Prentice-Hall, 1961, pp. 88.
21. Monismith, C. L., Seed, H. B., Mitry, F. G., and Chang, C. K. Prediction of Pavement Deflections From Laboratory Tests. *Proc. Second Internat. Conf. on Structural Design of Asphalt Pavements*, Univ. of Michigan, 1967, pp. 109-140.

Appendix

DEFLECTION AND CURVATURE AND THEIR RELATION TO COMPRESSIVE AND TENSILE STRAINS

$\frac{h_1}{a}$	$\frac{E_1}{E_2}$	$\frac{E_2}{E_3}$	Deflection		Curvature		$\frac{w}{a^2} \left(\frac{1}{R}\right)$	$\frac{a}{\epsilon_z} \left(\frac{1}{R}\right)$	$\frac{a}{\epsilon_r} \left(\frac{1}{R}\right)$	Deflection		Curvature		$\frac{w}{a^2} \left(\frac{1}{R}\right)$	$\frac{w}{a \epsilon_z}$	$\frac{a}{\epsilon_r} \left(\frac{1}{R}\right)$
			F_w	C.F.*	F_c	C.F.*				F_w	C.F.*	F_c	C.F.*			
0.3125	2	20	$h_2/a = 0.625$						$h_2/a = 2.500$							
			2	1.1829	0.64	0.3519	0.54	1.36	2.02	9.82	0.9103	0.62	0.2714	0.48	1.35	7.73
		20	0.5853	0.86	0.0754	0.71	3.14	1.55	37.60	0.2601	0.86	0.0295	0.52	3.57	10.50	12.51
		2	0.9963	0.75	0.2349	0.68	1.72	1.86	7.45	0.7880	0.74	0.1887	0.64	1.69	7.28	7.21
		20	0.4711	0.91	0.0441	0.79	4.34	1.37	8.44	0.2232	0.90	0.0208	0.66	4.35	10.31	8.12
		200	0.6240	0.88	0.0749	0.80	3.38	1.55	7.34	0.5358	0.88	0.0652	0.78	3.33	7.50	7.31
	200	0.2912	0.95	0.0126	0.81	9.36	1.16	7.60	0.1741	0.95	0.0077	0.56	9.14	11.65	7.58	
	2	20	$h_2/a = 1.250$						$h_2/a = 5.000$							
			2	1.0359	0.64	0.2962	0.51	1.42	2.65	8.75	0.8289	0.59	0.2655	0.47	1.28	22.33
		20	0.3986	0.88	0.0417	0.63	3.87	1.63	37.49	0.1741	0.80	0.0268	0.48	2.86	25.22	8.16
		2	0.8958	0.75	0.2065	0.66	1.76	2.28	7.40	0.7101	0.72	0.1833	0.63	1.57	19.60	7.09
		20	0.3379	0.91	0.0285	0.73	4.80	1.43	8.68	0.1495	0.86	0.0187	0.63	3.51	22.84	7.52
200		0.5920	0.88	0.0704	0.80	3.40	1.59	7.34	0.4754	0.87	0.0622	0.78	3.11	15.48	7.23	
200	0.2453	0.96	0.0102	0.76	9.72	1.02	7.65	0.1133	0.94	0.0065	0.62	8.10	20.97	7.41		
0.6250	2	20	$h_2/a = 0.625$						$h_2/a = 2.500$							
			2	1.0140	0.69	0.2627	0.56	1.56	2.04	5.05	0.8243	0.66	0.2229	0.51	1.50	8.60
		20	0.4530	0.89	0.0443	0.71	4.14	1.39	7.00	0.2324	0.88	0.0238	0.56	3.95	11.64	5.57
		2	0.6587	0.86	0.0914	0.75	2.92	1.54	4.12	0.5610	0.85	0.0801	0.73	2.84	7.92	4.10
		20	0.3060	0.95	0.0146	0.83	8.47	1.09	4.27	0.1819	0.95	0.0091	0.76	8.07	12.51	4.36
		200	0.3443	0.95	0.0181	0.84	7.70	1.22	4.01	0.3206	0.95	0.0171	0.83	7.64	10.31	4.02
	200	0.1565	0.98	0.0026	0.99	24.21	0.93	4.01	0.1259	0.98	0.0021	0.70	24.06	18.85	4.06	
	2	20	$h_2/a = 1.250$						$h_2/a = 5.000$							
			2	0.9178	0.68	0.2365	0.54	1.57	2.83	4.82	0.7552	0.64	0.2186	0.51	1.40	22.72
		20	0.3354	0.90	0.0304	0.64	4.47	1.64	6.94	0.1603	0.83	0.0219	0.52	2.97	23.68	4.70
		2	0.6193	0.86	0.0856	0.74	2.93	1.80	4.12	0.5029	0.84	0.0773	0.72	2.63	16.75	4.05
		20	0.2522	0.95	0.0116	0.80	8.78	1.11	4.38	0.1230	0.93	0.0080	0.72	6.24	21.03	4.21
200		0.3376	0.95	0.0177	0.84	7.71	1.17	4.01	0.2914	0.95	0.0163	0.83	7.23	15.29	4.01	
200	0.1486	0.98	0.0025	0.61	24.54	0.78	4.04	0.0907	0.97	0.0018	0.82	20.53	23.20	4.08		
1.2500	2	20	$h_2/a = 0.625$						$h_2/a = 2.500$							
			2	0.7913	0.71	0.1782	0.51	1.80	2.48	4.57	0.6888	0.69	0.1661	0.48	1.68	10.63
		20	0.3108	0.91	0.0237	0.61	5.32	1.49	4.64	0.1929	0.88	0.0183	0.47	4.28	14.38	5.37
		2	0.3840	0.91	0.0315	0.68	4.94	1.43	3.94	0.3523	0.90	0.0302	0.64	4.72	10.48	3.15
		20	0.1719	0.97	0.0041	0.77	16.86	0.96	2.79	0.1310	0.97	0.0034	0.69	15.48	18.56	3.09
		200	0.1796	0.97	0.0044	0.77	16.50	1.06	2.65	0.1751	0.97	0.0044	0.75	16.23	17.55	2.70
	200	0.0807	0.99	---	---	59.42	0.80	2.49	0.0752	0.99	---	---	58.28	37.24	2.57	
	2	20	$h_2/a = 1.250$						$h_2/a = 5.000$							
			2	0.7441	0.71	0.1711	0.50	1.76	3.48	4.73	0.6387	0.67	0.1639	0.48	1.58	24.20
		20	0.2551	0.90	0.0206	0.53	5.02	1.96	5.33	0.1400	0.84	0.0173	0.44	3.28	26.12	5.08
		2	0.3733	0.91	0.0311	0.65	4.86	1.65	3.12	0.3220	0.90	0.0295	0.63	4.43	17.03	3.17
		20	0.1585	0.97	0.0039	0.70	16.68	0.99	2.92	0.0954	0.96	0.0031	0.64	12.50	25.03	3.20
200		0.1785	0.97	0.0044	0.74	16.36	1.05	2.69	0.1665	0.97	0.0043	0.74	15.75	20.66	2.71	
200	0.0798	0.98	---	---	59.32	0.70	2.53	0.0644	0.99	---	---	54.18	37.63	2.64		
2.5000	2	20	$h_2/a = 0.625$						$h_2/a = 2.500$							
			2	0.6118	0.68	0.1451	0.43	1.71	4.86	9.18	0.5687	0.65	0.1428	0.34	1.61	16.40
		20	0.1966	0.89	0.0156	0.47	5.10	2.57	6.84	0.1463	0.87	0.0136	0.38	4.36	20.55	9.07
		2	0.2176	0.90	0.0168	0.48	5.24	2.38	4.76	0.2079	0.90	0.0153	0.44	5.51	16.65	4.53
		20	0.0913	0.97	0.0018	0.55	20.21	1.50	3.77	0.0816	0.97	0.0016	0.52	20.36	32.25	3.89
		200	0.0926	0.97	0.0018	0.57	20.33	1.64	3.60	0.0917	0.98	0.0017	0.52	21.82	33.58	3.36
	200	0.0411	0.99	---	---	84.08	1.16	3.04	0.0403	0.99	---	---	89.25	82.33	2.88	
	2	20	$h_2/a = 1.250$						$h_2/a = 5.000$							
			2	0.5939	0.68	0.1439	0.49	1.67	6.42	9.68	0.5400	0.63	0.1421	0.33	1.54	31.27
		20	0.1769	0.89	0.0158	0.49	4.52	3.43	8.78	0.1147	0.84	0.0133	0.37	3.50	32.68	9.50
		2	0.2153	0.90	0.0171	0.53	5.09	2.74	4.95	0.1972	0.90	0.0152	0.44	5.27	22.61	4.62
		20	0.0886	0.97	0.0018	0.61	19.51	1.57	4.01	0.0677	0.97	0.0016	0.48	17.48	37.41	4.28
200		0.0924	0.98	0.0019	0.59	20.01	1.67	3.61	0.0900	0.97	0.0017	0.53	21.56	35.41	3.38	
200	0.0411	0.99	---	---	83.58	1.11	3.12	0.0387	0.98	---	---	87.61	75.78	2.97		

* C.F. is the correction factor for dual tires.

Discussion

N. K. VASWANI, Virginia Highway Research Council—Huang's paper is a great step toward the application of theory to practice.

In Virginia we have been evaluating our pavements on the basis of their maximum deflection and spreadability. We define spreadability as a nondimensional quantity as follows:

$$\text{Spreadability} = \frac{d_{\max} + d_1 + d_2 + d_3 + d_4}{5 d_{\max}} \times 100 \text{ percent}$$

where

d_{\max} = maximum deflection of the pavement, and
 d_1, d_2, d_3 and d_4 = the deflections at 1, 2, 3 and 4 ft from the point of the maximum deflection in the deflected basin.

Thus, spreadability as defined here and curvature as defined by the author are inter-related.

Theoretical analyses based on the elastic layered system were carried out in Virginia, and we have determined that if spreadability and maximum deflections were to be considered, the multilayer system could be reduced to a two-layer system consisting of the semi-infinite subgrade and the overlying pavement. The modulus of elasticity of the overlying pavement, for the purpose of practical application, would be the average modulus of elasticity obtained by

$$E_{\text{av}} = \frac{h_1 E_1 + h_2 E_2 + \dots}{h_1 + h_2 + \dots}$$

where

E_{av} = the average modulus of elasticity of the overlying pavement, and
 E_1, E_2, \dots = the moduli of elasticity of the materials in the pavement having thicknesses equal to h_1, h_2, \dots respectively.

The author has theoretically determined that, when the pavements are of different types and with a wide variety of surface thicknesses and modulus ratios, the deflection-curvature ratio is no longer a constant. I have found this to be true in my evaluation of pavements in Virginia on the basis of the deflection-spreadability ratio, and also in my evaluation of the deflection data reported by Scrivner et al. (22). Some examples of the evaluations made in Virginia have been reported (23), and there appears to be a good relationship between the curvature as defined by the author and spreadability as adopted by Virginia.

In this discussion, I present the case of a pavement in southeastern Minnesota. The pavement consisted of a 3-in. layer of asphaltic concrete with 3 in. of crushed rock and 9 in. of sand gravel underneath it. The subgrade soil was a silty clay loam. Figure 5 shows the magnitude of the variation in the ratio of spreadability vs. maximum deflection from December 1966 to August 1967. The temperatures recorded at the top of the pavement during this period varied as follows: December 16, 1966—36 F; February 22, 1967—23 F; March 27, 1967—60 F; April 11, 1967—68 F; and August 8, 1967—93 F.

These temperature data present a picture of the seasonal variations and the hydro-thermal effects on the pavement and the subgrade, and, hence, the variations in the moduli of elasticity of the pavement and the subgrade.

For an understanding of Figure 5, the following points need to be recognized.

1. The modulus of elasticity of the subgrade for any point on the curve could be obtained by extrapolating a coordinate parallel to the coordinate inclined at $\tan^{-1} 0.47$ degrees (Fig. 5). The point at which this extrapolated coordinate hits the base line is the modulus of elasticity of the subgrade.

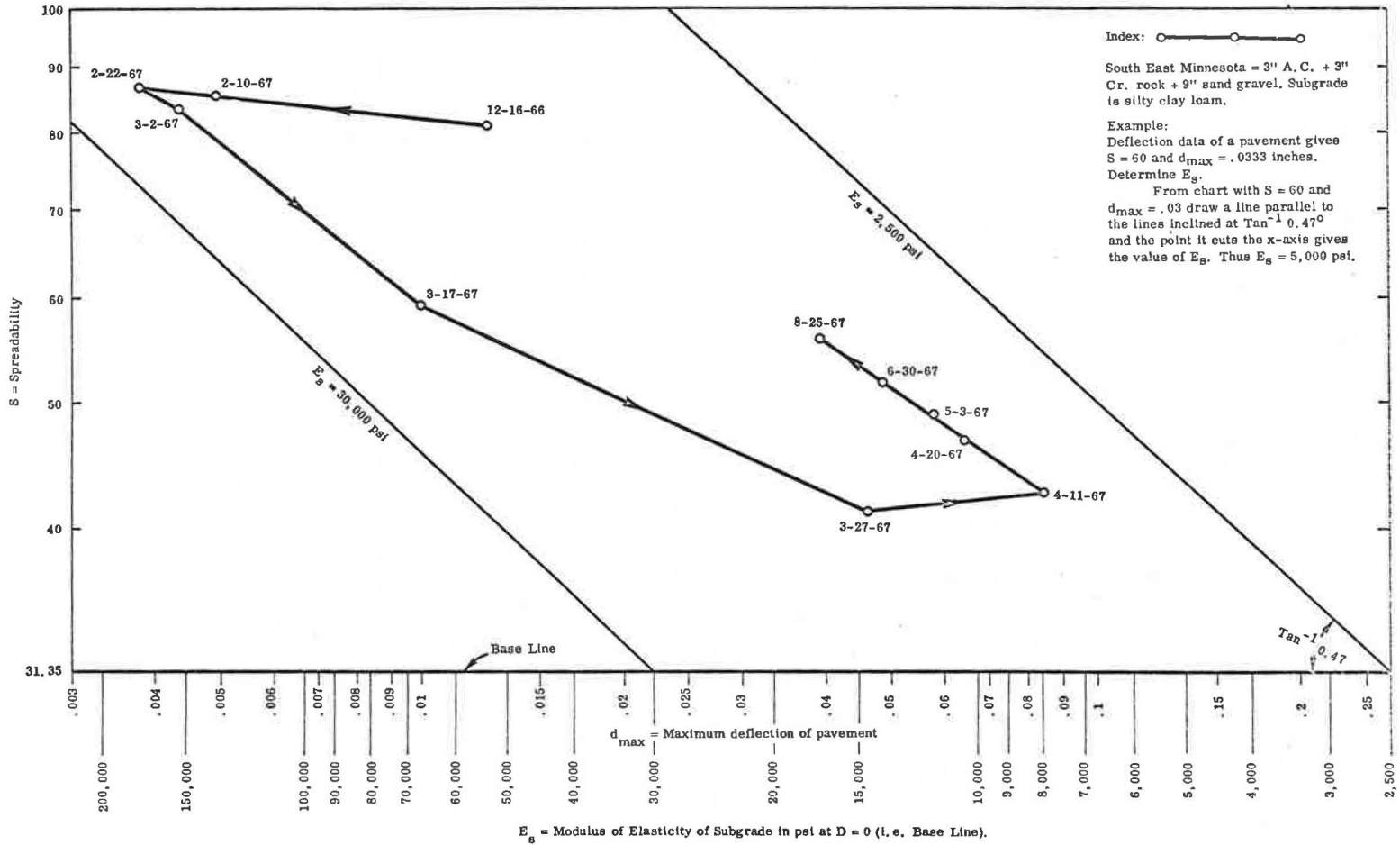


Figure 5. An example of pavement evaluation.

2. For the same pavement thickness, the spreadability value would increase (and thus d_{max} would decrease) as the average modulus of elasticity of the pavement increases, and vice versa, although the subgrade modulus remains the same.

3. For the same average modulus of elasticity of the pavement, the spreadability value would increase (and thus d_{max} would decrease) as the thickness of the pavement increases, and vice versa, although the subgrade modulus would remain the same.

Thus, Figure 5 shows that the modulus of elasticity of the subgrade increased from about 6,000 psi on December 16, 1966, to about 18,000 psi on February 22, 1967, with very little increase in the modulus of elasticity of the pavement. This was probably caused by the frozen condition of the subgrade.

From February 22 to March 17, 1967, the modulus of elasticity of the pavement decreased as indicated by the reduction in spreadability from 88 to 60. This might be due to the increase in the temperature of the asphaltic concrete and a thawing of the moisture in the crushed rock and sand gravel. During this period the modulus of elasticity of the subgrade did not change much, which indicates that the subgrade continued to remain frozen and thus retained the increased modulus caused by freezing.

The period between March 17 to March 27, 1967, shows an increased thawing of the pavement and the thawing of the subgrade, which resulted in the reduced modulus of elasticity of the pavement and the subgrade.

The period March 27 to April 11, 1967, indicates no change in the modulus of elasticity of the pavement but an increased thawing of and more moisture in the subgrade.

The period April 11 to August 25, 1967, shows an increased spreadability and thus an increased modulus of elasticity of the pavement and a slight increase in the subgrade modulus. These changes are probably the results of water draining away from the pavement and the subgrade.

References

22. Scrivner, F. H., Poehl, R., Moore, W. M., and Phillips, M. B. Detecting Seasonal Changes in Load Carrying Capabilities of Flexible Pavements. NCHRP Rept. 76, 1969.
23. Vaswani, N. K. A Method for Evaluating the Structural Performance of Subgrades and/or the Overlying Flexible Pavements. Presented at HRB 50th Annual Meeting and to be published in Highway Research Record series.

Y. H. HUANG, Closure—Vaswani's interest in the discussion of my paper is greatly appreciated. The spreadability used by him is a ratio of the off-center deflections to the center deflection and is, therefore, quite similar to the radius of curvature used in my paper to indicate the difference between off-center and center deflections, keeping in mind that curvature increases as spreadability decreases. It is gratifying that his field study in Virginia as well as other data also shows that the deflection-spreadability ratio changes with the change in modulus ratios, and that the effect of pavement thickness and modulus ratios on spreadability bears the same trend as that on curvature. Because the main purpose of my paper is to relate the curvature to the tensile strain at the bottom of the asphalt layer, which is maximum directly under the load, I have to determine the curvature near to the load by using a small chord length. If I had used the spreadability defined by Vaswani by measuring the off-center deflection as far as 4 ft away from the center, the correlation between the curvature and the tensile strain could not possibly have been established.

FACTORS INFLUENCING THE RESILIENT RESPONSE OF GRANULAR MATERIALS

R. G. Hicks*, School of Civil Engineering, Georgia Institute of Technology; and
C. L. Monismith, Institute of Transportation and Traffic Engineering,
University of California, Berkeley

This investigation is concerned with better defining those properties of granular base materials that contribute to the resilient response of pavement structures and includes a study of the influence of aggregate density, aggregate gradation (percent passing No. 200 sieve), and degree of saturation on the resilient response of two aggregates representative of those used in the construction of asphalt concrete pavements. Tests, carried out in triaxial compression, consisted of applying repeated axial stresses with realistic stress histories at a fixed frequency and at a load duration representative of that expected in the field. For both granular materials, the resilient modulus increased considerably with an increase in confining pressure and only slightly with an increase in axial stress. Poisson's ratio increased with a decrease in confining pressure and an increase in repeated stress. The resilient modulus and Poisson's ratio were also affected to lesser degrees by density, percent passing the No. 200 sieve, and degree of saturation. An analysis of a conventional asphalt concrete pavement over a sandy clay subgrade indicated that reasonable changes in the modulus or Poisson's ratio of the granular base layer can result in considerable changes in the response of the pavement structure to load.

• OVER the years highway engineers have devoted considerable effort toward improving the pavement design process. With the advent of large electronic computers, renewed interest has developed in the use of multilayer analysis as a part of the design procedure to evaluate the response of the pavement structure to load. In such analyses, nonlinear elastic and viscoelastic as well as elastic response characteristics can be used to represent the response of the materials comprising the pavement structure. To consider the influence of granular materials on the response of asphalt pavement structures to load within such a framework, it is necessary to determine their deformation characteristics under loads representative of those occurring in the field.

A number of investigations have, in recent years, examined the resilient response of granular materials (1, 2, 3). From these investigations, it would appear that the following factors may have a significant influence on the stress-deformation characteristics under short-duration repeated loads: (a) stress level (confining pressure), (b) degree of saturation, (c) dry density (or void ratio), (d) fines content (percent passing No. 200 sieve), and (e) load frequency and duration.

These studies also indicate that granular materials possess distinctly nonlinear stress vs. strain behavior with the resilient modulus increasing with an increase in

*Mr. Hicks was with Materials Research and Development, Inc., Oakland, California, when this research was performed.

confining pressure or sum of principal stresses. [Resilient modulus, M_R , is defined as the quotient of repeated axial stress, σ_d , in triaxial compression divided by the recoverable axial strain, ϵ_a , i. e., $M_R = \sigma_d / \epsilon_a$ (in psi).] Little information is available, however, for the effect of stress level on Poisson's ratio for such materials. In addition, most of the investigations have not considered the effect of material variables on the response of the pavement structure to load.

Accordingly, the purpose of this investigation has been to (a) ascertain the significant properties of granular materials at times of loading corresponding to moving vehicles, and (b) determine the influence of each factor on the response of flexible pavements using numerical techniques and results of laboratory tests, with the overall objective of adding to the required body of knowledge necessary for improved pavement design and evaluation.

Editor's Note: This paper as originally prepared included an Appendix containing seven tables and three figures. Because of space limitations, these have not been printed here. This Appendix is available in Xerox form at cost of reproduction and handling from the Highway Research Board. When ordering, refer to XS-34, Highway Research Record 345.

MATERIALS

Two aggregates were used in this investigation: one was a well-graded, subangular, partially crushed gravel and the other a well-graded crushed rock. Both materials have been extensively used in prior studies (2, 4, 5).

To investigate the effects of aggregate characteristics on resilient response, a number of factors were included:

1. Density—three levels termed low, medium, and high (based on ASTM D 2049 64T).
2. Aggregate gradation—three levels (Fig. 1) termed coarse, medium, and fine and based on percent passing the No. 200 sieve as follows: coarse, 2 to 3 percent; medium, 5 to 6 percent; and fine, 8 to 10 percent. [The aggregate gradation was maintained constant above the No. 30 sieve with the grading curve lying in the middle of the limits for a 3/4-in. maximum Class 2 aggregate base (State of California, 1969). Aggregate gradings for both aggregate types are included in Table A1 of the Appendix.]
3. Degree of saturation—dry, partially saturated, and saturated.

EQUIPMENT AND PROCEDURES

Equipment

Measurements of resilient response were made in a conventional triaxial cell on specimens nominally 4 in. in diameter by 8 in. in height. Repeated axial stresses were applied using a pneumatic loading system reported earlier (2).

Axial and radial strains for all specimens were measured using small displacement transducers (LVDT's) (6). Transient and static pore pressure measurements were obtained in the saturated tests with a device similar to that described by Chan and Duncan (7) that permitted both the transient and static values to be determined.

Sample Preparation

For tests on dry materials, specimens were prepared using

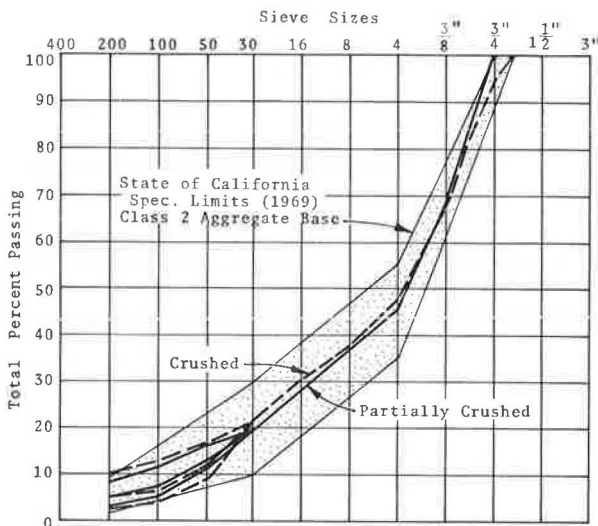


Figure 1. Aggregate grading curves.

vibratory compaction. Variations in density were obtained by changing the number of layers and the vibratory load. All layers were vibrated for 15 sec.

Partially saturated specimens were prepared in a similar manner with the exception that, before compaction, a specific amount of water was added to the oven-dried aggregate and then blended thoroughly. The material was placed immediately in layers into the mold and vibrated to obtain the desired density. At the completion of the test, the water content was determined. This value, together with the initial density, was used to calculate the degree of saturation.

Saturated specimens were also prepared in the manner described for the dry materials with the following changes in procedure. Once the specimen was compacted and completely sealed, de-aired water was allowed to percolate slowly up through the specimen until all entrapped air had been removed. Back pressure techniques were used to ensure complete saturation.

After fabrication, dual LVDT's were clamped onto each specimen outside the membrane to measure radial strains at the quarter points and axial strains over the middle 4 in.

Experimental Procedures

Before testing the specimens over the range of indicated material variables, preliminary tests were conducted to establish the influence of number of stress repetitions and stress sequence on the resilient properties of granular materials. The influence of stress repetitions was ascertained by subjecting a series of specimens to 25,000 load applications and observing variations in resilient modulus, M_R , and Poisson's ratio, ν , over the duration of the test. (Resilient Poisson's ratio, ν , is defined as the quotient of the recoverable radial strain, ϵ_r , divided by the recoverable axial strain, ϵ_a , i. e., $\nu = \epsilon_r/\epsilon_a$.) Two stress sequences (one an increasing, the other a decreasing sequence) were used to evaluate the influence of this factor, the difference in response between the first and last stress condition providing an indication of the effect of stress sequence.

For the dry and partially saturated specimens the results of the preliminary experiments indicated that, so long as the stresses are representative of those found in a pavement structure, the resilient response determined after 50 to 100 axial stress repetitions could be used to properly characterize the behavior of granular materials, and that one sample could be used to determine the resilient response for stresses of different intensities. For saturated granular materials, the resilient response under a given stress level was susceptible to change because of potential increases in the static pore pressure (causing a reduction in $\bar{\sigma}_3$). The studies indicated, however, that, if the sample were conditioned in a drained state with 1,000 to 2,000 axial stress repetitions, the potential for increases in the static pore pressure was reduced. Furthermore, if the principal stress ratio did not exceed 6 to 7, the resilient response after 50 to 100 axial stress repetitions would provide a reasonable indication of that for a material subjected to a complex stress history, and the response due to stresses of different intensities could thus be measured in any sequence on a single sample.

Accordingly, the data reported here were obtained from specimens that had been conditioned for 1,000 repetitions before testing to minimize the effects of uneven contacts at the sample ends or initial imperfections in the sample. Fifty to 100 repetitions of each combination of axial and radial stresses were then applied to the specimen—stresses that covered the range expected in typical pavements.

Moreover, one frequency, 20 repetitions per min, and one stress duration, 0.1 sec, were used. It should be noted that no observable influence on resilient modulus was obtained for durations in the range 0.10 to 0.25 sec.

TEST RESULTS

Influence of Stress Level

Dry and Partially Saturated Series—All specimens were conditioned at a confining pressure of 10 psi and a deviator stress of 15 psi and then subjected to a range in stresses. (After testing a sample at each stress level, it was retested at its initial

stress state to determine the extent of the changes in the material during the period of test. The difference between the initial and final strain states was normally less than 5 percent.) An example of the results for a dry specimen is shown in Figure 2. It will be noted that the resilient axial and radial strains vary not only with the repeated axial stress but also with the confining pressure, σ_3 . Nonlinearities in the stress vs. strain relationships are apparent in all cases with greater degrees of nonlinearity at small values of σ_3 . For axial strains, a slight softening occurred at low axial stress levels, while at higher stress levels specimens exhibited a stiffening type of response. These same patterns were observed on the majority of the specimens tested. For radial strains a softening pattern was always observed. It is possible that some of this nonlinearity was due to insensitivity in the measuring devices and test equipment at the low stress levels; however, this could not be verified.

The effect of the axial stress on the resilient modulus is shown in Figure 3. In this figure it will be noted that the modulus generally increases with increasing axial stress (or principal stress ratio) for principal stress ratios greater than 2. [Although the specimens were tested at principal stress ratios ranging from 1.25 to 7.0, there is evidence that this trend will continue to principal stress ratios of 9 to 11 (2, 6).]

The effect of confining pressure and sum of principal stresses on the modulus is shown in Figures 4 and 5 [in the more conventional manner (2, 8)]. These results emphasize the importance of properly accounting for the stress state and its variation within the base layer so that realistic measures of the modulus can be obtained.

Figure 6 shows the variation in Poisson's ratio with stress level for the sample whose data were presented in Figure 2. The general trends observed in this figure were also obtained from tests on other specimens although the absolute values were dependent on aggregate type, density, and gradation.

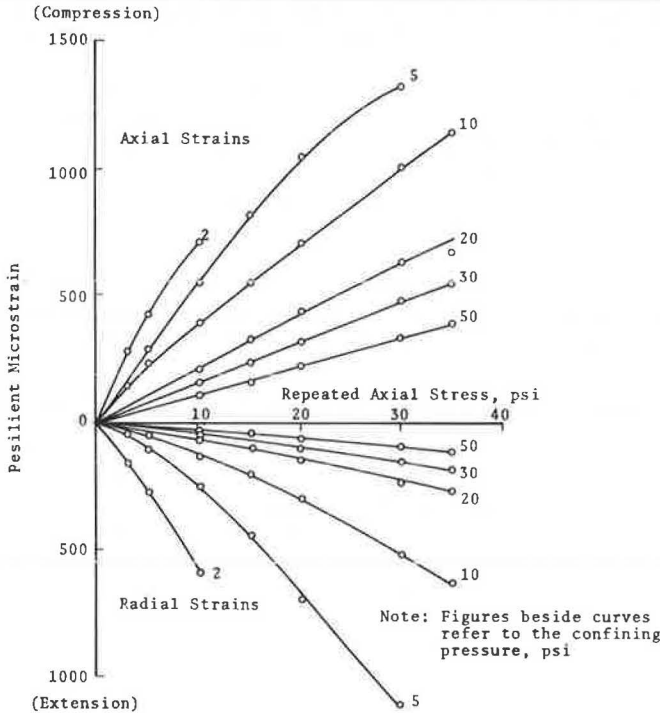


Figure 2. Variation in axial and radial strains with axial stress (partially crushed aggregate, low density, coarse grading, dry).

To simplify the relationship between Poisson's ratio and stress, it was determined (Fig. 7) that the variation in Poisson's ratio could be approximated by a third-degree polynomial curve (fitted to the data using least squares techniques) of the form

$$\nu = A_0 + A_1 \left(\frac{\sigma_1}{\sigma_3}\right) + A_2 \left(\frac{\sigma_1}{\sigma_3}\right)^2 + A_3 \left(\frac{\sigma_1}{\sigma_3}\right)^3$$

This form of the relationship was representative for all the test series.

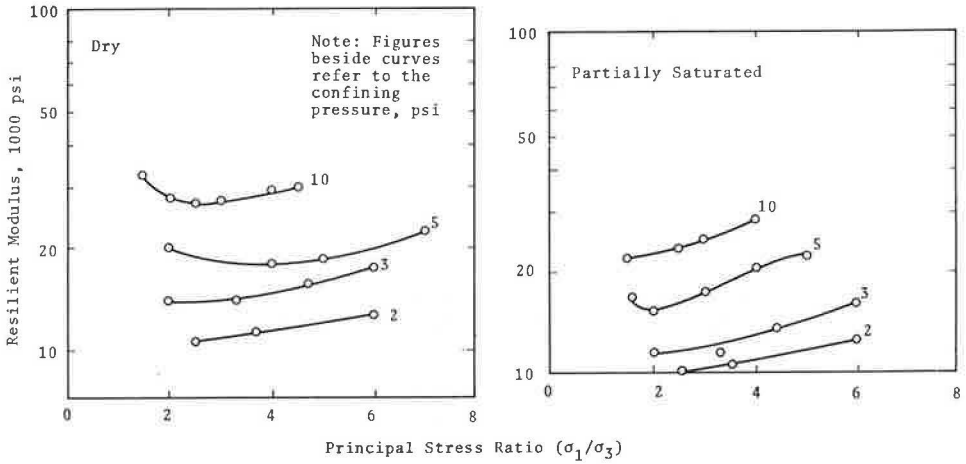


Figure 3. Variation in secant modulus with principal stress ratio (partially crushed aggregate, low density, coarse grading).

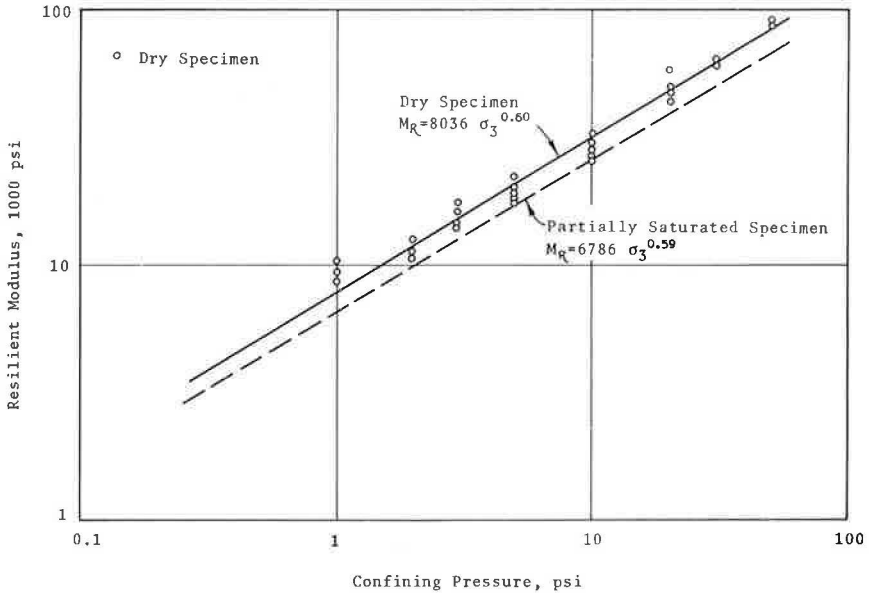


Figure 4. Variation in secant modulus with confining pressure (partially crushed aggregate, low density, coarse grading).

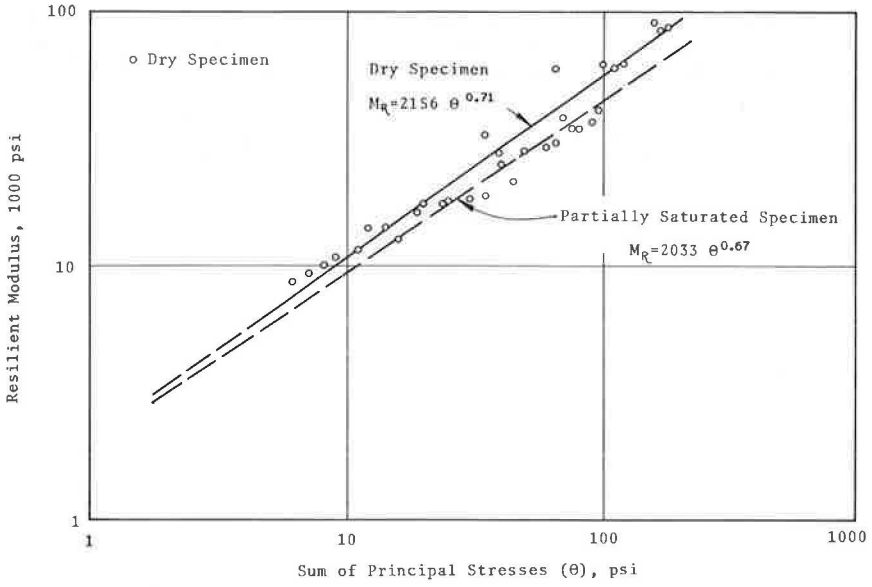


Figure 5. Variation in secant modulus with sum of principal stresses, $\theta = \sigma_1 + 2\sigma_3$ (partially crushed aggregate, low density, coarse grading).

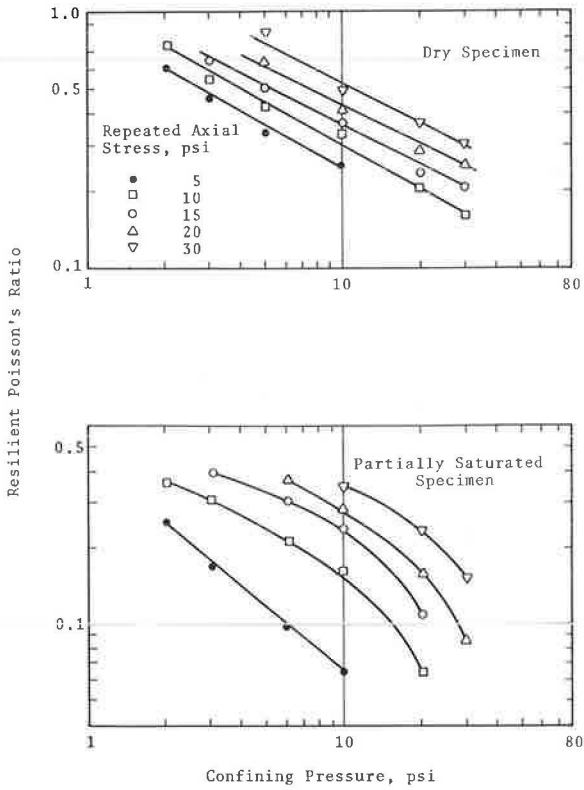


Figure 6. Variation in secant Poisson's ratio with stress level (partially crushed aggregate, low density, coarse grading).

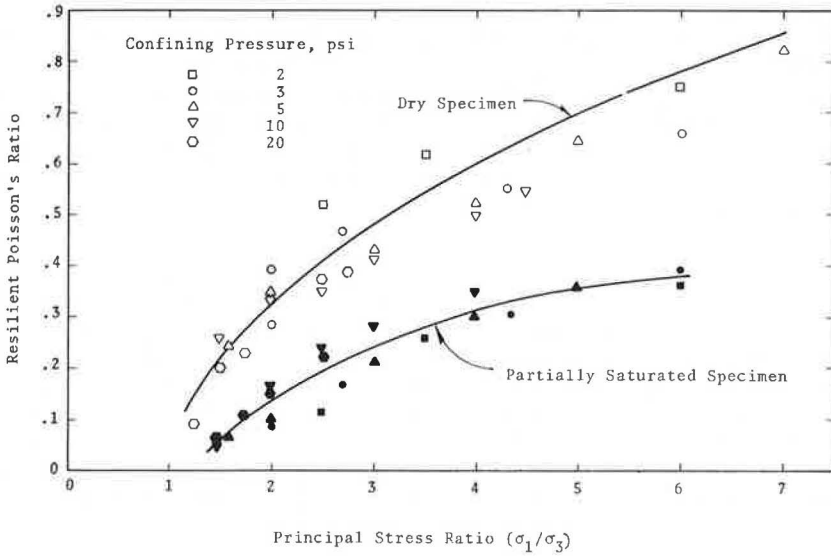


Figure 7. Secant Poisson's ratio as a function of principal stress ratio (partially crushed aggregate, low density, coarse grading).

Saturated Test Series—These specimens were conditioned at 1,000 to 2,000 repetitions in a drained condition and at the same stress conditions used in the dry and partially saturated series. Tests were conducted in both the drained and undrained conditions with resilient axial and radial strains measured after 50 to 100 repetitions. In all instances, drained and undrained stress-strain pairs were nearly the same. For the undrained tests, pore pressure measurements were also recorded throughout the test. Generally, static pore pressure (back pressure) remained relatively constant over the duration of a particular test. Transient pore pressure (that due to the repeated load) developed almost instantaneously and was generally of the order of 5 to 10 percent of the repeated load. For example, for one series of undrained tests, the transient pore pressures were as follows:

Back Pressure (psi)	Repeated Axial Stress (psi)	Sustained Radial Stress (psi)	Transient Pore Pressure (psi)
45	10	10	0.9
45	15	15	1.3

Generally, the variation in radial and axial strain with stress level was similar to that observed for the dry and partially saturated tests, except the relationship between the axial stress and axial strain was slightly more linear than that observed for the dry and partially saturated test series (Fig. A2, Appendix).

Influence of Mix Variables

To permit a reasonable comparison of data, it was necessary to adopt simple and realistic indexes that could be used to define the effect of each variable. For the resilient modulus, the least squares equations relating the modulus to the confining pressure, $\sigma_3 (M_R = K_1 \sigma_3^{K_2})$, and the sum of principal stresses, $\theta (M_R = K_1' \theta^{K_2'})$, for all samples tested were determined. The coefficients K_1 , K_2 , K_1' , and K_2' determined in this manner

are summarized in Tables A2, A3, and A4 of the Appendix for the dry, partially saturated, and saturated test series. In addition, least squares techniques were used to develop relationships between Poisson's ratio and the principal stress ratio, σ_1/σ_3 , for each sample. An example of this has already been shown in Figure 7. Because this relationship generally possessed the same shape for all samples, it was concluded that a mean value for Poisson's ratio could be determined. This value also appears in Tables A2, A3, and A4 where the mean value corresponds to the average of Poisson's ratio at σ_1/σ_3 of 2.0 and 5.0.

Density

Generally, the coefficients K_1 and K_1' were found to increase with increasing density, while K_2 and K_2' remained relatively constant or decreased slightly. The effects are shown for the partially crushed aggregate (dry test series) in Figure 8. Similar trends were found to exist for the partially saturated and saturated test series. For the crushed aggregate, K_1 also tended to increase with density (Fig. A3 of the Appendix). In one instance, however, K_1 was shown to decrease with increasing density (coarse grading, dry test series). The relationship was checked and no experimental error could be found. A possible explanation for this was the inconsistent interaction between

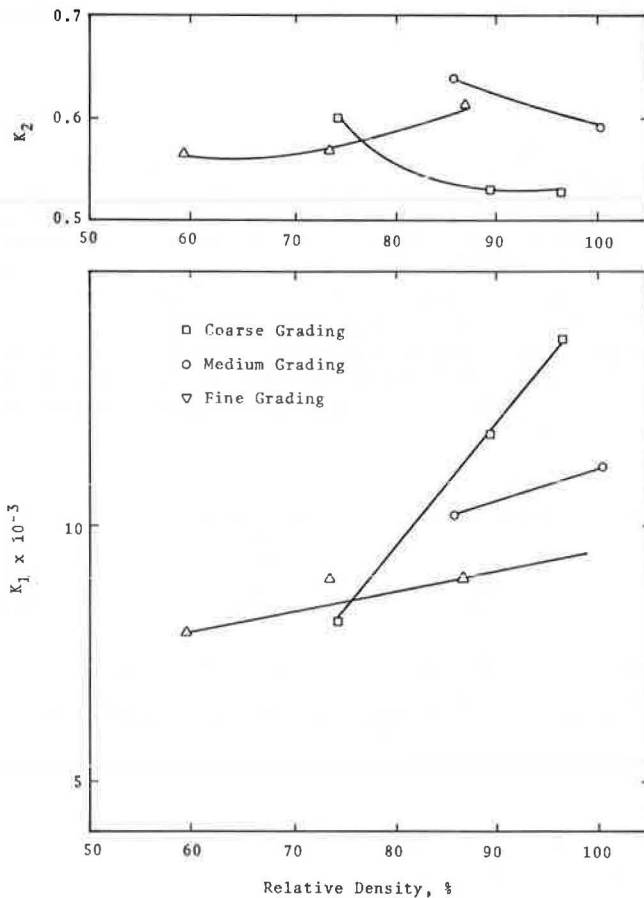


Figure 8. Variation of constants K_1 and K_2 in relationship $M_r = K_1 \sigma_3 K_2$ with relative density (partially crushed aggregate, dry test series).

K_1 and K_2 as the density increases. For the partially crushed aggregate (Fig. 8), as K_1 increased, K_2 tended to remain constant or decrease slightly. This was also shown to be the case for the crushed aggregate (Fig. A3) for the fine and medium gradings. For the coarse grading, however, K_2 increased. Had K_2 decreased in the manner shown for the other test series, K_1 would probably have increased.

When examined in terms of the resilient modulus, the effect of density was found to be greater for the partially crushed aggregate than for the crushed aggregate. For the partially crushed aggregate (Fig. 9), the modulus increased with relative density. In addition, the effect of density decreased as the percent of fines increased. For the crushed aggregate (Fig. 10), relative density had only a small influence on the modulus. Once again, as the fines content increased, the influence decreased. It is interesting

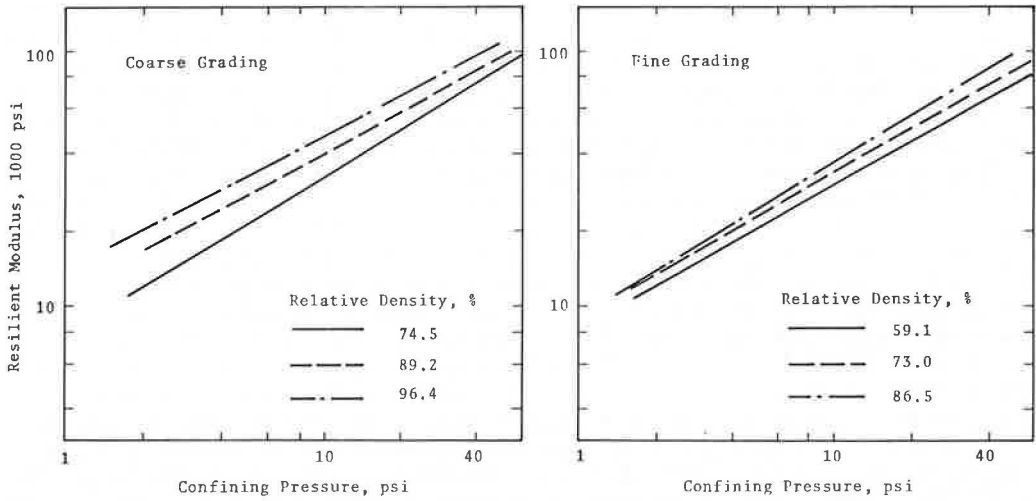


Figure 9. Effect of density on relationship between resilient modulus and confining pressure, σ_3 (partially crushed aggregate, dry test series).

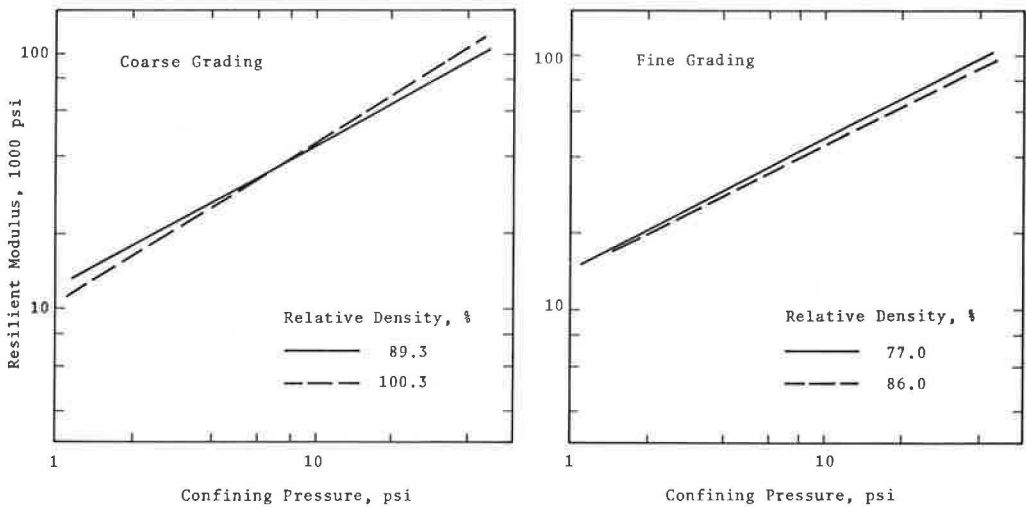


Figure 10. Effect of density on relationship between resilient modulus and confining pressure, σ_3 (crushed aggregate, dry test series).

to note that, despite the irregularity in K_1 (decreased with increased density) for the coarse grading, the modulus was relatively unaffected by density.

The level of density also affected Poisson's ratio. Although the influence was not always clear, the value in most cases decreased slightly with increasing density. For example, Figure 11 shows the influence of density on the partially crushed aggregate at two levels of fines content. In many cases the close coincidence of the curves in Figure 11 (coarse grading) was found to exist; however, there were cases in which there was an obvious decrease in Poisson's ratio with increasing density, as shown in Figure 11 (fine grading—mean values of 0.49, 0.45 and 0.34).

Aggregate Gradation (Percent Passing No. 200)

In all cases, the regression constants K_1 and K_2 (also applicable to K'_1 and K'_2) were affected by the fines content (Table A5 of the Appendix). The manner in which K_1 changed depended on the aggregate type. For the partially crushed aggregate, K_1 generally decreased as the fines content was increased. For the crushed aggregate, however, K_1 increased with increasing fines content. The reason for this is not apparent at this time, but, because the same trends were also observed for the partially saturated and saturated test series, it was concluded that this was a real aspect of the materials tests. Although the effect of gradation on K_2 was not as well defined, it would appear that K_2 decreased slightly as the fines content increased. The influence of gradation on the resilient modulus was not well defined (Fig. 12). However, over the range of confining pressures encountered in field pavements (0 to 10 psi), the resilient modulus of the partially crushed aggregate decreased as the fines content increased, while for the crushed aggregate, the modulus increased with increasing fines content.

Poisson's ratio was also influenced by the fines content. In most instances, as the fines content increased, the mean value for Poisson's ratio was reduced. An example of the manner in which Poisson's ratio varied with grading for partially crushed and crushed aggregate is shown in Figure 13. Regardless of aggregate type, there was a noticeable reduction as the percent of fines increased and the reduction appeared to be a function of the aggregate type (i. e., a greater reduction for the crushed aggregate).

Aggregate Type—For the dry test series, the coefficient K_1 was always larger for the crushed aggregate than in the partially crushed material, regardless of aggregate

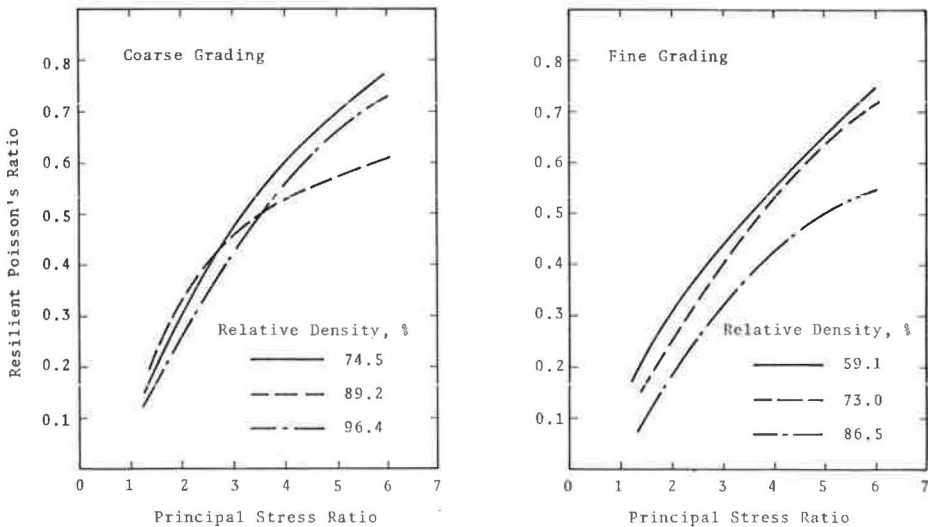


Figure 11. Effect of density on the relationship between resilient Poisson's ratio and principal stress ratio, σ_1/σ_3 (partially crushed aggregate, dry test series).

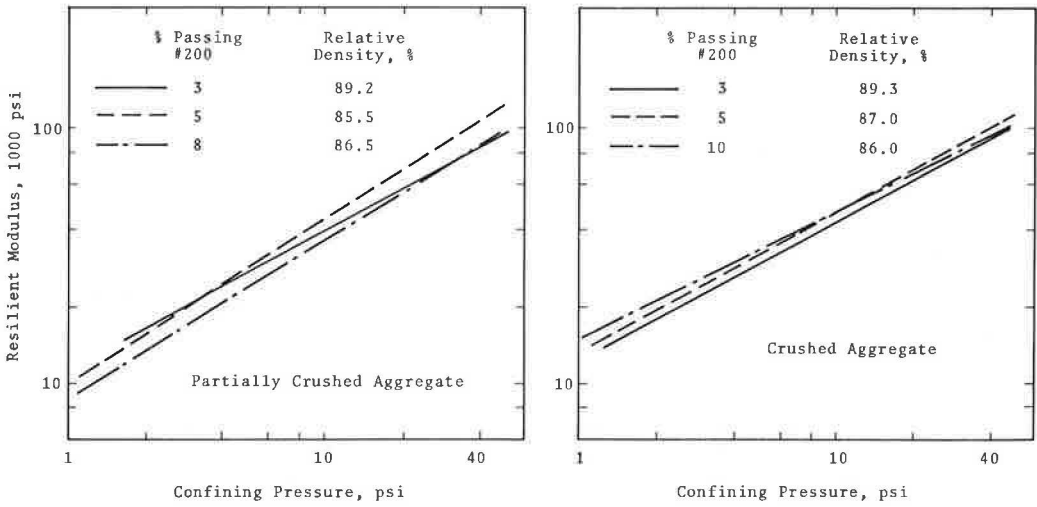


Figure 12. Effect of aggregate gradation (percent passing No. 200) on the relationship between resilient modulus and confining pressure, σ_3 (dry test series).

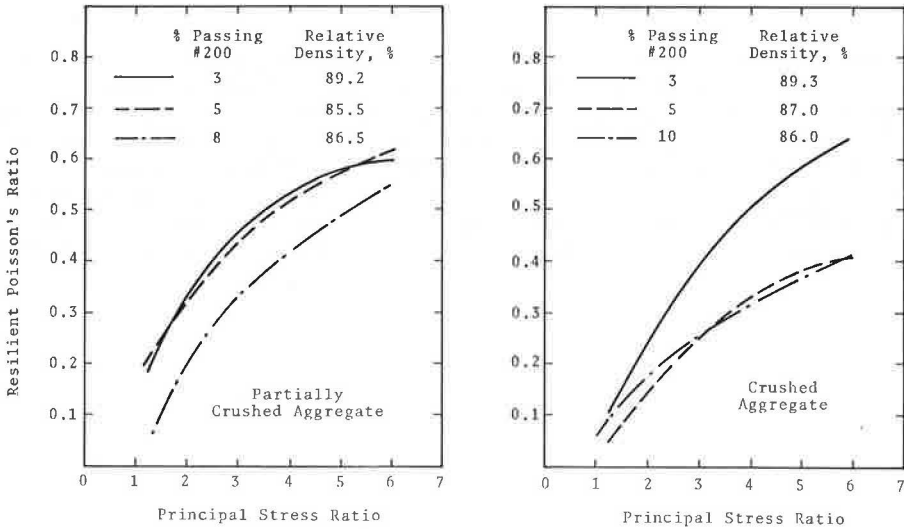


Figure 13. Effect of aggregate gradation (percent passing No. 200) on the relationship between resilient modulus and confining pressure, σ_3 (dry test series).

gradation (Table A5 of the Appendix). The percent change in K_1 , however, appeared to be a function of the aggregate gradation. For the coarse grading the difference was about 5 percent (12,338 vs. 11,752), while for the medium and fine grading the differences were 31 and 64 percent respectively. The actual effect on the modulus was not nearly as great (Fig. 14) because there were also differences in K_2 , but the influence of aggregate gradation is still apparent. The observations noted for the dry test series also held for the partially saturated series, in spite of the fact that all comparisons could not be made at equivalent levels of degree of saturation. For this series, however, there was not the large influence of gradation as the fines content increased.

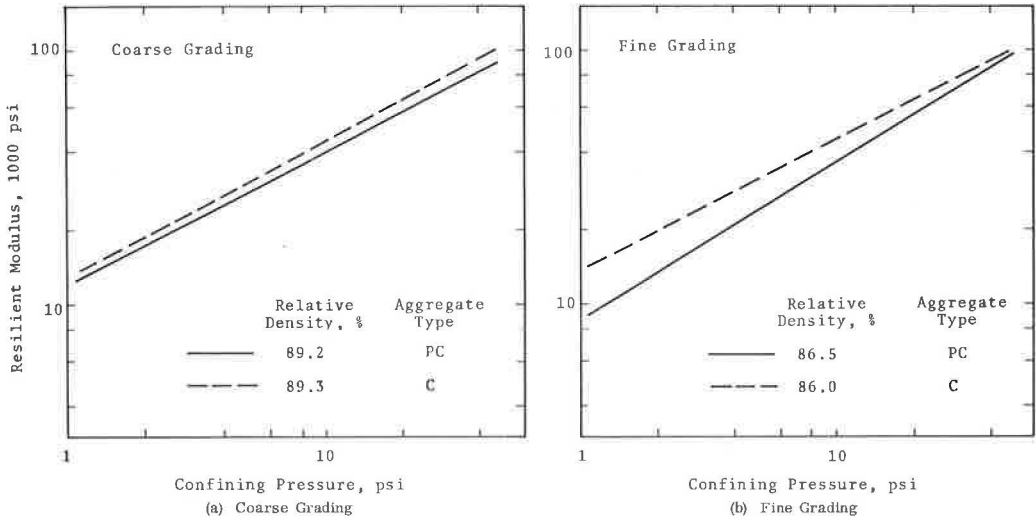


Figure 14. Effect of aggregate type (partially crushed vs. crushed) on the relationship between resilient modulus and confining pressure, σ_3 (dry test series).

Poisson's ratio also varied as a function of aggregate type. For the dry test series, the mean value was generally greater for the partially crushed aggregate. The actual variation for the specimens whose modulus data are shown in Figure 14 is shown in Figure 15. Although the patterns are similar, Poisson's ratios for the crushed aggregate were generally lower than those for the partially crushed aggregate.

Degree of Saturation—In all cases, K_1 decreased from the dry to partially saturated tests series (Table A6 of the Appendix) where the comparisons were made on the basis of total stresses. (For the dry test series, the cell pressure is approximately equal to

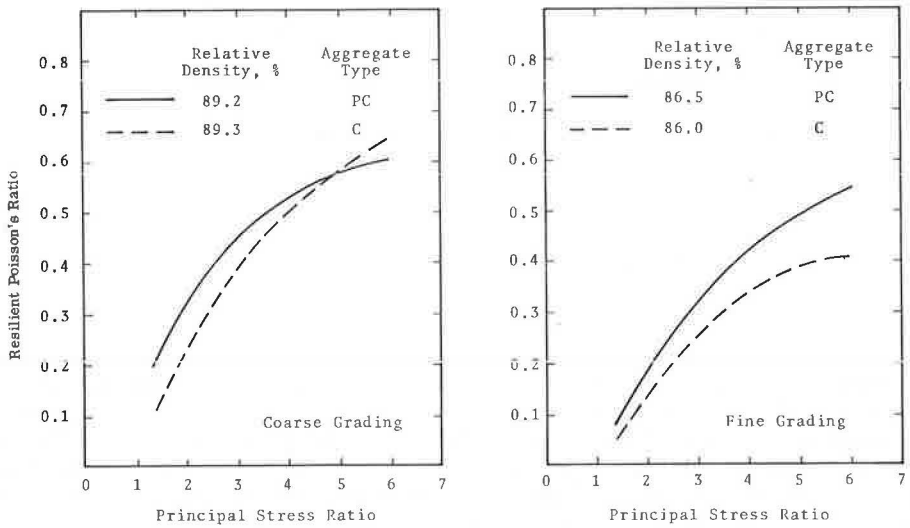


Figure 15. Effect of aggregate type (partially crushed vs. crushed) on the relationship between Poisson's ratio and principal stress ratio, σ_1/σ_3 (dry test series).

the total stress—and in this case only, the effective stress. For the partially saturated test series, the cell pressure is equal to the total stress and is not the same as the effective stress. Pore pressure measurements were not attempted; hence, effective stresses cannot be properly defined in the tests for partially saturated materials.) Figure 16 provides an indication of this effect for each aggregate at two levels of grading—coarse and fine.

When the data were plotted in the conventional manner (Fig. 17), the modulus associated with the partially saturated test series was the lowest. This may be because of the manner in which the data are compared; data for the dry and partially saturated specimens were compared on the basis of total stresses, whereas data for the dry and saturated specimens were compared using effective stresses.

It appears that, if all results were defined in terms of total stresses, the value of K_1 would steadily decrease with increasing degree of saturation (or water content) as shown in Figure 16. The data presented by Kallas and Riley (9) tend to substantiate this hypothesis. Although there were inherent differences in the dry density (mean values of 126.6 pcf for water content of 2.4 percent and 132.2 pcf for

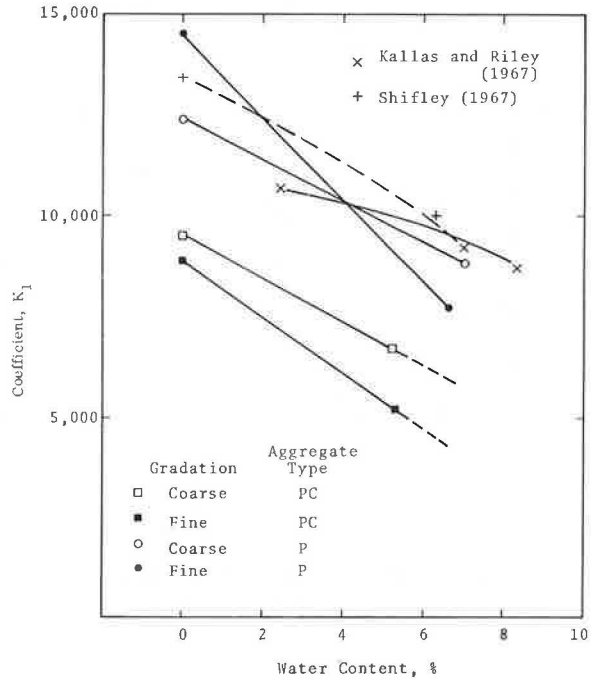


Figure 16. Variation in regression constant, K_1 , with water content in relationship $M_r = K_1 \sigma_3^{K_2}$.

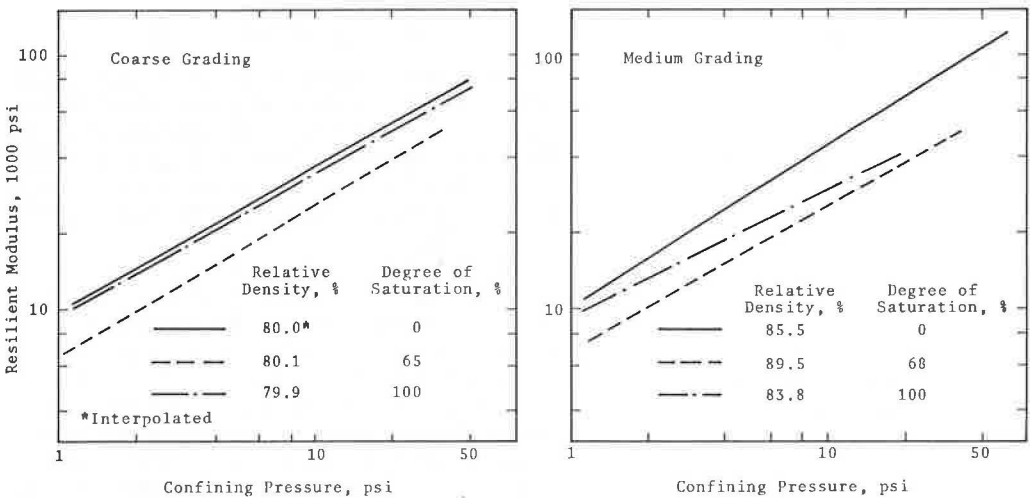


Figure 17. Effect of degree of saturation on the relationship between resilient modulus and confining pressure, σ_3 (partially crushed aggregate).

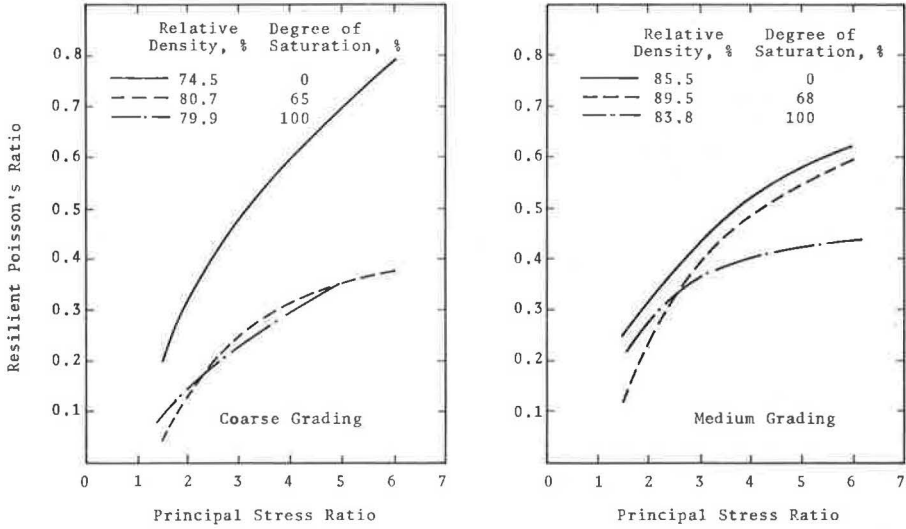


Figure 18. Effect of degree of saturation on the relationship between resilient Poisson's ratio and principal stress ratio (partially crushed aggregate).

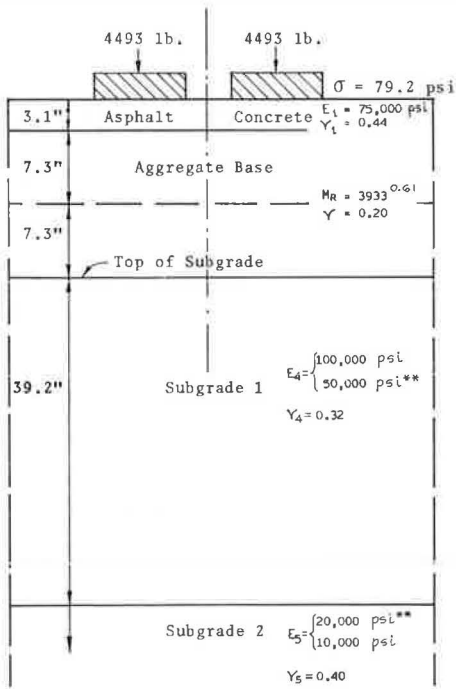


Figure 19. Layered system, loading conditions, and material properties; nonlinear analysis using layered theory.

water content of 6.3 percent) for their tests, the reduction in K_1 with increasing water content was very apparent.

The relationship between Poisson's ratio and the principal stress ratio (Fig. 18) was also affected by degree of saturation. In general, as the degree of saturation increased, Poisson's ratio decreased.

DESIGN IMPLICATIONS

To examine the influence of the aggregate characteristics on the response of a system, a sensitivity analysis was performed on the pavement structure shown in Figure 19. The thicknesses and material properties correspond to those found in Section 1 of the San Diego Test Road (6, 12).

Although there were a number of procedures in which such a structure could be analyzed (e.g., 2, 10, 11, and 12), the analyses performed here were conducted using a computer solution for the pavement system represented as a multilayer elastic structure (10). Using this approach, surface deflections and strains in the asphalt-bound layer have been determined. Changes in computed quantities corresponding to variations in moduli and Poisson's ratios provide an indication of the effect of these characteristics on pavement response.

Because some field measurements of deflection and strain were available, it was decided to use the axle load that had been used in the field measurements for the computations. As shown in Figure 19, this consisted of a set of dual tires with a load per tire of 4,493 lb and a contact pressure of 79.2 psi. The stress distribution was assumed to be uniform over the contact area, which was represented by two circular plates (4.25 in. radius spaced at a center-to-center distance of 11.2 in.).

The modular constant K'_1 in the relationship $M_R = K'_1 \theta^2$ was arbitrarily altered and calculations made for K'_1 values of 3,433 and 4,433, while holding Poisson's ratio at 0.20. The results of these calculations are given in Table 1. As indicated, the change in K'_1 resulted in changes in the predicted responses of varying degrees. For example, the surface deflection varied by ± 0.0015 (7.5 percent) while the surface horizontal strains were altered by $\pm 59 \times 10^{-6}$ in. per in. (12 percent) and $\pm 42 \times 10^{-6}$ in. per in. (12 percent) in the longitudinal and transverse directions respectively. In terms of tensile strain, at the bottom fiber of the asphalt layer the change was on the order of $\pm 67 \times 10^{-6}$ in. per in. (14 percent).

Fixing the modular relationship at $M_R = 3,933\theta^{0.61}$, Poisson's ratio was varied from 0.2 to 0.5. The strains and displacements computed for each level of Poisson's ratio are given in Table 2. This change resulted in a decrease in the surface displacement from 0.0195 to 0.0150 (23 percent) in the surface compressive strains from 485 to 291×10^{-6} in. per in. (40 percent) and 360 to 228×10^{-6} in. per in. (37 percent) and an increase in the maximum tensile strain at the bottom of the asphalt layer from 491 to 515×10^{-6} in. per in. (4 percent).

Although not extensive, this analysis demonstrates the importance of properly defining the significant properties of the granular base layer. Small changes in either the modular relationship or Poisson's ratio can result in considerable changes in

TABLE 1
INFLUENCE OF BASE MODULUS ON PREDICTED DEFLECTIONS AND STRAINS

Type of Response	Predicted Response ^a ($M_R =$)			Measured Response	Comparison Ratio, Predicted/Measured ($M_R =$)		
	$3433\theta^{0.61}$	$3933\theta^{0.61}$ ^b	$4433\theta^{0.61}$		$3433\theta^{0.61}$	$3933\theta^{0.61}$ ^b	$4433\theta^{0.61}$
Total deflection, in.	0.021	0.0195	0.018	0.020	1.05	0.975	0.90
Surface plus base deflection, in.	0.015	0.0133	0.012	0.016	0.94	0.83	0.75
Horizontal microstrain							
Surface, longitudinal	544C	485C	433C	420C	1.39	1.15	1.03
Surface, transverse	{ 402C	360C	323C	520C	0.77	0.69	0.62
Maximum tensile	{ 194T	160T	150T	130T	1.49	1.23	1.15
	543	491	425				

^aModulus of subgrade layers No. 1 and 2 equals 50,000 and 20,000 psi respectively, and Poisson's ratio of base layer equals 0.20.

^bBest estimate.

TABLE 2
INFLUENCE OF POISSON'S RATIO OF BASE IN PREDICTED DEFLECTIONS AND STRAINS

Type of Response	Predicted Response ^a ($\nu =$)			Measured Response	Comparison Ratio, Predicted/Measured ($\nu =$)		
	0.2 ^b	0.35	0.5		0.2	0.35	0.5
Total deflection, in.	0.0195	0.0175	0.0150	0.020	0.98	0.88	0.75
Surface plus base deflection, in.	0.0133	0.0115	0.009	0.0160	0.83	0.71	0.56
Horizontal microstrain							
Surface, longitudinal	485C	402C	291C	420C	1.15	0.96	0.69
Surface, transverse	{ 360C	303C	228C	520C	0.69	0.58	0.44
Maximum tensile	{ 160T	186T	202T	130T	1.23	1.43	1.55
	491	497	515				

^aBase modulus, $M_R = 3933\theta^{0.61}$, modulus of subgrade layers No. 1 and 2 equals 50,000 and 20,000 psi respectively.

^bBest estimate.

critical responses of the pavement structure. If consideration were given to variations in moduli and Poisson's ratios for reasonable changes in density, aggregate gradation, aggregate type, and degree of saturation, the effect on the pavement structure could be considerably greater than that indicated here.

SUMMARY AND CONCLUSIONS

Considering the results of this study, the following points presented here should be emphasized:

1. Reasonable estimates of the resilient response of granular materials can be obtained after 50 to 100 axial stress repetitions for a material subjected to a complex stress history, and the response due to stresses of different intensities can be measured in any sequence on a single sample.

2. The resilient properties of untreated granular materials are affected most significantly by stress level. In all cases the modulus increased considerably with the confining pressure and slightly with the repeated axial stress. So long as shear failure does not occur, the modulus can be approximately related to the confining pressure, σ_3 , or to the sum of principal stresses according to

$$M_R = K_1 \sigma_3^{K_2}$$

and

$$M_R = K_1' \theta^{K_2'}$$

Poisson's ratio increased with decreasing confining pressure and increasing repeated axial stress where the change in Poisson's ratio could be approximated as follows: $\nu = A_0 + A_1(\sigma_1/\sigma_3) + A_2(\sigma_1/\sigma_3)^2 + A_3(\sigma_1/\sigma_3)^3$.

3. The resilient properties of granular material were also affected by factors such as aggregate density, aggregate gradation (percent passing No. 200), aggregate type, and degree of saturation. At a given stress level, the modulus increased with increasing density, increasing particle angularity or surface roughness, decreasing fines content, and decreasing degree of saturation. Poisson's ratio, however, was slightly influenced by density, generally decreased as the fines content increased, and generally decreased as the degree of saturation increased.

4. Small changes in the modular relationship or Poisson's ratio for the granular base layer can result in significant changes in the response of the pavement structure.

ACKNOWLEDGMENTS

The data reported here were obtained from an investigation supported by the Federal Highway Administration. This agency has not reviewed the research findings.

Use of the facilities and assistance of the staff of the Institute of Traffic and Transportation Engineering is gratefully acknowledged.

Carlos Escalante of Materials Research and Development, Inc., prepared the figures.

REFERENCES

1. Dunlap, W. A. A Report on a Mathematical Model Describing the Deformation Characteristics of Granular Materials. Project 2-8-62-27, Texas Transportation Inst., Tech. Rept. No. 1, 1963.
2. Seed, H. B., Mitry, F. G., Monismith, C. L., and Chan, C. K. Prediction of Flexible Pavement Deflections From Laboratory Repeated Load Tests. NCHRP Rept. 35, 1967.
3. Thompson, O. O. Evaluation of Flexible Pavement Behavior With Emphasis on the Behavior of Granular Layers. PhD dissertation, Univ. of Illinois, 1969.
4. Mitry, F. G. Determination of the Modulus of Resilient Deformation of Untreated Base Course Materials. PhD dissertation, Univ. of California, 1964.

5. Shifley, L. H. The Influence of Subgrade Characteristics on the Transient Deflections of Asphalt Concrete Pavements. PhD dissertation, Univ. of California, 1967.
6. Hicks, R. G. Factors Influencing the Resilient Properties of Granular Materials. PhD dissertation, Univ. of California, 1970.
7. Chan, C. K., and Duncan, J. M. A New Device for Measuring Volume Changes and Pressures in Triaxial Tests on Soils. In Materials and Research Standards, Vol. 7, July 1967.
8. Biarez, J. Contribution à l'Etude des Propriétés Mécaniques des Sols et des Matériaux Pulvérulents. DSci thesis, Univ. of Grenoble, 1962.
9. Kallas, B. F., and Riley, J. C. Mechanical Properties of Asphalt Pavement Materials. Proc., Second Internat. Conf. on the Structural Design of Asphalt Pavements, Univ. of Michigan, 1967.
10. Kasianchuk, D. A. Fatigue Considerations in the Design of Asphalt Concrete Pavements. PhD dissertation, Univ. of California, 1967.
11. Dehlen, G. L., and Monismith, C. L. The Effect of Nonlinear Material Response on the Behavior of Pavements Subject to Traffic Loads. Presented at HRB 50th Annual Meeting, 1970.
12. Hicks, R. G., and Finn, F. N. Analysis of Results From the Dynamics Measurements Program on the San Diego Test Road. Presented at AAPT Annual Meeting, 1970.

COMPRESSIVE STRESS PULSE TIMES IN FLEXIBLE PAVEMENTS FOR USE IN DYNAMIC TESTING

Richard D. Barksdale, School of Civil Engineering, Georgia Institute of Technology

Traffic moving over a pavement structure results in a large number of rapidly applied stress pulses being applied to the material comprising each layer. The most realistic method to characterize this stress condition is through the use of dynamic tests such as the repeated load triaxial test or fatigue tests. In this investigation the shape and duration of the compressive stress pulse resulting at different depths beneath the surface are studied for several flexible pavement systems and for vehicle speeds varying between 1 and 45 mph. A comparison is made of the compressive stress pulses caused by a vehicle moving over a layered pavement system at a speed of 1 mph using both linear and nonlinear elastic finite element theory. Viscous effects and inertia forces are neglected in both theories. Because the normalized stress pulses calculated using the linear elastic theory are found to agree closely with those calculated using the nonlinear theory, linear elastic finite element theory is used throughout the remaining portion of the study.

The results of this investigation show that the shape of the compressive stress pulse varies from approximately a sinusoidal one at the surface to more nearly a triangular pulse at depths below approximately the middle of the base. Typically, the compressive pulse time also varies almost inversely with vehicle speed up to at least a speed of 45 mph. Pavement geometry and layer stiffness for spring and summer temperatures do not have a significant influence on the stress pulse times for conventional pavement constructions. For vehicle speeds up to 45 mph, the calculated stress pulse times were empirically corrected for viscous effects and inertia forces using the results of field measurements made at the AASHO Road Test. Finally, curves are presented from which approximate compressive stress pulse times can be selected for use in dynamic testing.

●AS traffic moves along the highway pavement structure, large numbers of rapidly applied stress pulses are applied to each element of material below and for some distance out to the sides of the wheelpath. Typically, these stress pulses last for only a short period of time, and the magnitude and duration of the pulse vary with the type of vehicle and its speed, the type and geometry of the pavement structure, and the position of the element of material under consideration.

To evaluate material properties in the laboratory, the best approach available at the present time is to simulate as closely as possible the field loading condition using a dynamic test. Dynamic bending tests have been used to evaluate fatigue resistance of stabilized surface and base materials (1, 2). Repeated load triaxial tests have also been used by a number of investigators (3, 4, 5). This test gives the dynamic modulus and the permanent rutting (strain) characteristics of both stabilized and unstabilized pavement materials. These results can be used in either theoretical analyses (6, 7) or in direct comparison with the effects of varying basic parameters such as compaction density, gradation, water content, or amount of stabilizing agent.

In performing the repeated load triaxial test, a cylindrical specimen of material to be tested is placed inside a conventional triaxial cell and usually subjected to a uniform chamber pressure. A large number of repeated axial loads are then applied to the specimen through the piston of the cell by either a pneumatic, hydraulic, or mechanical loading system (1, 2, 3, 4, 5). In the field, both the confining pressure and axial stress would vary as a wheel load moves over the surface. However, for convenience, most investigators have maintained the confining pressure a constant although it can and probably should be varied (5). The obvious advantage of the repeated load test over tests that use a single, slowly applied loading is that the rapidly applied, repetitive stress condition used in repeated load tests much more closely approximates the dynamic loading conditions that actually occur beneath the surface of a pavement system.

The purpose of this paper is to investigate the shape and duration of the axial stress pulse that should be used in performing a dynamic repeated load test. Factors studied that influence the stress pulse are the geometry and stiffness of the pavement structure, the vehicle speed, wheel configuration, rotation of principal stress axes, and material nonlinearity. The stress pulses directly beneath the wheel loading for a range in pavement geometries and layer stiffnesses are determined by using linear elastic layered theory neglecting inertia and viscoelastic effects. The results obtained using the elastic layered theory are compared with the results from a nonlinear theory and are shown to give good agreement. Finally, curves are presented that can be used to select appropriate stress pulse times for dynamic testing for vehicle speeds varying from 1 to 45 mph.

CALCULATION OF THE STRESS PULSE USING ELASTIC LAYERED THEORY

As the velocity of the vehicle increases, field measurements (8) have shown that the stresses and deflections in a layered pavement system become less because of inertia forces and viscous effects. The solution of the general layered system problem considering both viscous effects and inertia forces is very complicated, and this problem has not yet been completely solved. Viscous effects can at least be partially accounted for by testing the pavement materials by using approximately the same transient stress conditions as those that occur in the field caused by the moving vehicle.

To approximately evaluate the shape and duration of the stress pulse that should be applied to a specimen, elastic finite element theory was used neglecting inertia forces and viscous effects. For most of the investigation a single static, circular load of 9,000 lb was applied normally to the surface of the layered system. Shear stresses between the tire and pavement surface were assumed to be negligible. The pressure exerted by the tire on the surface was assumed to be 79.6 psi uniformly distributed over a circular area having a radius of 6 in. The elastic layered pavement system was idealized by using 221 rectangular, ring-shaped finite elements as shown in Figure 1. The size of the elements were increased with increasing distance from the loading as the stress gradients decreased. Each layer was assumed to extend in the lateral direction a large but finite distance, and the interfaces between layers were assumed to be rough.

The principle of superposition was used to calculate the shape and duration of the stress pulse and its variation with depth as a vehicle moves at a constant speed over the surface of a pavement system. The superposition approach used to solve this problem can be conceptually visualized as allowing the vehicle to remain stationary and the element to move past under the vehicle. If it is assumed that zero time corresponds to the instant that the wheel is directly above the element for which the stress pulse is desired, then the half of the theoretically symmetrical stress pulse corresponding to the vehicle moving away from the point can be readily constructed by plotting at the corresponding times the appropriate stress quantities calculated at a number of points out from the loading along a horizontal plane passing through the element under consideration. The time at which the stress is plotted simply corresponds to the distance out from the axis of symmetry of the loading to the point being considered divided by the vehicle speed. The finite element computer program used in this study (9)

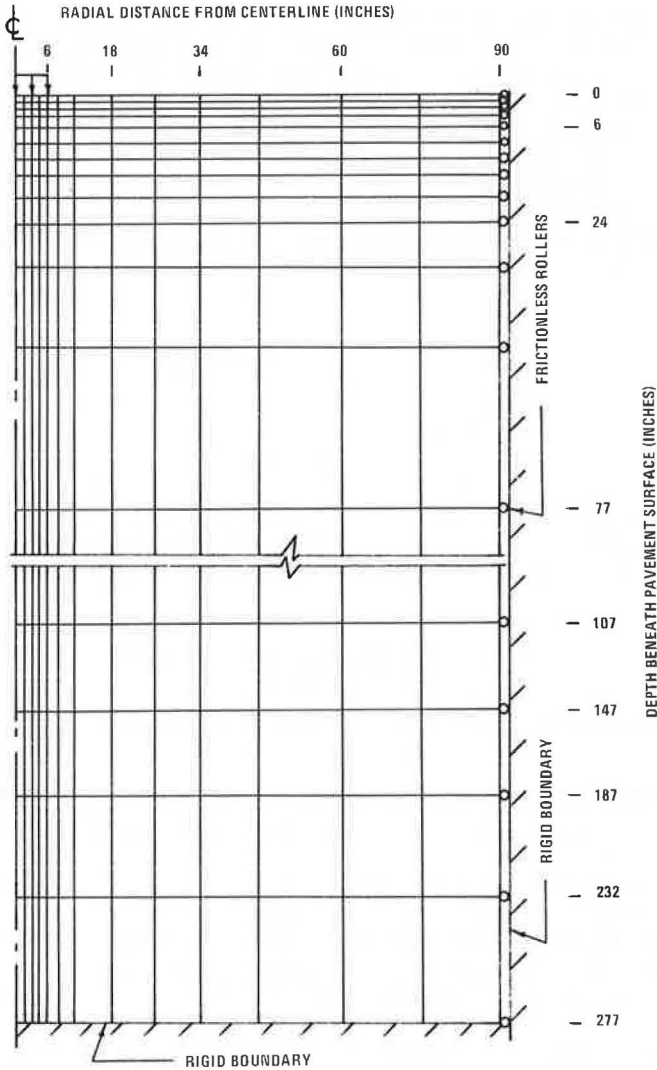


Figure 1. Finite element idealization of pavement system.

calculates the stress state at the center of each finite element. To more accurately construct the stress pulse, the values of stress in between the element centers were estimated by interpolating along a horizontal plane. To do this, a third-degree parabola was passed through the known stress points using Lagrange's interpolation formula (10). All numerical calculations were performed on the UNIVAC 1108 computer at the Georgia Institute of Technology.

COMPARISON OF LINEAR AND NONLINEAR ELASTIC THEORY

To evaluate the effect of material nonlinearity on the shape of the stress pulse, the stress pulses obtained using the linear elastic layered theory were compared with those calculated using a nonlinear elastic theory. The comparison was made for a layered pavement system consisting of 4 in. of asphalt concrete surfacing, 15 in. of crushed stone base, and a silty clay subgrade.

The asphalt concrete was assumed to have a modulus of elasticity of 100,000 psi in compression and 90,000 psi in tension. Several approximations were made in characterizing the granular base. When subjected to a compressive stress state, the granular material was assumed to behave isotropically and have an elastic modulus equal to

$$E_R = 15,000 \sigma_3^{0.5} \quad (1)$$

where

E_R = resilient modulus (psi), and
 σ_3 = confining pressure (psi).

Consider now the behavior of the lower part of the base when subjected to radial (lateral) tensile stresses. A certain amount of radial tensile stress can be applied before slip of the material occurs. For stress levels below those required to cause slip, the tensile stresses are resisted by frictional stresses developed between the granular particles caused by the vertical compressive stresses that exist in the base. The lateral tensile stress that can be developed before slip occurs depends on both the magnitude of the normal stress and the coefficient of friction between the particles of stone. For this study a coefficient of friction of 0.6 was used, which corresponds to a friction angle of approximately 31 degrees. When the base was subjected to tensile stresses less than that required to cause slip, a vertical elastic modulus of 10,000 psi and a lateral modulus of 8,000 psi were assigned. When slip did occur, a vertical modulus of 6,000 psi and a radial modulus of 600 psi were used. These values of moduli are probably conservative because, as soon as slip does occur, passive pressure in the surrounding soil further out will be developed, which will result in a rapid increase in stiffness in the radial direction. Furthermore, recent studies (13) indicate that an unstabilized granular material in an unconfined condition can have a vertical modulus of elasticity of 5,000 psi or more.

Although at the present time the approximations that were made concerning the granular base have not been fully justified experimentally, it is believed that these assumptions are certainly more nearly valid than assuming that a granular base behaves as an isotropic, elastic material when subjected to tensile stress components. Furthermore, using this approach, good agreement was found between calculated and measured subgrade stresses on one of the unstabilized granular bases at the AASHO Road Test (14). Certainly, the behavior of granular bases needs considerable further study.

The resilient modulus of the silty clay subgrade was assumed to be a function of only the deviator stress (11) with $E_R = -1,090(\sigma_1 - \sigma_3) + 16,000$ when $\sigma_1 - \sigma_3$ is less than 12.4 psi, and $E_R = 43.6(\sigma_1 - \sigma_3) + 2,350$ when $\sigma_1 - \sigma_3$ is greater than 12.4 psi. The resilient modulus, E_R , and the deviator stress, $\sigma_1 - \sigma_3$, are both measured in psi in these expressions.

The nonlinear problem was solved numerically by gradually increasing the surface loading in 50 increments using an anisotropic finite element computer program (9, 14). The corresponding elastic layered system was then solved using the same moduli for the asphalt concrete as used in the nonlinear analysis and a modulus of 35,000 psi and 12,000 psi for the base and subgrade respectively. The moduli used in the elastic analysis for the base and subgrade were approximately the equivalent values determined in those layers from the nonlinear analysis.

The comparison between the linear and nonlinear theory for half of the theoretically symmetrical, vertical compressive stress pulse is shown in Figure 2. Stress pulses shown in this and all subsequent figures are for a vehicle speed of 60 mph as evaluated from elastic theory. Although the absolute values of the vertical compressive stresses were different, the stress pulses were found to be very similar when normalized by the peak value of the vertical stress. Because of the good agreement between the calculated linear and nonlinear normalized stress pulses, all subsequent theoretical calculations were performed using the linear finite element theory.

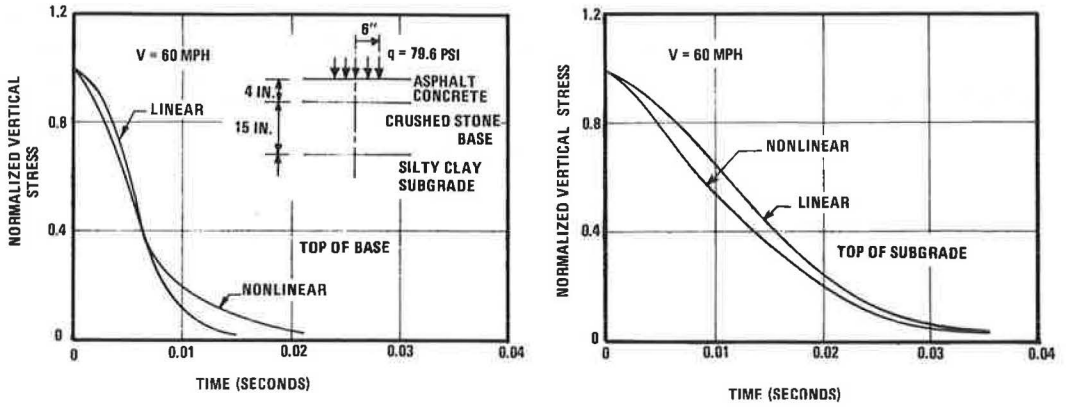


Figure 2. Comparison of theoretical linear and nonlinear vertical compressive stress pulses at two depths—4-in. surfacing and 15-in. base.

FACTORS INFLUENCING THE SHAPE AND DURATION OF THE STRESS PULSE

As a wheel load moves along the surface in the direction of an element of material, the orientation of the principal stress axes is gradually rotated (Fig. 3). At the instant the wheel is directly above the element, the principal stress axes are oriented vertically and horizontally with the principal compressive stress acting in the vertical direction. A typical comparison of half of the vertical and principal compressive stress pulses is given for two depths in Figure 4 for a system having a 4-in. asphalt surfacing and a 15-in. base. The principal normalized stress is seen to be greater than the vertical stress at all times except when they are equal at the instant the load is over the element. Therefore, the principal stress pulse has a longer duration than does the vertical stress pulse with this difference becoming greater with depth.

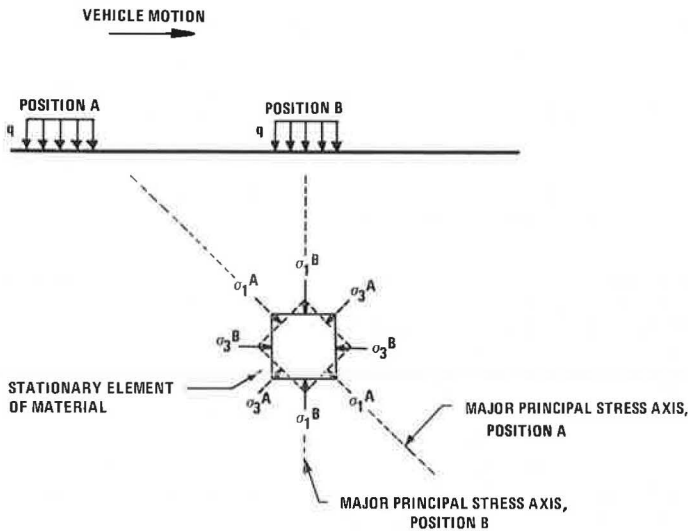


Figure 3. Rotation of principal stress axis of an element as a vehicle moves over the surface.

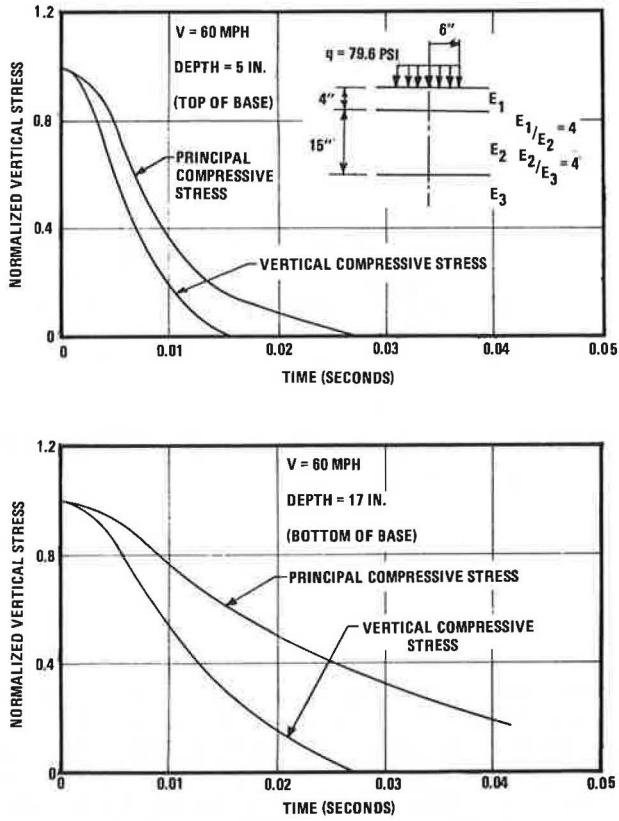


Figure 4. Comparison of vertical and principal compressive stress pulses for two depths—4-in. surfacing and 15-in. base.

The actual stress pulse shape is approximated in this investigation using either an equivalent sinusoidal or triangular stress pulse as shown in Figure 5. The reason for choosing these simplified equivalent pulse shapes is that all commonly used pneumatic, hydraulic, and mechanical loading systems can usually be made to apply one or both

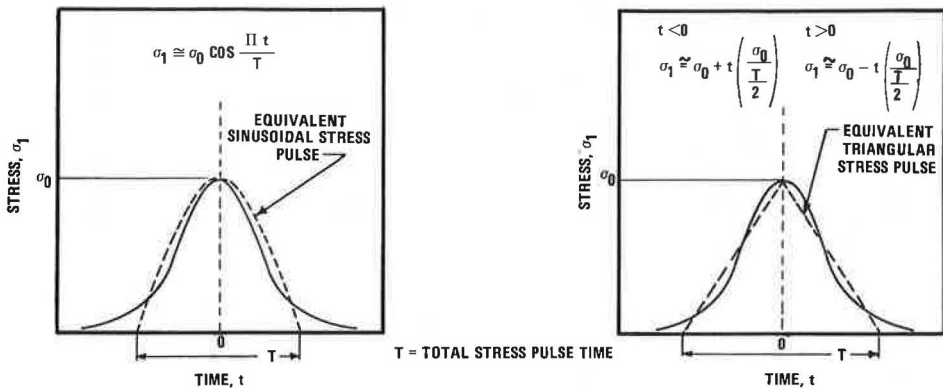


Figure 5. Equivalent sinusoidal and triangular stress pulses.

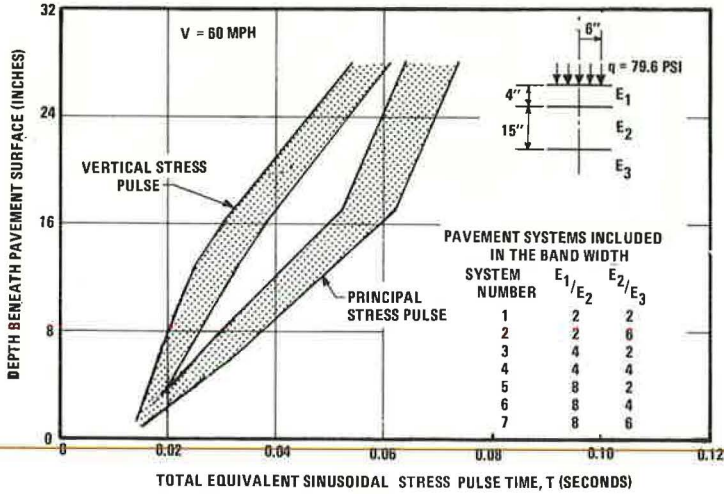


Figure 6. Variation of theoretical vertical and principal compressive stress pulse with depth—4-in. surface and 15-in. base.

of these simplified wave forms. The sinusoidal and triangular stress pulses were visually fitted to the calculated data. A sophisticated numerical curve-fitting technique was not believed to be justified because at the present time it is not possible to predict with an certainty what effect the length of time that a portion of the stress pulse stays on the sample will have on the overall physical response of a specimen. Furthermore, the uncertainties associated with calculations made involving asphalt concrete and

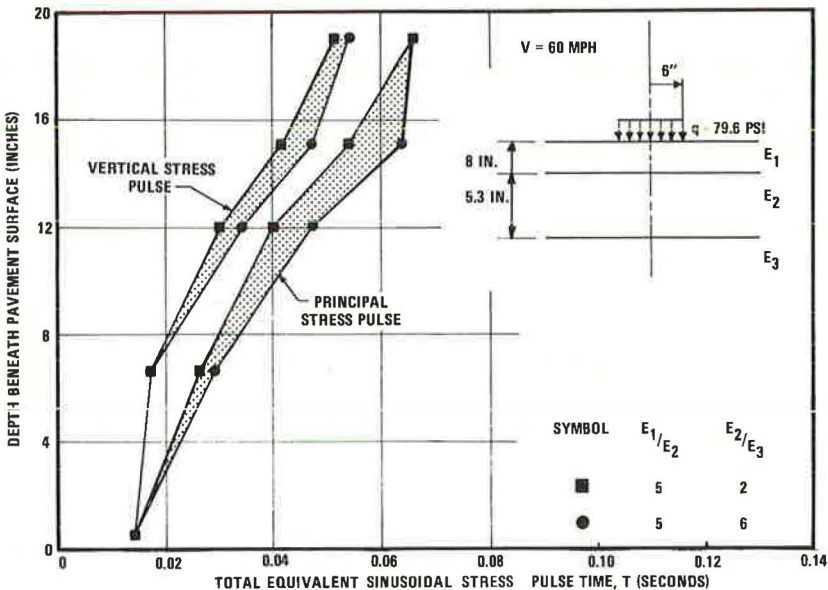


Figure 7. Variation of theoretical vertical and principal compressive stress pulse time with depth—8-in. surface and 5.3-in. base.

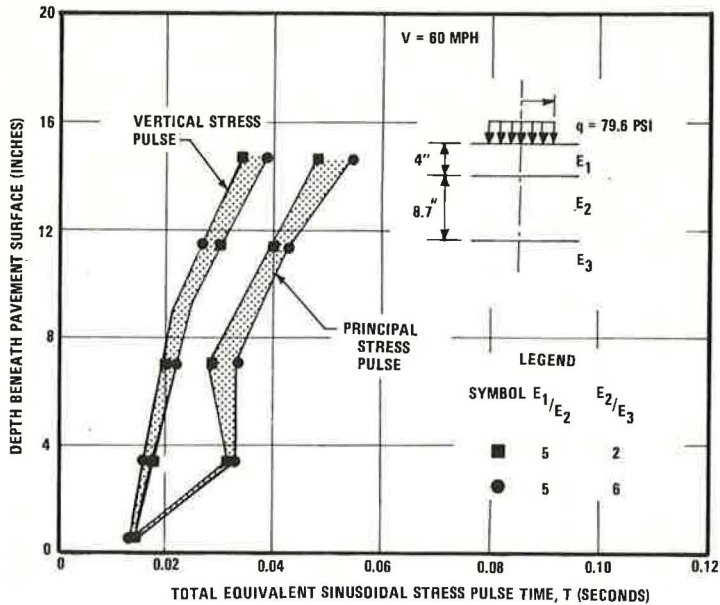


Figure 8. Variation of theoretical vertical and principal compressive stress pulse time with depth—4-in. surface and 8.7-in. base.

unstabilized granular bases using elastic layered theory do not justify a high degree of precision. Undoubtedly the technique used accounts for some of the scatter in the results shown in Figures 6 through 8.

The effect of depth, pavement geometry, and layer stiffness on the equivalent sinusoidal vertical and principal stress pulse times is shown in Figures 6 through 8 for a 9,000-lb, single-wheel loading. These figures show that the total stress pulse time for both the principal and axial stress pulses increases significantly with depth beneath the pavement surface. For example, the vertical stress pulse time in a typical pavement consisting of a 4-in. asphalt concrete surfacing overlying a 15-in. granular base would increase by a factor of approximately 2.7 in going from the surface down to the top of the subgrade. These results clearly indicate that the variation in pulse time with depth should certainly be considered in conducting an experimental testing program. The principal stress pulse time becomes greater with depth than does the vertical compressive stress pulse. After a certain depth, however, the difference in the two equivalent stress pulse times apparently becomes approximately constant or may even decrease with further increase in depth, depending on the pavement geometry.

Figure 6 shows that, for a 4-in. surfacing and 15-in. base and a reasonably wide range in layer stiffnesses, the total stress pulse times did not change drastically with changes in layer stiffness. Considering the uncertainties associated with using the elastic layered theory, it was deemed justifiable to investigate only two reasonable variations in layer moduli for the other two systems studied, and to use only the average total pulse times in summarizing the results of this investigation.

The shape of the stress pulse also varies significantly with depth (Fig. 9). Near the surface the pulse shape can be reasonably accurately approximated as a half sinusoid. With increasing depth, however, the pulse flattens out significantly so that, for elements located in the subgrade, the pulse can, in general, be more accurately approximated by a triangular pulse shape. For the pavement system shown in Figure 6, which has a 4-in. asphalt surfacing and 15-in. base, the sinusoidal shape pulse gives a reasonably good approximation to the stress pulse above a critical depth somewhere between the middle and top portion of the base; below this level the triangular pulse is

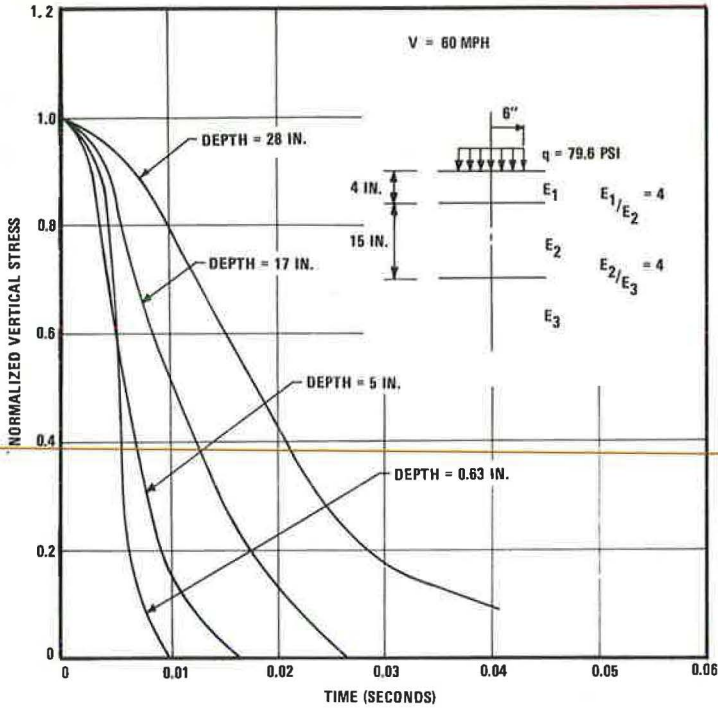


Figure 9. Variation of calculated vertical compressive stress pulse shape with depth—4-in. surface and 15-in. base.

probably more appropriate. For the system with a 4-in. surfacing and 8.7-in. base (Fig. 8), the approximate depth for change in shape of the stress pulse is in the vicinity of the top of the base. The critical depth of the stress pulse shape for the system with the 8-in. asphalt surface and 5.3-in. granular base (Fig. 7) is in the lower part of the asphalt layer.

All of the stress pulses shown are for a vehicle speed of 60 mph and a single-wheel loading. A single-axle, dual-wheel loading causes a change in the pulse shape and peak stress in the lower part of the base and subgrade. The equivalent pulse times for points located beneath the center of the dual-wheel assembly for practical purposes can be assumed to be the same as for a single-axle loading, although a slight decrease in equivalent pulse time does apparently occur. Neglecting inertia forces and viscous effects, the effect of vehicle speed would be to simply compress the time scale of the stress pulse in an inverse proportion to the vehicle speed. Thus, if the pavement performs as an elastic system, an increase in vehicle speed would tend to linearly decrease the stress pulse time, and a decrease in speed would linearly increase the stress pulse time. In going from a creep speed to speeds of 45 to 60 mph or more, however, inertia forces and viscous effects would be expected to probably influence the stress pulse and result in a nonlinear scaling law. These effects are empirically considered in the next section by adjusting the stress pulse times to agree with measured pulse times.

COMPARISON WITH EXPERIMENTALLY MEASURED STRESS PULSES

To investigate the influence of inertia and viscous effects, the theoretically calculated stress pulses were compared with the pulse times measured in the field during the AASHO Road Test. A reasonably good evaluation of the elastic theory can be obtained because most of the significant variables for this study are documented in the

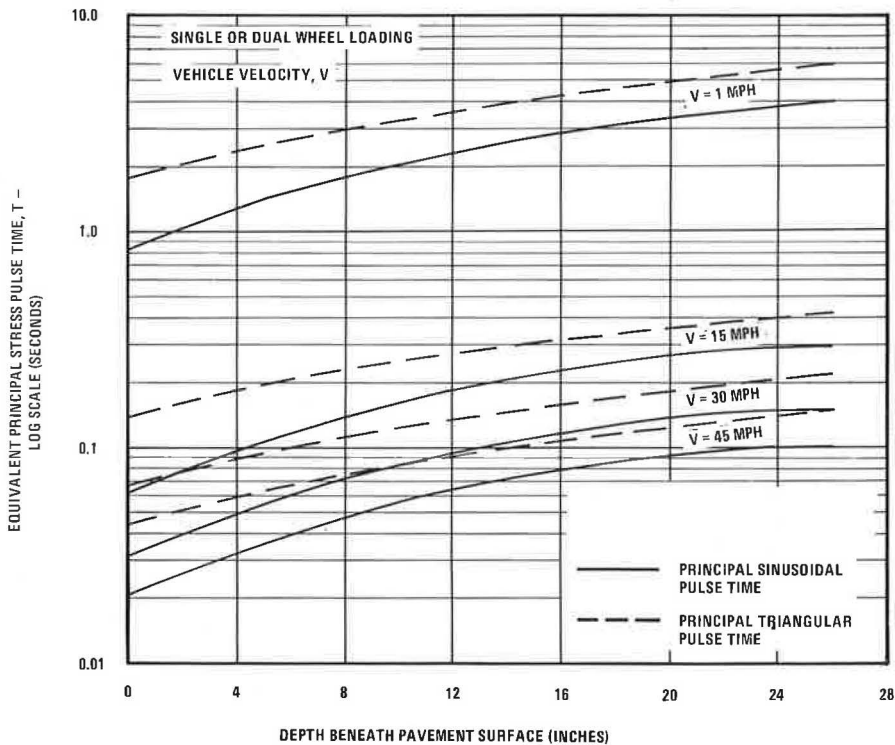


Figure 10. Variation of equivalent principal stress pulse time with vehicle velocity and depth.

literature (12). The following comparisons are made for a flexible pavement system consisting of a 5-in. asphalt concrete surfacing, 6-in. unstabilized crushed stone base, 12-in. sand-gravel subbase, and a compacted silty clay subgrade. Peak vertical pressures and the corresponding leading and tailing distances to zero pressure were measured at the top of the subgrade embankment.

Only the results of the measurements made using a 22.4-kip single-axle, dual-wheel loading moving at a creep speed were compared with the elastic theory. Inertia forces and viscous effects in the field measurements were minimized by making this comparison using the values measured for a creep vehicle speed. The average distance from zero pressure to the peak pressure measured at the Road Test was 49.7 in. for these conditions. The corresponding average measured distance from the peak to zero pressure was 57.0 in. The distance from zero to peak pressure calculated for the AASHTO Road Test conditions using the elastic finite element theory varies from a minimum value of 47.5 in. to a maximum of 57.0 in. depending on how the numerical results are interpreted. The extreme values of the theoretical results, therefore, agree closely with the extremes in the measured distances for the case of creep vehicle motion.

Because inertia forces and viscous effects are neglected when using the finite element theory, the calculated distance in which the pulse either builds up to a maximum or goes from the maximum value to zero does not vary with vehicle velocity. In the Road Test pavement system, however, these measured distances were found in the most extreme instance to increase by as much as 26 percent as the vehicle goes from a creep speed to a speed of 30 mph. To estimate the effects of inertia forces and viscous effects, all of the measured leading and tailing distances for both the 18- and 22.4-kip single-axle, dual-wheel loadings were averaged for each vehicle speed. Corresponding average correction factors to be applied to the creep distance were determined to be 1.11 and 1.13 for vehicle speeds of 15 and 30 mph respectively. By

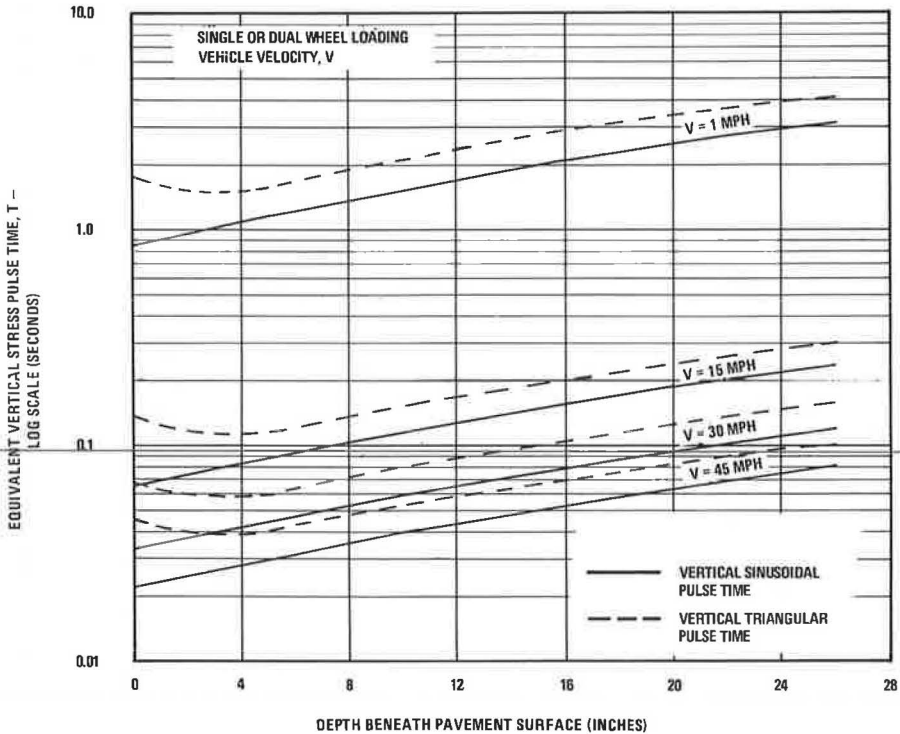


Figure 11. Variation of equivalent vertical stress pulse time with vehicle velocity and depth.

extrapolating these results, a correction factor of approximately 1.14 was obtained for 45 mph. The theoretically calculated values of the pulse times for a creep vehicle speed are assumed to be reasonably good, considering how favorably the calculated distances compared with the leading and tailing distances measured at the AASHO Road Test. Therefore, the stress pulse times obtained using elastic layered theory were not corrected for creep vehicle speeds. The correction factors for greater vehicle speeds obtained from the AASHO Road Test field measurements were applied to the stress pulse times derived from elastic theory.

A tabulation was made of the corrected stress pulse times for the pavement systems shown in Figures 6 through 8. A study of these pulse times indicated that for conventional flexible pavement sections, including deep strength designs and spring and summer temperatures, the equivalent stress pulse times at a given depth do not change significantly with different flexible pavement constructions. This approximation made it possible to summarize the results of this investigation in Figures 10 and 11. These figures give the variation of both the equivalent sinusoidal and triangular stress pulse times with vehicle velocity and depth beneath the pavement surface. These stress pulse times have been empirically corrected for viscous and inertia effects as previously discussed. The stress pulse times given are for a point located directly beneath the center of the load for a single-wheel loading and beneath the center of the assembly for single-axle, dual-wheel loadings.

DISCUSSION OF RESULTS

The repeated load test should be performed to duplicate as closely as possible the same stress conditions that an element of material will be subjected to in the field. This is true if the results are to be used to directly compare the performance of

of different materials, or if the evaluated material properties are to be used in a layered system or other type of theoretical analysis. By simulating the field stress conditions in the laboratory, the effects of material viscosity and inertia are at least partly accounted for in the evaluated material properties. Because rate-of-loading effects are not considered in the presently used elastic layered theory, it is indeed important that the material properties at least partly reflect viscosity effects. An element of material in the field is actually subjected to repeated stress pulses of different magnitudes caused by the variation in the position of the wheel loading across the pavement and by the application of widely varying wheel loadings. At the present time probably the most realistic way to handle varying wheel loadings in performing the repeated load test is to convert the mixed traffic to an equivalent number of 18- or 20-kip single-axle loadings. Certainly further study is needed on the effects of varying loads on the specimen.

The results of this study indicate that, in general, for conventional pavements having an asphalt concrete surfacing up to a thickness of about 5 in., a sinusoidal stress pulse should be applied to specimens simulating elements of material in the asphalt surfacing and the upper part of the base. For the thicker deep-strength or full-depth asphalt pavements, a sinusoidal stress pulse is probably appropriate only for elements in the middle and upper parts of the asphalt. Below these depths, a triangular-shaped stress pulse more nearly approximates the actual one. More complicated stress pulse forms are not, at the present time, considered necessary because of the many uncertainties associated with the use of layered theory.

In conducting a repeated load test, the choice arises as to whether to use the vertical stress pulse or the principal stress pulse. Probably for measuring the dynamic modulus of elasticity, the principal stress pulse would be the most appropriate because the modulus is usually defined in terms of principal stress systems, and principal stresses are normally applied in a triaxial cell. On the other hand, if the plastic properties of the material are desired to study rutting, possibly the vertical stress pulse would be more appropriate because the displacements of the pavement system are usually desired in the direction normal to the pavement surface.

CONCLUSIONS

The repeated load triaxial test more closely simulates the stress conditions that an element of material beneath a flexible pavement system feels than does the CBR test, the Hveem stabilometer test, or the conventional triaxial test. Therefore, the repeated load test or similar tests should become more commonly used in the future to predict pavement performance. The vehicle speed and depth beneath the pavement surface are of great importance in selecting the appropriate axial compressive stress pulse time to use in dynamic testing. For conventionally used flexible pavement sections, including deep-strength asphalt concrete structures and spring and summer temperatures, the stiffness and depth of each layer have only a small influence on the duration of the stress pulse. The influence of these factors can be neglected at the present time for practical engineering purposes. In addition, the axial stress pulse duration for a single- and dual-wheel loading can be considered to be approximately the same although the duration of the stress pulse caused by the dual-wheel loading is slightly less. As a consequence of these simplifying relationships, the equivalent sinusoidal and triangular stress pulse times for vehicle speeds up to 45 mph can be given as a function of vehicle velocity and depth beneath the pavement surface (Figs. 10 and 11).

The stress pulse times given in this paper were obtained using a linear elastic layered theory. The theoretically calculated stress pulse times were empirically corrected for inertia and viscous effects by using data obtained from the AASHO Road Test. Nevertheless, as more reliable field data are obtained and more refined methods of analysis become available, the pulse times recommended in this paper should be re-examined and also extended to include vehicle speeds greater than 45 mph.

ACKNOWLEDGMENT

The author would like to express his appreciation to W. M. Sangster, Director of the School of Civil Engineering, the Georgia Institute of Technology, for providing financial support for this investigation. Acknowledgment is also given the personnel of the Rich Electronic Computer Center for their assistance. The figures were prepared by P. H. Griggs.

REFERENCES

1. Deacon, J. A., and Monismith, C. L. Laboratory Flexural-Fatigue Testing of Asphalt-Concrete With Emphasis on Compound Loading. Highway Research Record 158, 1967, pp. 1-31.
2. Kallas, B. F., and Riley, J. C. Mechanical Properties of Asphalt Pavement Materials. Proc. Second Internat. Conf. on the Structural Design of Asphalt Pavements, Univ. of Michigan, 1967.
3. Seed, H. B., and Fead, J. W. N. Apparatus for Repeated Loading Tests on Soils. ASTM, STP No. 254, 1959, pp. 78-87.
4. Larew, H. G., and Leonards, G. A. A Strength Criterion for Repeated Loads. HRB Proc., Vol. 41, 1962, pp. 529-556.
5. Grainger, G. D., and Lister, N. W. A Laboratory Apparatus for Studying the Behavior of Soils Under Repeated Loading. Geotechnique, Vol. 12, No. 1, 1962, pp. 3-14.
6. Dorman, G. M. The Extension to Practice of a Fundamental Procedure for Design of Flexible Pavements. Proc. Internat. Conf. on the Structural Design of Asphalt Pavements, Univ. of Michigan, 1962, pp. 785-793.
7. Barksdale, R. D., and Leonards, G. A. Predicting Performances of Bituminous Surfaced Pavements. Proc. Second Internat. Conf. on the Structural Design of Asphalt Pavements, Univ. of Michigan, 1967.
8. The AASHO Road Test: Report 6—Special Studies. HRB Spec. Rept. 61F, 1962.
9. Barksdale, R. D. Analysis of Layered Systems. School of Engineering, Georgia Inst. of Technology, 1969.
10. Salvadori, M. G., and Baron, M. L. Numerical Methods in Engineering. Prentice-Hall, Englewood Cliffs, N. J., 1961.
11. Duncan, J. M., Monismith, C. L., and Wilson, E. L. Finite Element Analysis of Pavements. Highway Research Record 228, 1968, pp. 18-33.
12. The AASHO Road Test. HRB, Spec. Repts. 61A-61G, 1962.
13. Hicks, R. G. Oral communication, Aug. 1970; Factors Influencing the Resilient Properties of Granular Materials, paper presented at HRB 50th Annual Meeting and published in this Record.
14. Barksdale, R. D. Unpublished research, Georgia Inst. of Technology, 1970.

ANALYSIS OF STRESSES AND DISPLACEMENTS IN THREE-LAYER VISCOELASTIC SYSTEMS

J. F. Elliott and F. Moavenzadeh, Department of Civil Engineering,
Massachusetts Institute of Technology

A solution technique is presented for the analysis of the stresses and displacements induced in a viscoelastic three-layered body subject to boundary loads with different time configurations. The technique used is composed of two parts: (a) the use of a modified correspondence principle in the form of hereditary integrals to convert the elastic solution (to a boundary value problem with time-boundary conditions of the Heaviside type) to the viscoelastic solution, and (b) the use of the principles of the response of linear systems to imposed excitations to obtain the viscoelastic solutions to boundary value problems with time-boundary conditions other than the Heaviside type. The underlying principles of this method are discussed, and an example of the use of the method in the analysis of the stresses and displacements induced in a three-layer viscoelastic body subjected to uniformly distributed normal loads of the stationary, repeated, and moving types is presented.

•THIS PAPER presents a method of stress analysis for pavement structures by representing it as a three-layer mathematical model. The model is capable of predicting the response of the pavement to the following three sets of variables: (a) the mechanical properties of the materials in the layers, (b) the loading characteristics, and (c) the geometric parameters. Under heading (a) the quality of each layer and that of the combination of layers is considered. Under heading (b) the pertinent parameters used are the magnitude of the load, its duration (static, repeated, moving), and the frequency of the repetition. Under heading (c) the thickness of each layer, the offset distance of the load, and the location of the point of interest are considered.

STATEMENT OF PROBLEM AND METHOD OF SOLUTION

The geometrical model selected is a multilayered, semi-infinite half space consisting of three distinct layers as shown in Figure 1. It is assumed that the material properties of each layer can be characterized as linear elastic or linear viscoelastic. The load is considered to be uniform, normal to the surface, and acting over a circular area. The following loading conditions are considered:

1. A stationary load is applied and maintained at the surface (Fig. 1).
2. A repeated load is applied with a specified frequency to the surface of the pavement (Fig. 2).
3. A load travels at a constant velocity V along a straight path on the surface of the system (Fig. 3).

The variables of interest are the components of the stress tensor and the displacement vector at any point in the system.

The results for the normal deflection on the surface are presented in detail in this paper. [The other stress and deflection components can be determined in a similar manner (4).]

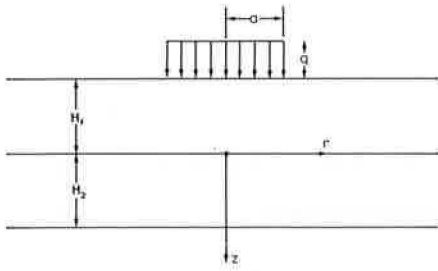
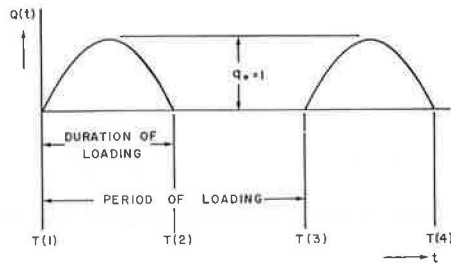


Figure 1. Cross section of three-layer system.



WHERE $Q(t) = q_0 \sin \omega t, 0 < t < \frac{1}{2}(\text{PERIOD OF SINE WAVE})$
 $0, \frac{1}{2}(\text{PERIOD OF SINE WAVE}) < t < (\text{PERIOD OF EXCITING FORCE})$

Figure 2. Time-varying repeated load configuration.

The correspondence principle is used to obtain the viscoelastic solution for the stationary load case. In addition, the principle of the response of initially relaxed linear systems to imposed excitations is used to obtain the solutions for the moving and repeated load boundary conditions. This method of analysis has been selected largely because the viscoelastic behavior of the system materials is assumed to be represented by stress-strain relations of the linear and nonaging type, using hereditary integrals.

The steps involved in this analysis consist of the following:

1. Obtaining the elastic solution for the surface deflection of the system due to a stationary applied load (2).
2. Applying the "correspondence principle" to the above solution, in the form of hereditary integrals for the stress-strain relations, to obtain the viscoelastic solutions (2).
3. Obtaining the viscoelastic solution for the surface deflection due to the repeated and moving loads, through the use of Duhamel's superposition integral for linear systems.

The Stationary Load

The solution for the surface deflection of a three-layer linear elastic half space was first derived by Burmister (1) for an incremental boundary load $-mJ_0(mR)$. The present analysis uses, for mathematical convenience, an incremental boundary load $-J_0(mR) J_1(ma)$. The resulting expressions are then integrated from 0 to ∞ with respect to m, and multiplied by qa to yield the correct response of the system to the following boundary stress:

$$\sigma_z \Big|_{z = -H_1} = -qa \int_0^\infty J_0(mR) J_1(ma) dm \quad (1)$$

where

q = intensity of the applied load, and
 a = the radius of the loaded area.

$J_0()$ and $J_1()$ are Bessel functions of the first kind zero and first order respectively.

Using this approach, the stationary load solution for the surface deflection of a pavement

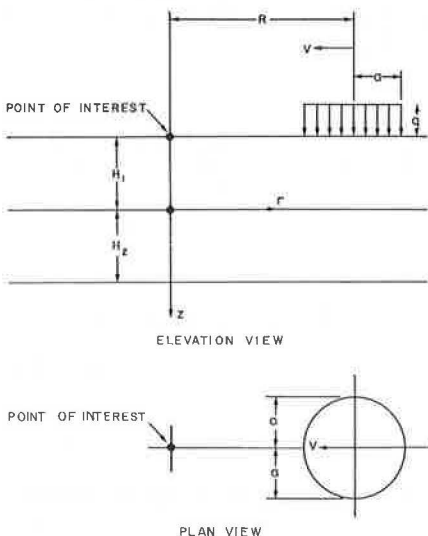


Figure 3. Moving load on viscoelastic half space.

system with elastic layers is given by the following equation:

$$W_S(r, -H_1) = qa \int_0^\infty \frac{H m}{m} \psi(m, -H_1) dm \quad (2)$$

where

- $H m = J_0(mR) J_1(ma)$ product of Bessel functions,
- $\psi(m, -H_1)$ = a rational function of elastic constants and their products,
- m = a dummy variable of integration,
- R = the offset distance at which a solution is desired, and
- $-H_1$ = the value of the Z coordinate at the surface of the layered system.

To obtain the viscoelastic solution, the stress-strain relations of the viscoelastic layers are assumed to be of the following form:

$$\begin{aligned} \epsilon_i(R, Z, t) = & D_{CRP_i}(0) \sigma_i(R, Z, t) \\ & - \int_0^t \sigma_i(R, Z, \tau) \frac{\partial}{\partial \tau} D_{CRP_i}(t - \tau) d\tau \end{aligned} \quad (3)$$

where

- $D_{CRP_i}(t)$ = creep function of each layer ($i = 1, 2, 3$),
- $\epsilon_i(R, Z, t)$ = strain at location (R, Z) at time t , and
- $\sigma(R, Z, t)$ = stress at location (R, Z) at time t .

The equivalent creep compliance for each layer in the viscoelastic domain will then be given in an integral operator form as

$$D_{CRP_i}(t) = D_{CRP_i}(0) () - \int_0^t () \frac{\partial}{\partial \tau} D_{CRP_i}(t - \tau) d\tau \quad (4)$$

When the correspondence principle (3) is applied to the elastic solution through the use of the creep integral operator in Eq. 4 for each layer, the viscoelastic solution for the surface deflection under a stationary load is obtained as

$$W_S(R, -H_1, t) = qa \int_0^\infty \frac{H m}{m} \psi(t, m, -H_1) dm \quad (5)$$

The surface deflection is time-dependent and the variable responsible for this time-dependence is $\psi(t, m, -H_1)$, which is the viscoelastic counterpart of $\psi(m, -H_1)$ in Eq. 2. If the mechanical properties of the system are changed, $\psi(t, m, -H_1)$ also changes.

The surface deflection $W_S(R, -H_1, t)$ due to a step load of intensity q applied to the surface of the system is a step response function of the system. It can be used when convolved with a time-varying load other than the step type applied to the boundary of the system to obtain the surface deflection for the new time-varying loading condition.

The Repeated Load Solution

Given $W_S(R, -H_1, t)$ as the response of the linear viscoelastic system to a step loading, the response due to a repeated load $Q(t)$ can be determined from the following superposition integral:

$$W_R(R, -H_1, t) = \int_0^t \frac{\partial Q(t)}{\partial \tau} W_S(R, -H_1, t - \tau) d\tau \quad (6)$$

[The lower limit of the integral accounts for the discontinuities that may initially exist in $Q(t)$ or $W(R, -H_y, t)$.]

Figure 2 shows the repeated loading pattern used in this study where

$$Q(\tau) = \begin{cases} \sin W\tau & \text{for } [(N-1) \text{ period}] \leq \tau \leq [(N-1) \text{ period} + \text{duration}] \\ 0 & \text{for } [(N-1) \text{ period} + \text{duration}] \leq \tau \leq [(N) \text{ period}] \end{cases}$$

for any number of repetitions N of the applied load ($N = 1, 2, 3, \dots$). A repetition of load is completed at the end of every period of application.

In this study, $W_S(R, -H_y, t)$ has been represented by a finite series of exponential terms of the form $\sum_{i=1}^n A_i \exp -(t - \tau) \delta_i$. The method of determining the coefficients of A_i and the exponents δ_i of such a series has been described in detail elsewhere (4, Appendix II).

The Moving Load Solution

When the load moves with a constant velocity V along a straight path on the surface (Fig. 3), the argument R in function $J_0(mR)$ of Eqs. 2 and 5 is $R - Vt$, where R is the offset distance of the load at zero time. The incremental load exciting the system will have the form $-J_0[m(R - V\tau)]J_1(ma)H(t - \tau)$ for loading and $+J_0[m(R - V\tau)]J_1(ma)H(t - \tau_1)$ for unloading ($>\tau_1 >\tau$), where $H(t)$ is the Heaviside step function.

This form of loading thus corresponds to the summation of all such incremental terms over time. By integrating them over m and multiplying by qa the total boundary load is obtained in the following form:

$$\sigma_Z \Big|_{Z = -H_1} = -qa \int_0^\infty J_1(ma) \left\{ \sum_{i=1}^{N-1} J_0[m(R - V\tau_i)] [H(t - \tau_i) - H(t - \tau_{i+1})] + J_0[m(R - V\tau_N)] H(t - \tau_N) \right\} dm \quad (7)$$

Then for appropriate values of $\Delta\tau = \tau_{i+1} - \tau_i$, the discrete load application given above corresponds to the continuous application of a moving load. The response for this case in terms of the surface deflection at location $(R, -H_1)$ due to a moving load is given by

$$W_M(R, -H_y, t) = qa \int_0^\infty \left\{ \frac{J_1(ma)}{m} \sum_{i=1}^{N-1} J_0[m(R - V\tau_i)] [\psi(m, H_y, t - \tau_i) - \psi(m, H_y, t - \tau_{i+1})] + J_0[m(R - V\tau_N)] \psi(m, H_y, t - \tau_N) \right\} dm \quad (8)$$

from which the solution at any time t_N can be obtained.

In this arrangement again the $\psi(m, H_y, t - \tau_i)$ terms have been represented by finite exponential series of the form $\sum_{j=1}^m G_j \exp -t\alpha_j$ where G_j and α_j are determined using techniques previously described (4, Appendix II).

RESULTS

The following presentation is divided into two sections. A discussion is first presented on the dimensionless system parameters that describe the pavement system. Then the capabilities of the model are discussed with the aid of several typical pavement structures.

Dimensionless Pavement Parameters

The pavement in this analysis is defined as a three-layer structure with a given set of dimensionless variables (Fig. 4). Each layer is incompressible, and the material in each layer is represented by a dimensionless creep compliance function. For ease of computation and use, the normalizing factor for the creep compliance of each layer is the value of the creep compliance of the third layer at infinity, $D_3(\infty)$.

All the components of the stress tensor at any point in the structure are expressed in terms of the intensity of the load. For the components of the displacement vector, the normalizing factor is the product of the intensity of the load q , the creep function of the third layer at infinity $D_3(\infty)$, and the height of the first layer H_1 .

The following geometric variables are considered: the offset distance of the load R , the heights of layers one and two, H_1 and H_2 respectively, the depth of interest Z , the radius of the loaded area A —all of which are presented in dimensionless forms in terms of the height of the first layer. In addition, all times are dimensionless and in terms of an arbitrary time factor, τ .

The Model Response

The response of the model is discussed in three sections. First, the influence of the mechanical properties of the layers on the response of various pavement systems is discussed. Next, the influences of the loading variables on the response of two pavement systems are considered. Third, the influences of the geometric variables are discussed.

The Mechanical Properties of the Layer Materials—Four different pavement systems were selected to investigate the effect of the mechanical properties of the materials used in each layer on the response behavior (Fig. 5).

The material in each layer is assumed to be incompressible, linear, homogeneous, and isotropic. Due to the lack of availability of meaningful real data, the four systems used for the discussion are selected to demonstrate qualitatively the influence that the material properties may have on the pavement response. For this reason, no absolute values are given for the magnitude of the creep function of any layer in any of the systems used.

System 1 is composed of completely elastic materials. System 2 is completely viscoelastic. Layer one in system 3 is viscoelastic, and the second and third layers are considered elastic. System 4 is assumed to be partially viscoelastic by considering that only the third layer is viscoelastic.

System 2 (Fig. 4) is used as the basis for comparison. In this system each layer is viscoelastic and the creep compliance function of each layer has the same value at infinity. This provision serves as a check on the results of the static loading condition. At very large times, the creep functions of the three layers have the same value; the system acts as a homogeneous elastic half space and Boussinesq's elastic solution should thus be obtained.

In dimensionless form, systems 2 and 4 have the same initial values for the dimensionless creep functions $[D(t)/D_3(\infty)]$ in their respective layers; systems 1 and 3 also have the same initial values for the dimensionless creep functions in their respective layers.

Vertical Deflection—Figure 6 represents the vertical deflection under the center of the loaded area on the first interface for systems 1 through 4. It was mentioned before

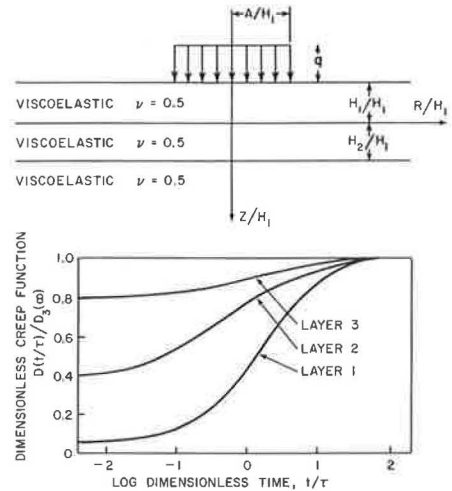


Figure 4. Dimensionless pavement system 2.

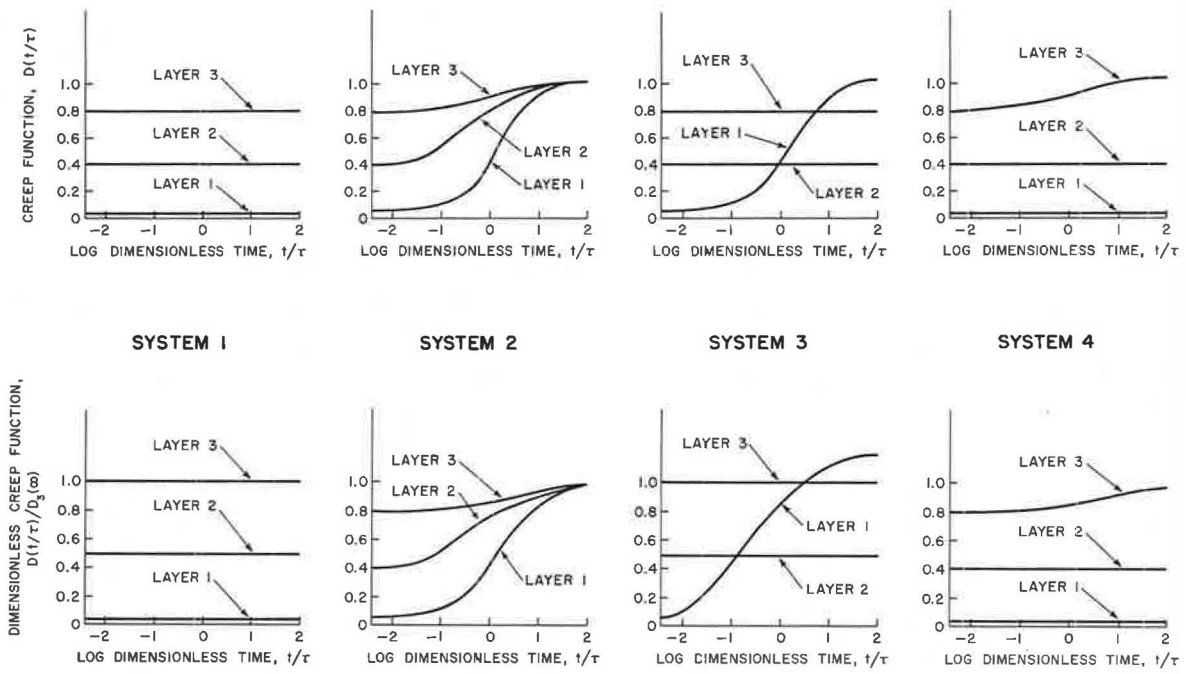


Figure 5. Creep function for systems 1 through 4.

that the zero time value of the creep functions for systems 1 and 3 are the same; therefore at zero time (not shown because of the logarithm scale) the two systems undergo the same magnitude of deflection. However, as the load is maintained, system 3 continues to deflect more because of the viscoelastic characteristics of its top layer. This shows the effect of the stiffness of the first layer on the deflection. The stiffer the surface material, the lesser is the deflection of the pavement.

Systems 2 and 4 have the same initial values of deflection. System 2, however, accumulates more deflection than system 4. Because the third layers of both systems possess the same mechanical properties, the discrepancy in results must be due to the uppermost layers; this supports Burmister's conclusion that when better quality materials are used in the base and surface course of the pavement, the pavement provides a blanket effect around the subgrade.

All the systems shown in Figure 5 are elastic at long times with system 4 displaying the least deflection factor and system 2 the greatest. In terms of stiffness, at long times system 2 is the weakest of all the systems and, therefore, deflects the most. Because systems 2 and 3 are later used to investigate the influence of the loading conditions and geometric variables on the mechanical response, it will be worthwhile to examine them more closely at the present time.

For very small values of time, system 2 is stiffer than system 3. Therefore, at short loading times the deflection factor for system 2 is less than that for system 3 when loads of the same magnitude are used. With the passage of time, however, system 2 becomes less stiff when compared to system 3. From the shape of the deflection curves, this occurs at dimensionless time of approximately one. When this event occurs, the deflection factor on the first interface of system 2 exceeds that of system 3 and continues to do so until it reaches a plateau.

For the stress (Fig. 7), however, system 3 consistently displays higher values of developed stresses than system 2 except at very short times where the stresses of system 2 are greater than those for system 3 (not shown in the figure). The reason for

this behavior is that the two lower layers of system 3 are elastic and have stiffness values that do not change with time. The stresses developed on the first interface of system 3 increase considerably with time because of the rigidity of the bottom two layers. The lower layers of system 2 offer no such resistance; therefore, the stresses developed are not as great as those for system 3.

Vertical Stresses—Figure 7 shows the curves obtained for the vertical stress factor on the first interface for systems 1, 2, 3, and 4 (Fig. 5). The stresses similar to vertical deflection start with the same initial values for systems 2 and 4 and for systems 1 and 3.

However, while the stress on the first interface of system 2 increases with time,

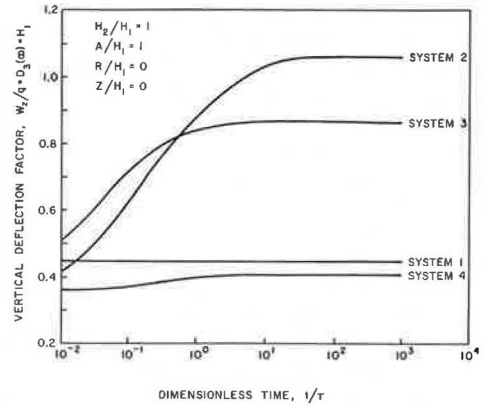


Figure 6. Influence of material variables on vertical deflection factor—4 systems.

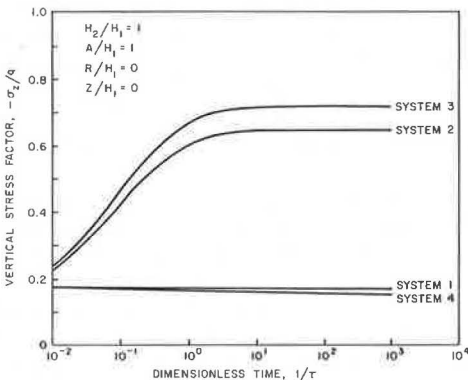


Figure 7. Influence of material variables on vertical stress factor—4 systems.

that on system 4 decreases. This may be because the stiffness of the upper two layers of system 4 remains fixed while that of the lower layer decreases with time. The overall effect is to cause a decrease in the stresses on the first interface. For elastic system 1, the stresses remain constant with time as expected.

In Figure 7, the stresses developed on the first interface of system 3 exceed those of system 2. This increase is due to the differences between the two systems, which resulted in a difference in their vertical deflections shown in Figure 6.

Shear Stress—Figure 8 shows the effect of the mechanical properties of the layer materials on the shear stress developed on the first interface directly under the edge of the loaded area. The effect is almost similar to that for vertical stress except for system 4, where the shear stress slightly increases with time while the normal stress showed a slight decrease. This may be because the deflection on the interface under the axis of the load is increasing, causing an increase in the curvature of the interface. This would cause an increase in the shear stress because such stresses, as Burmister shows, are deflection dependent (6).

The results indicate that the nature of the system response depends on the mechanical characteristics of the materials in the layers. The interaction between the material properties of each layer produces what may be called a system function that is not only a function of the location of the point of interest but also of the kind of the response function being investigated (i. e., a stress or a deformation output).

Loading Conditions—The vertical stress, the vertical deflection, and occasionally the shear stress are presented to investigate the effect of the loading conditions and geometric variables.

The Stationary Loading Condition—For the stationary loading condition, the magnitude of the components of the stress and displacement factors generally increases with the increase in dimensionless time factor for all systems, as shown in Figures 6, 7, and 8 for vertical deflection, vertical stress, and shear stress respectively.

It is interesting to note that for both systems 2 and 3 the magnitude of all the three responses tends toward an asymptotic value at a value of dimensionless time corresponding to that when the dimensionless creep compliance functions become asymptotic. The system response therefore depends on the response characteristics of the layer materials. The extensive variation in stress and deformation with time under the constant load for both systems is a marked contrast to the constant distribution (of these quantities) exhibited by a structure with elastic properties. This phenomenon may have an important influence in the design of such structures. The rational design of the structural components (especially those exhibiting viscoelastic response) should, therefore, use the complete history of the stress and displacement distribution, rather than a single value of these components.

At values of dimensionless time greater than 1,000, the magnitudes of the stress and displacement components are equal to those obtained when the system behavior is elastic; i. e., the mechanical properties of the materials in the layers are equivalent to those of the given creep functions at infinity.

This capability serves as a check on the validity of the viscoelastic representations because the results thus obtained are comparable to those acquired by other authors for elastic systems having the appropriate properties. The model can therefore account for the manner of variation of all the pertinent stress and deflection factors at any point in three-layer pavement structure for this boundary condition.

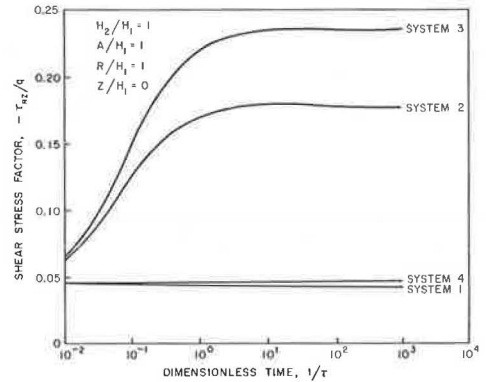


Figure 8. Influence of material variables on shear stress factor—4 systems.

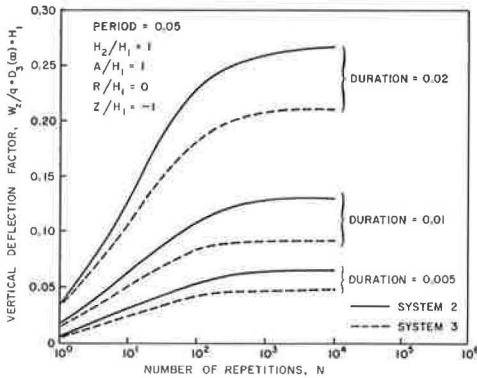


Figure 9. Influence of duration of vertical deflection factor.

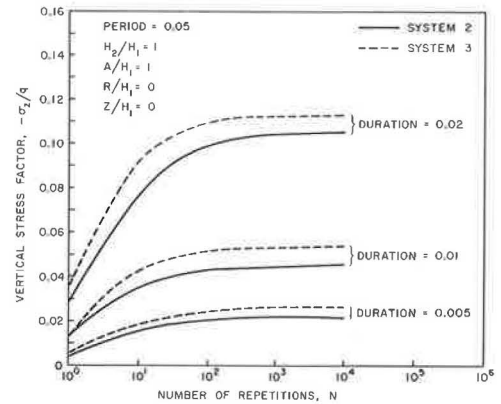


Figure 10. Influence of duration on vertical stress factor.

The Repeated Loading Condition—For this loading condition, the influence of the duration and period of the loading on the response of systems 2 and 3 was investigated using the vertical deflection on the surface directly under the center of the loaded area and the vertical stress on the first interface.

A load repetition is considered to be completed at the end of the period of the loading (see Fig. 2), and the magnitude of the stress or deflection factor is measured at this time. The results that are presented for a dimensionless period of 0.05 and durations of the loading equal to 0.005, 0.01, and 0.02 can be noted in Figures 9 and 10; the stress and deflection factors of the systems increase with increasing number of load repetitions.

Figure 9 shows the results obtained for the vertical deflection on the surface. The magnitudes of the deflection factor for system 3 are consistently lower than those for system 2. This indicates that system 2 behaves more viscously, a result that is evident from the dimensionless creep compliance functions for this system (Fig. 4).

Figure 10 shows the curves obtained for the vertical stress factors on the first interface. The stresses developed in system 3 are again consistently higher than those for system 2. This is because, for the same load, the system that is stiffer will develop the greater stresses. An examination of the creep functions for systems 2 and 3 in Figure 5 shows system 3 to be stiffer than system 2.

For each system, the greater the duration of the loading the greater is the developed stress or deflection factor. This indicates that the severity of the structural response is directly related to the duration of the loading. The longer the load remains on the system, the greater is the damaging effect.

The Moving-Load Condition—Figures 11 through 13 show the manner in which systems 2 and 3 respond to the application of a moving load traveling with a constant velocity along a straight line on the surface (see Fig. 3). The curves in Figure 11 are for the vertical deflection on the surface. The vertical stress

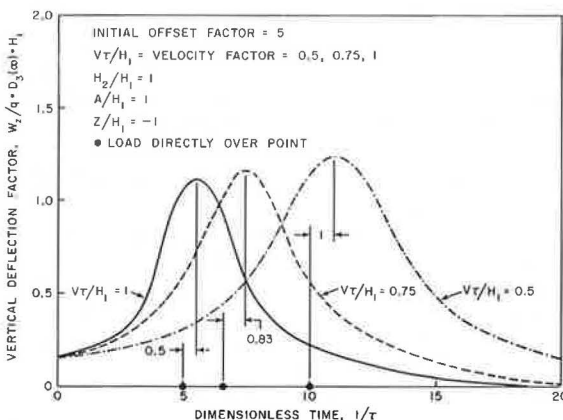


Figure 11. Moving load—vertical deflection factor, system 2.

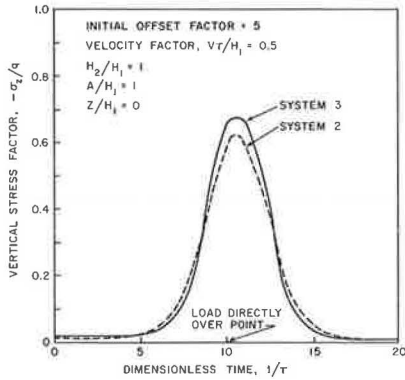


Figure 12. Moving load comparison—vertical stress factor.

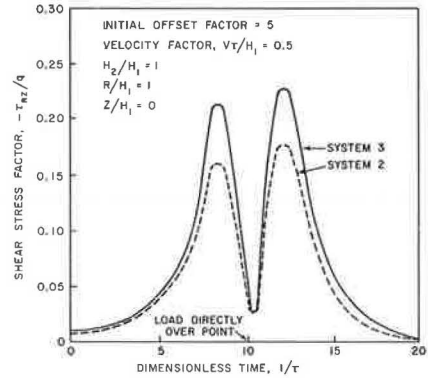


Figure 13. Moving load comparison—shear stress factor, systems 2 and 3.

and the shear stress on the first interface are shown in Figures 12 and 13 respectively.

The curves indicate that the system response in terms of stress and deflection factors is not symmetrical with respect to time. The viscoelastic behavior of the systems is such that there is a time lag between the observance of a response and the time of application of the agent causing it. Therefore, at the time when the load is directly over the point of interest, the magnitudes of the response in terms of stress and deflection factors are not at the maximum. In addition, it must be noted that the maximum value of either stress or deflection factor is obtained after the load has passed over the point.

The observed time lag in the viscoelastic responses is also velocity dependent. The greater the velocity of the moving load, the smaller is the time lag. This velocity dependence is discussed using the solutions obtained for the vertical deflection of systems 2 and 3. Figure 11 shows the curves obtained for the vertical deflection of system 2. It is seen that the peak deflection of the system increases with decreasing velocity factors, indicating that the longer the load remains within the region of influence the greater is the damaging effect that it has on a point of interest within the structure. It is also interesting to note that the lag in response time increases with decreasing velocity factors, for these same reasons. The same behavior is displayed by system 3.

The results obtained for the vertical stress and shear stress factors on the first interface of systems 2 and 3 also show a consistent behavior as indicated in Figures 12 and 13 respectively. In the case of the shear stress factor, however, there are two peaks in the curve. This indicates that as the load approaches the point the shear stress builds up to some limiting value and starts to decrease. At the time when the load is directly over the point, the shear stress is zero. However, the superposition of effects from previous loads actually prevents the total shear stress from going to zero. The effect of the decrease is to cause a marked reduction in the shear stress. As this load moves away from the point, the shear stress builds up again to a maximum peak and decreases.

The Geometric Variables—The height factor, depth factor, radius factor, and offset distance factor are discussed in the following paragraphs.

The Height Factor of the Second Layer—The influence of the height factor on the system response is investigated using the vertical deflection factor on the surface of systems 2 and 3 when they are subjected to repeated loading.

Figure 14 shows that for both systems the deflection increases with the number of repetitions for a fixed value of the height factor. The deflection factors for a given number of repetitions, however, decrease with increasing H_2/H_1 , indicating that the thicker the system, the lower are the deflections. An alternative method of lowering surface deflection is to have stiffer materials in the layers, as was discussed earlier.

The dependence of the surface vertical deflection factor on the height factor of the second layer is more marked for system 3 than for system 2. For system 3, this marked dependence is displayed at every load repetition. At lower numbers of load repetition the dependence is pronounced. At higher levels it is absent. This is not surprising when the mechanical properties of system 2 are taken into account (Fig. 5). Because all the creep functions of system 2 tend toward the same value at long times, one would expect the system to become homogeneous eventually. When this occurs, the deflection at the surface is independent of H_2/H_1 because the system is a semi-infinite homogeneous mass.

The Depth Factor—The influence of the depth factor is investigated using the vertical deflection under the center of the loaded area. The curves so obtained for both systems 2 and 3 are shown in Figure 15. There is a marked reduction in vertical deflection through the layers as shown in this figure. The reduction is greater as the number of load repetitions increases. For points within the third layer, an increase in the number of repetitions does not cause significant increase in the deflection. However, this effect is more severe for points that are nearer to the point of load application.

The Radius Factor—The effect of the radius factor was investigated using the vertical deflection factor on the first interface directly underneath the load (Fig. 16). The curve generally indicates that, as the radius of the loaded area is increased, the deflection is accordingly increased. Again system 2 deflects more than system 3 for reasons previously discussed.

The damaging effect on the first interface increases considerably with the increase in the size of the loaded area confirming the rather obvious result that for a given period and duration of loading heavier loads do more damage than lighter ones.

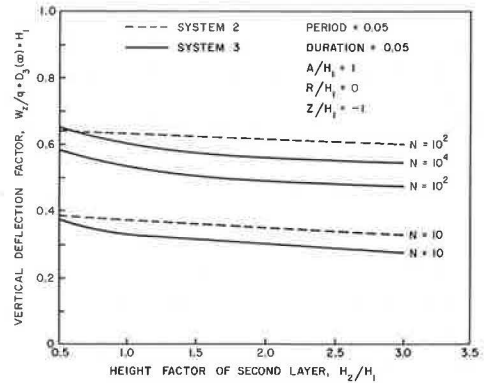


Figure 14. Influence of height factor on vertical deflection factor.

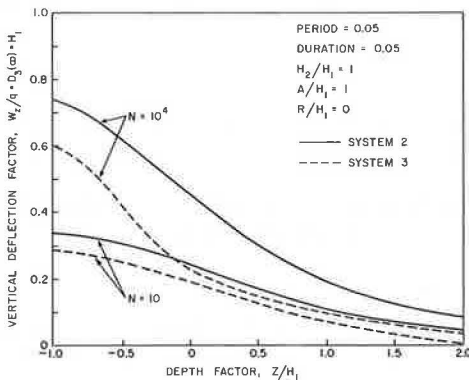


Figure 15. Influence of depth factor on vertical deflection factor.

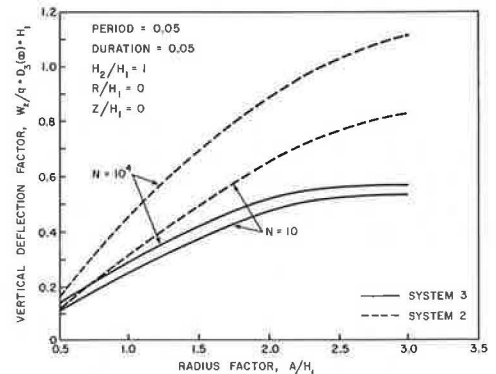


Figure 16. Influence of radius factor on vertical deflection factor.

The Offset Distance Factor—Figure 17 shows that the surface deflection factor decreases with increasing offset distance for both systems 2 and 3. This result is what is expected: the effect of the applied load is more severe near the point of interest.

SUMMARY AND CONCLUSIONS

The preceding discussion has served to emphasize the fact that the physical characteristics of the pavement system depend, among other things, on geometric measurements such as thickness, arrangement of the component layers, and the basic properties that characterize material behavior. The system response consequently involves the behavior of the physical structure when it is subjected to load and climatic inputs. When these act on the system, a condition that describes the mechanical state results. Measurable quantities such as the deformation and stress are then acquired. These quantities are calculated in this study based on the assumption that the material in each layer is linear viscoelastic.

The model presented accounts for the response behavior of a three-layer linear viscoelastic system. It is capable of predicting the response of pavement structures in terms of the developed stresses and displacements at any location.

In the development of the model, however, several assumptions were made. For instance, the effects of inertia and the fact that the real structure has finite geometrical boundaries are neglected. The materials in layers are assumed to be linear, homogeneous, and isotropic. The validity of such assumptions must therefore be further investigated.

In addition, the determination of realistic inputs other than material properties into a suitable model for the stress and deformation analysis should be investigated. A proper and adequate identification of the characteristics of the applied load and the determination of appropriate failure criteria for existing pavement structures would aid in this area.

The present viscoelastic analysis is believed to be a step in the right direction primarily because, unlike the linear elastic analysis, the rate and accumulation effects, the influence of parameters such as the duration of loading, the system geometry, the system properties, and the load configuration on the mechanical response of the system can all be accounted for.

ACKNOWLEDGMENT

The work reported here was sponsored by the U.S. Department of Transportation, Federal Highway Administration, under a project entitled "Moving Load on a Viscoelastic Layered System Phase II."

The opinions, findings, and conclusions expressed in the publication are those of the authors and not necessarily those of the Federal Highway Administration.

REFERENCES

1. Burmister, S.M. The General Theory of Stresses and Displacements in Layered Soil System, I, II, III. Jour. Appl. Phys., Vol. 16, No. 2, pp. 80-96; No. 3, pp. 126-127; No. 5, pp. 296-302, 1945.
2. Ashton, J. E., and Moavenzadeh, F. Linear Viscoelastic Boundary Value Problems. Jour. Eng. Mech. Div., Proc. ASCE, Feb. 1968.

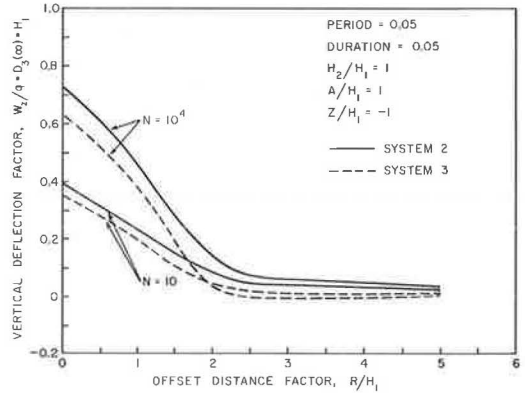


Figure 17. Influence of offset distance factor on vertical deflection factor.

3. Bland, D. R. *Linear Viscoelasticity*. Pergamon Press, London, 1960.
4. Elliott, J. F., and Moavenzadeh, F. *Moving Load on Viscoelastic Layered Systems, Phase II*. Dept. of Civil Eng., M.I.T., Cambridge, Research Rept. R69-64, Sept. 1969.
5. Tobolsky, A. V. *Stress Relaxation Studies of the Viscoelastic Properties of Polymers*. *Jour. Appl. Phys.*, Vol. 27, No. 7, July 1956.
6. Burmister, Donald M. *Application of Layered System Concepts and Principles to Interpretations and Evaluations of Asphalt Pavement Performances and to Design and Construction*. *Internat. Conf. on Structural Design of Asphalt Pavements*, Univ. of Michigan, 1962.

STRESSES AND DISPLACEMENTS IN AN ELASTIC MASS UNDER ASSUMED AND MEASURED TIRE PRESSURES

Y. T. Chou, Pavement Research Laboratory,
U.S. Army Engineer Waterways Experiment Station, Vicksburg, Mississippi

•IN ANALYTIC STUDIES of pavement structural design, a common assumption has been that vehicle tires transmit uniformly distributed pressure to the supporting medium over a circular area. Experimental studies on firm and soft surfaces conducted at the U.S. Army Engineer Waterways Experiment Station (WES) have shown that the pressure distribution pattern is approximately uniform only when the tire-inflation pressure is very low, the tire walls are very flexible, and the supporting medium (soil) is very soft (1, 2). Although the assumption of uniform pressure distribution results in mathematical convenience and simplification, the question arose as to the magnitude of the deviation in stress and displacement within the medium caused by the simplified assumption.

The primary purpose of this study was to compare the differences in the magnitudes of vertical stresses and vertical displacements in the supporting medium arrived at by computations based on assumed and measured tire pressures. Using the theory of elasticity, computations were made for various points along the vertical axis originating at the centroid of the vertical pressure and also along the vertical axis under the higher edge pressure in cases of low-pressure tires. The computations for the uniform pressure distributions were based on circular and rectangular contact areas. Also, assumed parabolic pressure distributions over circular contact areas were investigated.

EVALUATION OF ASSUMED UNIFORM PRESSURE PATTERNS

The pressure distributions under pneumatic tires were measured in the mobility facility at WES. Test tires consisted of an 11.00-20 buffed smooth tire and a 12-22.5 treaded tire. Analysis was made only with tires of 12-ply rating, which is commonly used for tires for military land vehicles. Measurements were made in soft soils (sands and clays) with a towed (about 1 mph) smooth tire and on a hard surface under both static and towed conditions. At one test load, the measurements were made at three different tire-inflation pressures. In soft soils, each soil was tested at three different levels of strength in terms of cone index, which is the force (lb) per unit area (sq in.) required to move a 30-deg, right circular cone of 0.5-sq-in. base area through the soil at a rate of 72 in. per min.

Because the measured pressure distribution under a tire is not expressed analytically, an approximation procedure was applied to use the elastic equations. The tire print was divided into many small areas, depending on smoothness of the pressure distribution, and each area was considered as a concentrated load in the computation. Poisson's ratio ν was assumed to be 0.25.

For uniform pressure distribution, the idealized rectangular and circular contact areas had the same area as the actual tire prints. For uniformly loaded rectangular areas, the widths were chosen equal to those of the actual tire prints, and the lengths were computed accordingly.

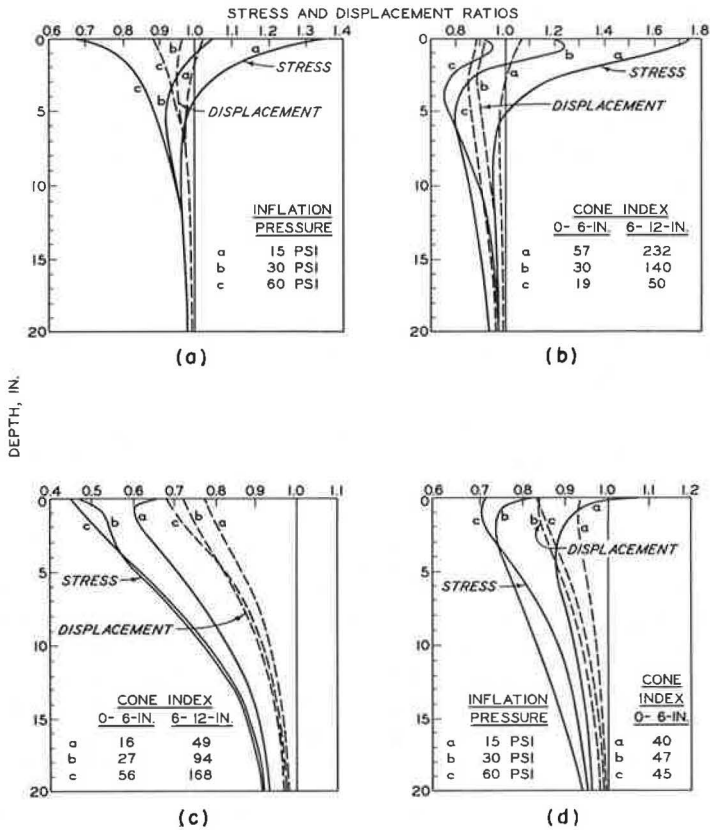


Figure 1. (a) 11.00-20 smooth tire, 3,000-lb load, wheel towed on firm surface; (b) 11.00-20 smooth tire, 15-psi inflation pressure, 3,000-lb load, wheel towed on sand; (c) 11.00-20 smooth tire, 60-psi inflation pressure, 3,000-lb load, wheel towed on sand; and (d) 11.00-20 smooth tire, 3,000-lb load, wheel towed on clay.

Because computed results for uniformly distributed pressures were nearly identical for circular and rectangular areas, only the results for uniform rectangular loads are presented here. The computed results are expressed as ratios of assumed-to-measured conditions, and the ratios are plotted for various depths (Fig. 1). Worthy of note is the fact that differences in stress are much more pronounced than those in displacements.

The stress and displacement ratios for an 11.00-20 smooth, towed tire at three different inflation pressures and loaded to 3,000 lb are shown in Figure 1a. The plotted curves show that the computed stress ratios were much higher than unity for a low-pressure tire; the situation was reversed for a high-pressure tire. In the latter case, the vertical stress on the surface under uniform pressure was 66 percent of the stress induced by the measured pressure distribution. The computed displacement ratios for a low-pressure tire were near unity but were less than unity for a high-pressure tire; however, the difference was not large within the test range.

The pressure distribution patterns for the 11.00-20 tire under static conditions were very similar to those for the same towed tire; thus the computed results were quite close to those for the rolling tire and, therefore, are not presented. Also, the pressure distribution patterns for a 12-22.5 treaded, tubeless tire in the static condition and loaded to 2,800 lb were similar to those used to derive Figure 1a. The computed

results for these cases represented were also quite close and, consequently, are not presented.

Because relatively high pressures were measured near the edge of the contact area, computations were made along the vertical axis under the higher edge pressure, and the results were compared with those along the vertical axis under the center of the uniform pressure distribution, where maximum stress and displacement would occur. The computed stress and displacement ratios were slightly larger than unity, except at upper regions, where the stress ratios were much less than unity.

Results for a low-pressure tire (15 psi) loaded to 3,000 lb and towed over sand of three different strengths are shown in Figure 1b. The sand conditions ranged from loose to dense. The stress ratios were much greater than unity when the supporting sand had high penetration resistance, but decreased and became less than unity when the penetration resistance decreased. The displacement ratios were near unity for high penetration resistance, but became less than unity as the penetration resistance decreased.

Results in Figure 1c are from tests conducted under similar conditions as those shown in Figure 1b, the only difference being the higher tire-inflation pressure (60 psi) for the tests in Figure 1c. The pressure distribution patterns had shapes similar to a parabola. The computed ratios were much less than unity.

Computations were also made for a low-pressure tire (15 psi) towed over a loose sand under the three different loads (1,500, 3,000, and 4,500 lb). The computed stress and displacement ratios were close to unity under the heaviest load, but became less than unity as the load decreased. For a high-pressure tire (60 psi) tested in the similar conditions, the pressure patterns were very much like those used to develop Figure 1c. The results are not presented in this paper but have been published elsewhere (3). Results for tests with a tire loaded to 3,000 lb and towed over a soft clay at three different inflation pressures are shown in Figure 1d. In general, the pressures beneath the tire were distributed more uniformly in clay than in sand. The plotted results show that, at low inflation pressure, the computed stress and displacement ratios were near unity but tended to become less than unity as the inflation pressure increased.

EVALUATION OF ASSUMED PARABOLIC PRESSURE PATTERNS

The stresses computed for measured pressure distributions on a firm surface tended to draw closer to those computed for the equivalent parabolic pressures as the tire-inflation pressure was increased. For the cases analyzed at a high inflation pressure (60 psi), uniform pressure distribution appears to be more realistic than the parabolic one. For measured pressure distributions in sand, the computed stresses were close to those computed for the parabolic pressure distributions for high-pressure (60 psi) tires; however, for low-pressure (15 psi) tires, this conclusion applies only to loose sand and light load. In these cases, the parabolic pressure distributions appear to be more realistic than uniform pressure distributions.

CONCLUSIONS

For high-pressure tires on a hard surface and on sands, the stresses in the former case and the stresses and displacements in the latter case computed from measured pressure distribution are much higher than those computed from an assumed uniform pressure distribution. The assumption of uniform pressure distribution on clay is reasonable provided that the tire-inflation pressure is low. The assumption of parabolic pressure distribution is found to be more realistic than that of a uniform one for high-pressure tires on sands and for low-pressure tires with light load on loose sand.

REFERENCES

1. Green, A. J., McRae, J. L., and Murphy, N. R. Stresses Under Moving Vehicles; Distributions of Stresses on an Unyielding Surface Beneath Stationary and Towed Pneumatic Tires. Technical Report No. 3-545, Report 4, U.S. Army Engineer Waterways Experiment Station, Vicksburg, Miss., July 1964.

2. Freitag, D. R., Green, A. J., and Murphy, N. R. Normal Stresses at the Tire-Soil Interface in Yielding Soils. Miscellaneous Paper 4-629, U.S. Army Engineer Waterways Experiment Station, Vicksburg, Miss., Feb. 1964.
3. Chou, Y. T. Effect of Pressure Distribution Under Pneumatic Tires on Stresses and Displacements in the Supporting Elastic Media. Miscellaneous Paper M-70-6, U.S. Army Engineer Waterways Experiment Station, Vicksburg, Miss., May 1970.

NEW METHOD FOR DETERMINATION OF TENSILE STRENGTH OF SOILS

H. Y. Fang and W. F. Chen, Department of Civil Engineering, Lehigh University

This paper describes a new and simple test technique for determining the tensile strength of soils. A cylindrical soil specimen is used by applying two steel punches at the center on both top and bottom surfaces of the specimen. Based on the perfect plasticity theory, a simple formula for computing the tensile strength of soils is developed. The fundamental relationship between tensile strength and environmental variables is examined. The comparisons of tensile strength determined from double punch tests and split tensile tests for various materials including concrete, mortar, and bituminous concrete are presented. It is concluded that the double punch test could be used easily for both laboratory and field to determine the tensile characteristic of soils.

•TENSILE STRENGTH of soil is one of the important strength parameters in the field of soil mechanics. However, engineers often consider that the tensile strength of soil is assumed to be zero because it is a relatively small value compared with compression strength and because of the lack of a satisfactory measuring technique.

The importance of cracking failure related to the tensile strength of materials in many highway pavements and earthfill dams has been given considerable attention in recent years. Leonards and Narain (14) developed a laboratory measuring technique to measure the tensile-bending stress of soil by use of clay-beam and to predict the cracking behavior of earth dams. George (10) has applied the theory of brittle fracture to evaluate the cracking growth and the effects on stabilized soil-cement.

For measuring the tensile strength of material, the split tensile test has been widely used for concrete (1, 5, 20) and has been extended to measure the tensile strength of bituminous concrete (4, 15), lime-stabilized soil (16), and soil-cement (12, 13). Tschebotarioff et al. (18) and Winterkorn (19) have used a modified Briquet Gang Model type to measure the tensile strength of various clay minerals. Recently, Chen (7, 8) proposed a double punch test that has been suggested as an alternative test method for determination of tensile strength of concrete.

The purpose of this paper is to develop both theoretically and experimentally the application of a double punch test to cohesive soils, which includes (a) development of an equation based on the perfect-plasticity theory that the tensile strength of soil can be computed; (b) development of the fundamental relations between tensile strength and environmental variables; and (c) comparisons of tensile strength results determined from double punch tests and split tensile test for various materials including concrete, mortar, and bituminous concrete.

DESCRIPTION OF DOUBLE PUNCH TEST

Using two steel discs centered on both top and bottom surfaces of a cylindrical soil specimen, the vertical load is applied slowly on the discs until the specimen reaches failure. The tensile strength of the specimen can be calculated from the maximum load by the theory of perfect plasticity. Schematic diagrams and photographs of the double punch test are shown in Figures 1 and 2.

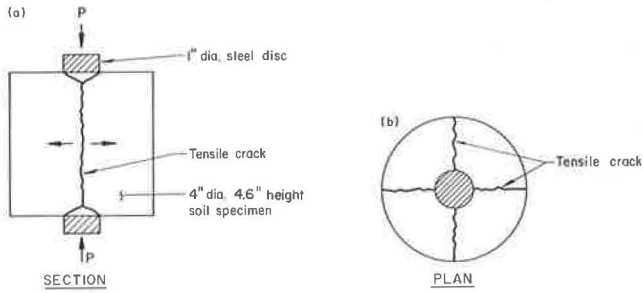
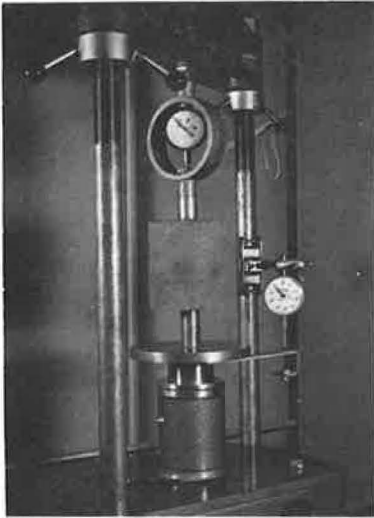
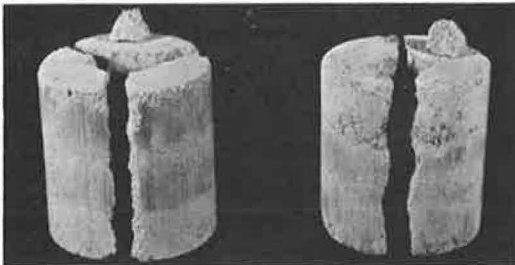


Figure 1. Schematic diagram of a double punch test.

The effect of the sample size and the dimensions of the disc have been studied by Hyland and Chen (11). Based on the test of concrete and mortar, they have found that the effect of height-to-diameter ratio and disc size on the tensile strength is approximately a linear relation. Fang (9) has found that a height-to-diameter ratio of the specimen varying from 0.8 to 1.2 and a ratio of diameter of the specimen to the diameter of the disc varying from 0.2 to 0.3 are suitable for this test. For convenience, the Proctor mold (4 by 4.6 in.) and CBR mold (6 by 6 in.) with 1 in. and 1.33 in. (CBR piston) disc respectively are recommended (9). For this study the Proctor mold was used for preparation of the soil specimen with a 1-in. diameter disc. The disc should be rigid so that no bending occurs during the loading test.



(a)



(b)

Figure 2. A double punch test: (a) test setup; and (b) modes of failure.

THEORETICAL ANALYSIS

The theoretical basis of the formula for computing the tensile strength of a split tensile test has been derived from the theory of linear elasticity (17). It has the simple form

$$\sigma_t = \frac{2P}{\pi Ld} \quad (1)$$

where

- σ_t = simple tensile strength, psi;
- P = applied load, lb;
- L = length of specimen, in.; and
- d = diameter of specimen, in.

It has been shown recently by limit analysis (7) that an identical formula of the problem can also be derived from the theory of perfect plasticity. A plasticity treatment of the double punch test for the concrete has been developed by Chen (8), and results for predicting the bearing capacity of concrete and rock are available (6, 7, 11). It would appear that the same

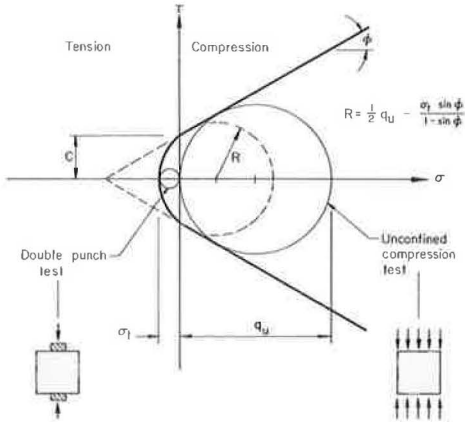


Figure 3. Modified Mohr-Coulomb criterion.

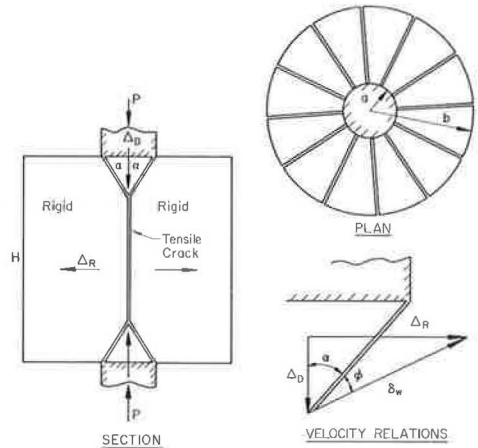


Figure 4. Failure mechanism of a double punch test.

theory should be applicable to the soil double punch test because the bearing capacity behavior for soils can be closely related to the bearing capacity behavior of concrete blocks or mortar.

The theory cited by Chen and Drucker (6) is based on two assumptions. The first assumption is that sufficient local deformability of soils in tension and in compression does exist to permit the application of the generalized theorems of limit analysis to soils idealized as a perfectly plastic material. The second assumption is that a modified Mohr-Coulomb failure surface in compression and a small but non-zero tension cutoff is postulated as a yield surface for soils (Fig. 3). In Figure 3, q_u , σ_t , c , and ϕ denote the unconfined compression, simple tension strength, cohesion, and the internal friction angle of the soil respectively.

Figure 4 shows an ideal failure mechanism for a double punch test on a cylinder specimen. It consists of many simple tension cracks along the radial direction and two cone-shaped rupture surfaces directly beneath the punches. The cone shapes move toward each other as a rigid body and displace the surrounding material sideways. The relative velocity vector δ_w at each point along the cone surface is inclined at an angle ϕ to the surface (6). The compatible velocity relation is also shown in Figure 4. It is a simple matter to calculate the areas of the surfaces of discontinuity. The rate of dissipation of energy is found by multiplying the area of each discontinuity surface by σ_t times the separation velocity $2\Delta_r$ across the surface for a simple "tensile" crack or $q_u(1 - \sin \phi)/2$ times the relative velocity δ_w across the cone-shaped rupture surface for simple "shearing" (6). Equating the external rate of work to the total rate of internal dissipation yields the value of the upper bound on the applied load P,

$$\frac{P}{\pi a^2} = \frac{1 - \sin \phi}{\sin \alpha \cos (\alpha + \phi)} \frac{q_u}{2} + \tan (\alpha + \phi) \left(\frac{bH}{a^2} - \cot \alpha \right) \sigma_t \quad (2)$$

in which α is the as yet unknown angle of the cone, a is the radius of the punch, and b and H are the specimen dimensions (Fig. 4).

The upper bound has a minimum value when α satisfies the condition $\partial P^u / \partial \alpha = 0$, which is

$$\cot \alpha = \tan \phi + \sec \phi \left[1 + \frac{\frac{bH}{a^2} \cos \phi}{\frac{q_u}{\sigma_t} \left(\frac{1 - \sin \phi}{2} \right) - \sin \phi} \right]^{1/2} \quad (3)$$

valid for

$$\alpha \geq \tan^{-1} \left(\frac{2a}{H} \right)$$

and Eq. 2 can be reduced to

$$\frac{P}{\pi a^2} = \sigma_t \left[\frac{bH}{a^2} \tan(2\alpha + \phi) - 1 \right] \quad (4)$$

Using typical values of $q_u = 10 \sigma_t$ and $\phi = 20$ deg, and assuming $2a = 1$ in., $2b = 4$ in., and $H = 4.6$ in., the upper bound has a minimum value at the point where $\alpha = 14.2$ deg, and Eq. 4 gives

$$P \leq P^u = \pi (1.12 bH - a^2) \sigma_t \quad (5)$$

It is found that the value of the coefficient 1.12, which appeared in Eq. 5, is not too sensitive to the internal friction angle ϕ . For example, ϕ varies from 0 to 30 deg and the value of the coefficient varies from 0.84 to 1.32 respectively. The average value of the coefficient is 1.08.

As concluded by Chen and Drucker (6), the upper bound solution so obtained is in fact close to the correct values. It seems, therefore, reasonable to take

$$\sigma_t = \frac{P}{\pi (1.0 bH - a^2)} \quad (6)$$

as a working formula for computing the tensile strength in a double punch test for all soils.

LABORATORY EXPERIMENTS

Specimen

Medium plasticity soil (liquid limit = 31, plasticity index = 10) was selected for the study. Soil samples passed No. 10 sieves and were air-dried. A 4- by 4.6-in. Proctor mold was used for preparation of the soil specimen. Specimens were compacted in three layers with a 5.5-lb hammer and 12-in. drop; 15, 25, and 55 blows per layer were applied. For the double punch test the procedures were followed as suggested by Fang (9). One-inch diameter steel discs were used as shown in Figures 1(a) and 2(a). The rate of load application was 2 in. per min. Simultaneously, duplicated specimens were made for the split tensile test (2) and unconfined compression test (2, 3).

Test Results

The load-deflection data and maximum load were recorded for all tests, which include double punch, split tensile and unconfined compression tests. The test results are shown in Figures 5 through 10. The double punch tensile strength was computed from Eq. 6 where $b = 2$ in.,

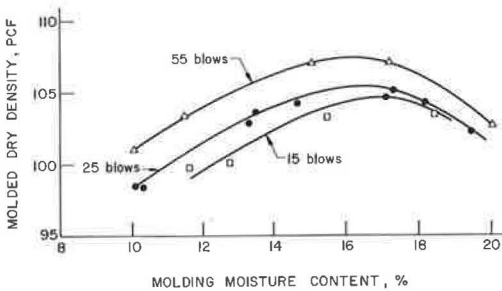


Figure 5. Molded dry density versus molding moisture content.

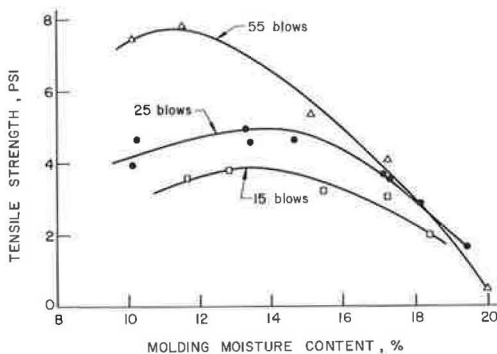


Figure 6. Tensile strength versus molding moisture content.

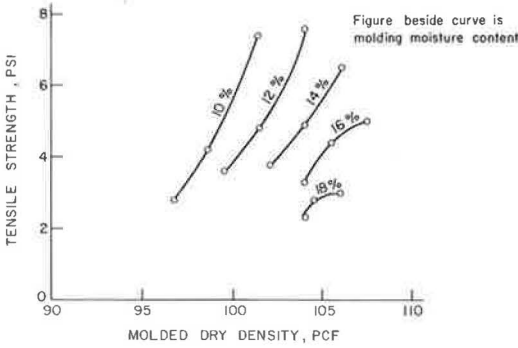


Figure 7. Tensile strength versus molded dry density.

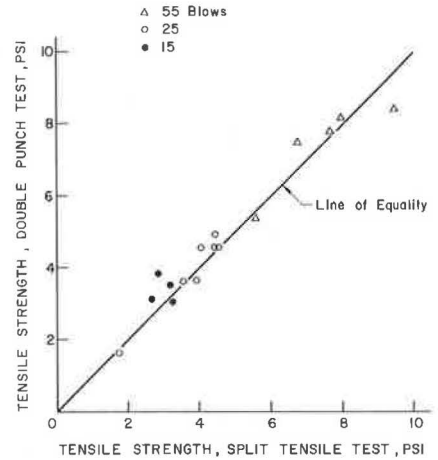


Figure 8. Comparisons of tensile strength of soil determined by double punch and split tensile tests.

H = 4.6 in., and a = 0.5 in. The split tensile strength was calculated from Eq. 1 where L = 4.6 in. and d = 4 in. For both equations, P is the maximum load for the specimen. The cracking pattern for the double punch test is shown in Figures 1(b) and 2(b). The cone-shaped formation with 2- or 3-piece cracks is generally observed for the soils.

Figure 5 shows the density-moisture content relationships with three compactive efforts. Figure 6 shows the tensile strength versus molding moisture content with various compactive efforts and indicates that maximum tensile strength exists on the dry

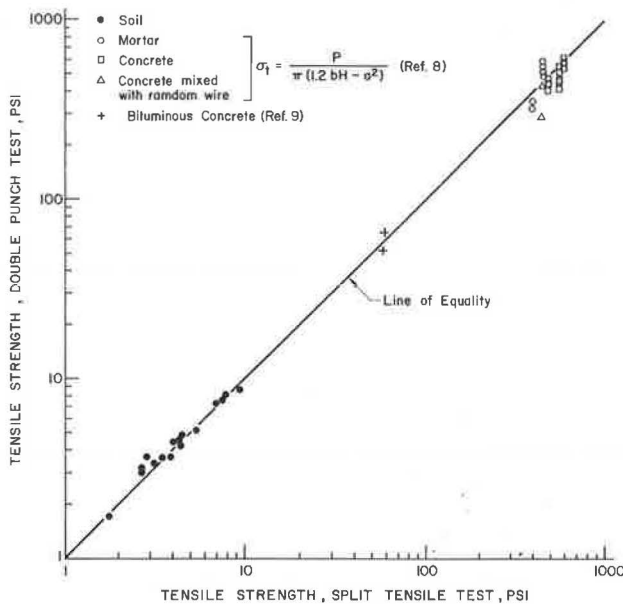


Figure 9. Comparison of tensile strength of various materials determined by double punch and split tensile tests.

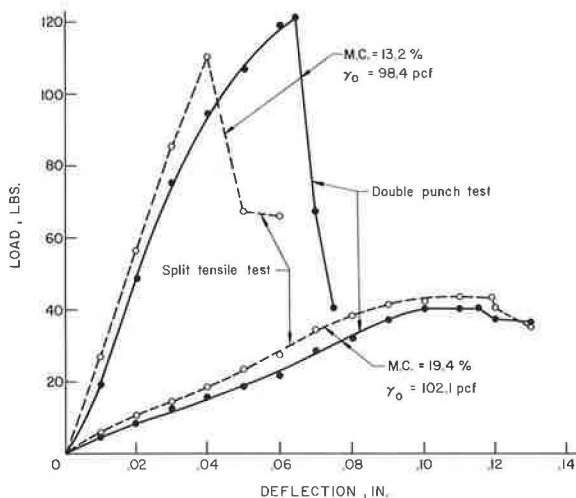


Figure 10. Load-deflection curves.

side of the optimum moisture content. Figure 7 was interpreted from Figures 5 and 6 and indicates that, at higher moisture content, as density increases the tensile strength increases slightly; however, at lower moisture content, as density increases, the tensile strength increases sharply.

Figures 8 and 9 show the comparisons of the tensile strength determined by double punch and split tensile tests. Figure 8 shows only one type of soil with various molding moisture contents and compactive efforts. However, Figure 9 shows the tensile strength of soil comparisons with other materials such as concrete, mortar, and bituminous concrete. Good agreement between two tensile strength test results is indicated. Figure 10 shows the typical load-deflection curves for both double punch and split tensile tests. For all the cases, the similar load-deflection patterns were found for both double punch and split tensile tests.

SUMMARY AND CONCLUSIONS

1. The double punch test is a simple test and easy to perform. No additional equipment is needed for the test, which could be tied in with routine CBR or compaction tests.
2. Based on the plasticity theory, a simple equation (Eq. 6) has been developed for computing the tensile strength of soils. This equation agrees both theoretically and experimentally with the equation used for the split tensile test.
3. Higher tensile strength existed on the dry side of the optimum moisture condition.
4. When the cracking failure is significant, it is necessary to examine the tensile strength of the material. The double punch test can be used for both laboratory and field construction control.

ACKNOWLEDGMENTS

The work described in this paper was conducted in the Geotechnical Engineering Division, Fritz Engineering Laboratory, Lehigh University, as part of the research program on soil plasticity. This particular study is sponsored by the Envirotronics Corporation.

The experimental work for this study was performed by Humphrey C. S. Han and Eric Maurer.

REFERENCES

1. Akazawa, Tsuneo. Tension Test Method for Concrete. Union of Testing and Research Laboratories for Materials and Structures, Bull. 16, Nov. 1953, pp. 11-23.
2. ASTM. 1970 Annual Book of ASTM Standards, Part 11.
3. Bowles, J. E. Engineering Properties of Soils and Their Measurement. McGraw-Hill, New York, 1970, 187 pp.
4. Breen, J. J., and Stephens, J. E. Split Cylinder Test Applied to Bituminous Mixtures at Low Temperatures. ASTM, Jour. of Materials, Vol. 1, No. 1, March 1966.
5. Carneiro, Fernando L. L. B., and Aguinaldo, Barcellos. Tensile Strength of Concrete. Union of Testing and Research Laboratories for Materials and Structures, Bull. 13, March 1952, pp. 97-127.
6. Chen, W. F., and Drucker, D. C. Bearing Capacity of Concrete Blocks or Rock. Jour. of Eng. Mech. Div., Proc. ASCE, Vol. 95, No. EM4, Aug. 1969, pp. 955-978.
7. Chen, W. F. Extensibility of Concrete and Theorems of Limit Analysis. Jour. of Eng. Mech. Div., Proc. ASCE, Vol. 96, No. EM3, June 1970, pp. 341-352.
8. Chen, W. F. Double Punch Test for Tensile Strength of Concrete. ACI, Vol. 67, Dec. 1970, pp. 993-995.
9. Fang, H. Y. Method of Test for Tensile Strength of Soil, Rock, and Stabilized Materials by Double Punch Test. Lehigh Univ., Fritz Eng. Lab. Rept. 348.4, July 1970.
10. George, K. P. Theory of Brittle Fracture Applied to Soil Cement. Jour. of Soil Mech. and Found. Div., Proc. ASCE, Vol. 96, No. SM3, May 1970, pp. 991-1010.
11. Hyland, M. W., and Chen, W. F. Bearing Capacity of Concrete Blocks. ACI, Vol. 67, March 1970, pp. 228-236.
12. Kennedy, T. W., and Hudson, W. R. Application of the Indirect Tensile Test to Stabilized Materials. Highway Research Record 235, 1968, pp. 36-48.
13. Kezdi, A. Erddrucktheorien. Springer-Verlag, Berlin, 1962.
14. Leonards, G. A., and Narain, J. Flexibility of Clay and Cracking of Earth Dams. Jour. of Soil Mech. and Found. Div., Proc. ASCE, Vol. 89, No. SM2, March 1963, pp. 47-98.
15. Livneh, M., and Shklarsky, E. The Splitting Test for Determination of Bituminous Concrete Strength. Proc. AAPT, Vol. 31, 1962, pp. 457-476.
16. Thompson, M. R. The Split-Tensile Strength of Lime-Stabilized Soils. Highway Research Record 92, 1965, pp. 11-23.
17. Timoshonko, S. Theory of Elasticity. McGraw-Hill, New York, 1934, pp. 104-108.
18. Tschebotarioff, G. P., Ward, E., and DePhilippe, A. A. The Tensile Strength of Disturbed and Recompacteds Soils. Proc. Third Internat. Conf. on Soil Mech. and Found. Eng., Vol. 3, 1953, pp. 207-210.
19. Winterkorn, Hans F. The Science of Soil Stabilization. HRB Bull. 108, 1955, pp. 1-24.
20. Wright, P. J. F. Comments on an Indirect Tensile Test on Concrete Cylinders. Magazine of Concrete Research, Vol. 7, No. 20, July 1955, pp. 87-96.

PROBABILISTIC APPROACH TO THE DETERMINATION OF SAFETY FACTORS FOR THE BEARING CAPACITY OF COHESIVE SOILS

J. Neil Kay and Raymond J. Krizek, The Technological Institute,
Northwestern University

There are a number of considerations that influence the factor of safety to be used in the engineering design of a foundation resting on a cohesive soil. Broadly speaking, these may be divided into uncertainty considerations and cost considerations. The former pertain to the evaluation of applied loads, soil properties, and analytical procedures, whereas the latter are concerned with the cost of changing the foundation size and the total cost of failure, if it should occur. In this work, probability functions are used to represent these uncertainties, and a rational procedure is advanced to determine safety factors associated with the bearing capacity of cohesive soils.

•THE uncertainties associated with loading, soil properties, and analytical procedures render very difficult the estimation of a safety factor for the bearing capacity of a cohesive soil. To be sure, the experienced engineer with an appreciation of all three factors intuitively accounts for each when he applies the traditional formulas of soils engineering. However, to make a selection that is economically optimum and at the same time consistent with the various uncertainties involved, a certain number of failures would necessarily have to be experienced. In some engineering situations, failures are sufficiently common that it may be possible over a period of time to develop intuitive guidelines that would enable the selection of an appropriate value for safety factor. Such failures are usually associated with temporary construction procedures, wherein the relationship between cost of failure and savings obtainable by modification of design is concomitant with a somewhat higher than normal permissible frequency of failure. Other cases conducive to a higher frequency of failure occur where failure is not of a catastrophic nature; in such situations the cost of failure is usually relatively low and/or the failure itself is progressive in nature.

On the other hand, because catastrophic failures of permanent structures normally involve extensive loss of property, human life, and professional reputation, as well as the cost of replacement of the structure, a high degree of conservatism is necessarily used. As a result, the frequency of failure is extremely low and, although the experienced designer may be capable of selecting a safety factor that will provide for a safe structure, he may have difficulty in refuting any contention that this safety factor and its related costs are excessive. One example of this situation is the bearing capacity problem for structures on stiff clays. Although it is recognized that settlement may sometimes provide the design criterion in such cases, this work is concerned with the case in which bearing capacity is the critical mode of failure. Because bearing capacity failures under these conditions are extremely rare, it may be argued that safety factors in current use are perhaps too large, and money is being wasted. Of even greater significance, it is desirable for the designer to have some means of determining

quantitatively how the factor of safety varies with cost of foundation, cost of ultimate failure, degree of knowledge about the subsurface soil, uncertainty of the loading, and analytical procedures used. The individual evaluation of each of these factors poses a difficult problem; in some cases, a reasonably accurate determination is possible, whereas for other cases, only a subjective estimate may be made. However, even within these limitations, if values can be determined and properly analyzed as a group, the resulting procedure for determining a safety factor should be superior to the intuitive approach so commonly employed at present. Accordingly, this work will suggest one possible procedure for determining in a rational manner the bearing capacity of a cohesive soil.

BEARING CAPACITY FORMULATION IN PROBABILISTIC TERMS

The bearing capacity, q_d , of a shallow footing in or on a cohesive soil has been given by Skempton (1) as

$$q_d = 5c \left(1 + 0.2 \frac{D_f}{B} \right) \left(1 + 0.2 \frac{B}{L} \right) \quad (1)$$

For a 10-ft square footing embedded 5 ft, Eq. 1 would simplify to

$$q_d = 6.6c \quad (2)$$

or

$$A = \frac{L}{6.6c} = \frac{L_D + L_L}{6.6c} \quad (3)$$

where L is the total maximum load on the footing and A is the footing area. Traditionally, the footing area would be determined from the right-hand side of Eq. 3 by dividing the total load, which is composed of a dead load, L_D , and a live load, L_L , by a soil strength, c , which is determined by selecting a conservative value from the results of laboratory tests; then, the result so obtained is multiplied by a safety factor.

However, instead of evaluating Eq. 3 in the conventional deterministic manner just described, the load and strength parameters may be treated in a probabilistic manner, and $f(A)$, a probability distribution function for A , may be determined; the input functions would indicate the probability that strengths or loads may deviate from specified mean values, and the output function, $f(A)$, would indicate the probability that any given area represents the one that is critical from a stability point of view. Provided the input distribution functions are representative of the uncertainties associated with loading and soil strength and provided the theoretical formulation describes precisely the physical phenomenon being investigated, the area distribution function, $f(A)$, will be realistic. Although the uncertainties associated with loading can be represented directly, those associated with the ultimate soil strength on the failure plane combine various distributions, one of which may be obtained from laboratory tests, while the others are determined on a subjective basis. For example, if c represents the undrained shear strength measured in a laboratory test, it is a relatively simple matter to obtain an associated distribution function; however, there are a number of additional factors that must be considered when the ultimate shear strength on the failure plane in the field is desired. These include (a) sample disturbance, (b) the tendency for progressive failure, (c) the drainage conditions in the field and in the laboratory test, (d) the rates of loading in the field and in the laboratory test, and (e) the extent to which the specimens tested represent the actual soil on the failure plane.

Sample disturbance will normally decrease the soil strength, and a multiplying factor, D , is introduced to account for this effect; because of the uncertainty involved with determining the value of D , an associated probability function will be used. Similarly, progressive failure will normally lead to a reduction in ultimate strength, and a factor,

P, having an associated probability function, is introduced. This treatment applies specifically to the $\phi = 0$ design approach, and it presumes that strength values are obtained from undrained laboratory tests conducted at conventional rates of strain (on the order of 1 percent per minute). Although these conditions may represent reasonably well the case where a load is applied rapidly to a poorly draining soil, the slower rates of loading usually associated with building construction will make this approach somewhat conservative, owing to consolidation and the related increase in effective stress. Even though the undrained strength is generally less at lower rates of strain, this effect is usually overshadowed by the consequences of consolidation, and no account is taken of these effects in this study. As a consequence of the foregoing factors, it is extremely difficult, if not impossible, to evaluate the correctness of the bearing capacity formulation given by Eq. 1; therefore, it is necessary to provide for some uncertainty in this formulation, and a factor, T, having an associated probability function is included. Subject to the above modifications, Eq. 3 now becomes

$$A = \frac{L_D + L_L}{6.6c \times D \times P \times T} \quad (4)$$

EVALUATION OF AREA DISTRIBUTION FUNCTION

Although other distribution forms have been proposed, Wu and Kraft (2) have suggested that live loading may be represented by a normal distribution function; dead load may be considered as deterministic or, alternatively, also as normally distributed. Such assumptions permit the combination of loads to form a single load function on the basis of a total load, L, because normal distribution functions, when summed, produce a normal distribution having a mean value equal to the sum of the individual means and a variance equal to the sum of the individual variances. The relatively small significance of load distribution in the final result indicates that some inaccuracy in the assumptions of normal distributions for loading is not important.

The number of specimens tested and the degree to which these specimens represent the soil on the failure plane require careful consideration. Any evidence of geological factors that may provide a lower strength in the vicinity of the failure plane may dictate that the strength distribution be based on these specimens alone. In general, test specimens should be distributed throughout the entire region that encloses the theoretical failure zone. If the number of specimens is larger (30 or more), the distribution may be represented as normal with a mean, \bar{x} , equal to the sample mean and a standard deviation, S, given by

$$S = \sqrt{\frac{\sum (\bar{x} - x)^2}{n - 1}} \quad (5)$$

where x is the test value and n is the number of specimens. When there is a smaller number of specimens, an approximate approach may be taken if the coefficient of variation, V (ratio of standard deviation to the mean), is estimated for the region. If we consider a normal distribution with a mean, \bar{x} , equal to the sample mean, the standard deviation, S, may be expressed as

$$S = \frac{\bar{x} V}{\sqrt{n}} \quad (6)$$

Hooper and Butler (3) have reported consistent values of V for the strength of soil specimens taken from various sites, even though the mean strengths were different. Accordingly, a conservative value of V, based on previous work, may very well provide a more realistic estimate of the mean than the t distribution, another alternative for smaller sample numbers. The details of this approach, based on the coefficients of variation V, have been discussed by Kay and Krizek (4).

For the functions representing sample disturbance, progressive failure, and theory uncertainty, a purely subjective judgment of functional relationships must be made at this time. Accordingly, normal distribution functions, characterized as given in Table 1

and discussed subsequently, have been assigned to each phenomenon, and the respective assigned fixed functions have been used throughout this work.

In the case of sample disturbance, the data in Table 1 imply, for example, that there is a 50 percent chance that the measured strength should be increased by 33 percent to account for this phenomenon, a 16 percent chance that the strength should be increased by 18 percent, and a 5 percent chance that the strength should be increased by only 8 percent. The 33 percent value of mean probable strength increase is a somewhat subjective evaluation, but it is equivalent to the effects of sample disturbance found by Terzaghi (5) on the Chicago subway by use of careful sampling procedures. The spread of the distribution is purely subjective, but it seems reasonable.

For progressive failure, the tabulated values imply a 50 percent chance that progressive failure will reduce the soil strength by a factor of 0.67, a 10 percent chance that it will be reduced by 0.58, and a 5 percent chance that it will be reduced by 0.55. Again, these figures appear to indicate a reasonable choice of distribution form.

There is no real basis for knowing the accuracy with which the Prandtl solution predicts the bearing capacity of cohesive soils because it is difficult to evaluate the effects of progressive failure and measurement of soil properties. The selected distribution indicates a 16 percent chance that the required foundation area should be 10 percent larger than indicated by Prandtl, a 10 percent chance that it should be 15 percent larger, and a 5 percent chance that it should be 20 percent larger.

The selection of normal distributions for these cases is also purely subjective, and it is difficult to defend these selections except to point out that an analysis of the implications of such distributions has been made and the results have been judged subjectively to be reasonable.

The equation from which the area distribution function, $f(A)$, may be determined is now of the form

$$A = \frac{L}{6.6c \times D \times P \times T} \quad (7)$$

and each of the probability distribution functions associated with the variables, L and c , may have either its mean or its standard deviation varied. For a particular set of values, the Monte Carlo technique (6) may be used to obtain $f(A)$. A digital computer may be used to generate sets of random numbers sufficient in number (perhaps 50,000) to obtain a reliable functional form in the significant part of the function (Fig. 1). This function indicates the probability that any given area will be required, based on the probability distributions of the input parameters.

OPTIMIZATION OF FOUNDATION AREA

To determine the optimum design area for the foundation, two cost values are required; one is the estimated cost of a catastrophic failure of the foundation, and the other is the unit cost of variation in the footing size. In addition, the concept of including in the total cost an appropriate portion of the cost of failure of the foundation is required; this may be considered analogous to, or may in fact be, the appropriate insurance premium. The total cost of the structure, T , may be written in the form

$$T = U_{CF} \cdot A + C_F \cdot p(F) + B \quad (8)$$

where U_{CF} is the unit cost of the foundation, A is the foundation area, C_F is the total cost of failure of the foundation, $p(F)$ is the probability of failure for a given area A (obtained from the area distribution function), and B is the total remaining cost of the

TABLE 1
FIXED FUNCTIONS ASSIGNED

Function	Mean Value	Standard Deviation
Sample disturbance	1.33	0.15
Progressive failure	0.67	0.07
Theory precision	1.00	0.10

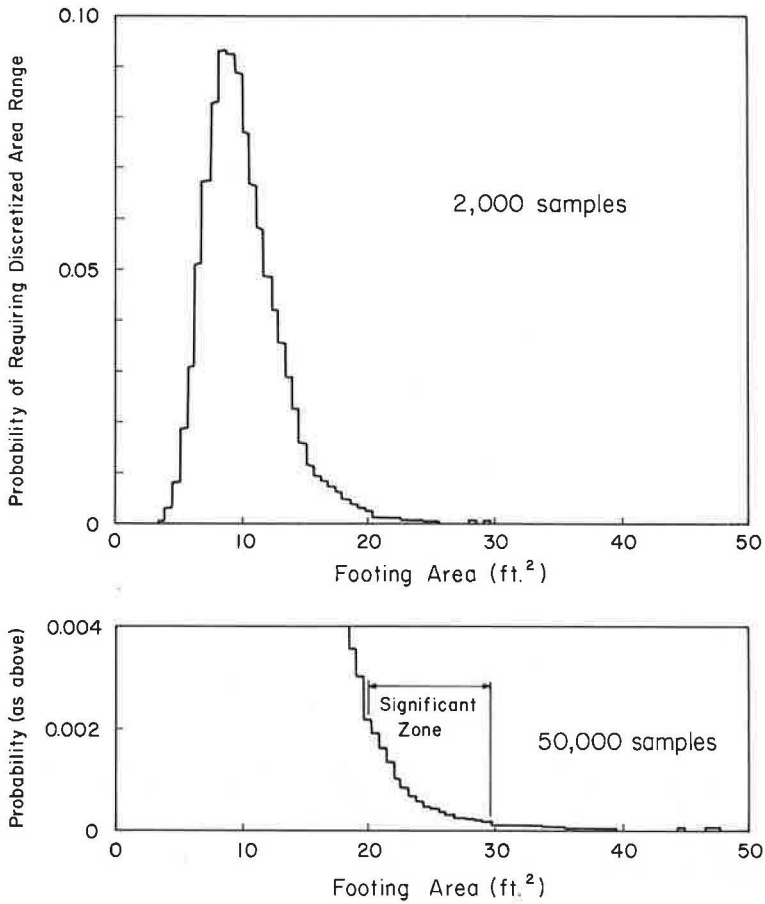


Figure 1. Area distribution diagram.

structure (which, for present purposes, may be considered constant). The total cost may be minimized by equating to zero the partial derivative of Eq. 8 with respect to area,

$$\frac{\partial T}{\partial A} = U_{CF} + C_F \cdot \frac{\partial p(F)}{\partial A} = 0 \quad (9)$$

and solving for R,

$$R = \frac{C_F}{A \cdot U_{CF}} = - \frac{1}{\frac{\partial p(f)}{\partial A} \cdot A} \quad (10)$$

where R is the ratio of the unit cost of the foundation failure to the unit cost of the foundation. Equation 10 is written specifically to show that the costs can be studied in the form of the dimensionless parameter R. Because the area distribution function formulation is not known, the optimum value for the area is obtained on the basis of Eq. 8; the computer is used to test progressively each discretized area value until the minimum total cost value is found.

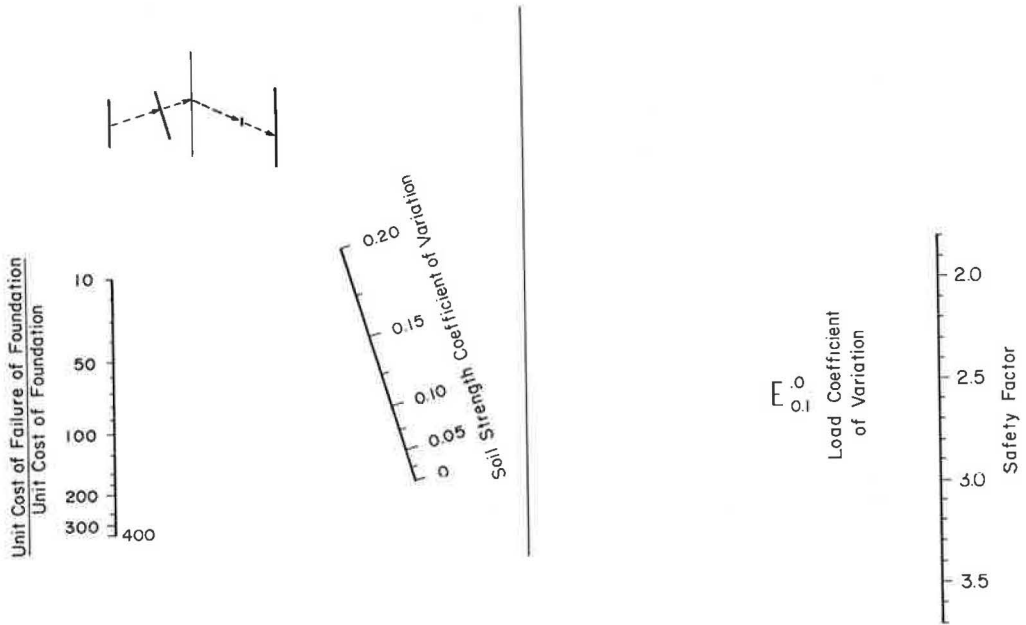


Figure 2. Safety factor nomograph for bearing capacity of cohesive soils.

Although the unit cost of the foundation, U_{CF} , is considered independent of the foundation area, A , in the preceding treatment, this may not be the case in many instances. However, the dependency will usually be slight, and a single repetition of the design process, using a unit cost compatible with the initially computed area, should be sufficient to account for such variations.

SAFETY FACTORS

With an optimum value for the foundation area thus obtained, we may now ask what value of safety factor would have been required in the conventional design procedure to produce the same design area. This value may easily be determined by dividing the area so obtained by the area obtained by substituting the mean values for load and soil strength into Eq. 3. Thus, a safety factor is determined in terms of one dimensionless parameter, the cost ratio R , and four other dimensioned parameters, the means and standard deviations for the load and soil strength respectively. One logical dimensionless parameter for these variables is the coefficient of variation, which is defined as the ratio of the standard deviation to the mean. In fact, several trials have indicated that the safety factor, computed as indicated earlier, does depend only on the respective values of the coefficient of variation of these parameters and not on the means. Dividing by the deterministic value of area removes any dimensional dependence, as may be expected. Similarly, any dependence on the coefficient (6.6 in Eq. 3) is removed, and the computed safety factor is independent of foundation shape and embedment depth (with the possible reservation that some allowance should be made for the inability to determine accurately the soil unit weight associated with the latter).

By evaluating the safety factor for a range of values (expected to include those found in practice) for each of the independent parameters (cost ratio, R , load coefficient of variation, L , and soil strength coefficient of variation, C), a large number of observations may be obtained, and multiple regression techniques may be used to describe the observations by an empirical equation. For example, the following empirical relationship was obtained on the basis of 296 observations:

$$S. F. = 2.03 + 1.58L + 0.226e^{10C} - 0.28e^{-0.01R} - 0.147e^{10C-0.01R} \quad (11)$$

Once determined, all of the original independent variables can be substituted into the equation to compare the observed and computed values of safety factor. Of the 296 observations, four deviated by 0.2 to 0.23, 51 deviated by 0.1 to 0.2, and the remainder were within 0.1. For convenience in using the results of this analysis, a nomograph based on an equation considered to be a good representation of the data has been constructed and is shown in Figure 2.

To illustrate the independent influence of L , C , and R on safety factor, the typical curves shown in Figure 3 relate each of the variables in turn to safety factors while holding the other two constant. Both the load coefficient of variation, L , and the cost ratio, R , are shown to have only a small effect, the latter being more influential at lower values. However, the effect of the soil strength coefficient of variation, C , is considerable, particularly for values above 0.1.

DISCUSSION OF RESULTS

Although very appealing from many points of view, the foregoing analysis has some shortcomings. Review of Figure 1 will indicate that the significant zone of the area distribution diagram is in the tail of the diagram. This tail is highly dependent on the assumed tails of the input distribution functions, and, provided these assumptions are correct, any desired accuracy of the output function may be obtained, subject only to restrictions imposed by cost of computer time. Accordingly, the accuracy of the input functions is a major consideration. In this regard, Hooper and Butler (3) and Lumb (7) have shown that shear strength test values for cohesive soils closely approximate a normal distribution. Furthermore, provided that the number of samples is large enough, the distribution of the estimate of the mean strength of the population closely approximates a normal distribution, even if the distribution of the population departs from the normal to some extent, so long as it is approximately bell-shaped and not skewed (8). The assumption of normality for the estimate of mean shear strength, therefore, appears justified. In the case of the subjective assumptions of normal distributions for sample disturbance, progressive failure, and theory accuracy, no similar justification can be made. The selection of a normal distribution, as well as a standard deviation, is purely "engineering judgment." Furthermore, the shapes of the tails of these distributions have significance similar to that of strength.

It is emphasized that full consideration must be given to the geological aspects of site investigation when selecting the shear strength parameters. The foregoing development is based on the assumption of a random distribution of soil strength in the tested zone and a similar random distribution on the failure plane. Such an idealization will be frequently violated, and the proposed method in no way precludes the necessity for careful localized investigations where possible weak zones are suspected. A judicious increase in the soil strength coefficient of variation used to select safety factor may be advisable under certain conditions.

CONCLUSIONS

A probabilistic approach for determining in a rational manner the bearing capacity of a cohesive soil has been presented and illustrated. Despite the shortcomings that are inherent in the procedure at this stage of development, it is considered that this

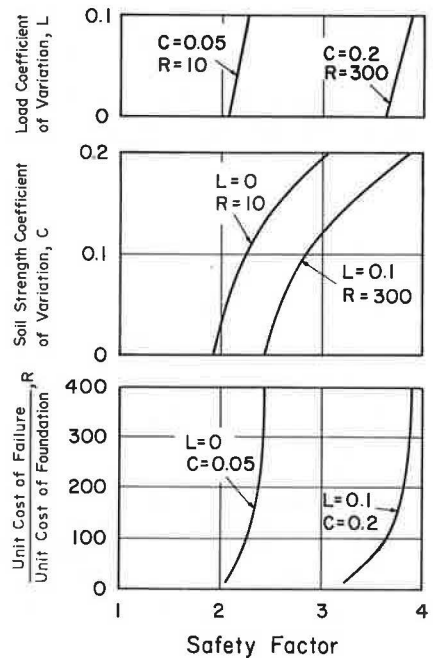


Figure 3. Influence of various parameters on safety factor.

method for the selection of a safety factor offers a number of advantages. Primarily, the design engineer, who is charged with the responsibility of selecting a safety factor, will be forced to consider the relevant parameters on which safety factor depends instead of exercising a gross intuitive judgment. In addition, some guidance is provided for determining the economic relevance of the various aspects of the bearing capacity problem.

REFERENCES

1. Skempton, A. W. The Bearing Capacity of Clays. Proceedings of the British Building Research Congress, Vol. 1, 1951, p. 180.
2. Wu, T. H., and Kraft, L. M. The Probability of Foundation Safety. Jour. Soil Mech. and Found. Div., ASCE, Vol. 93, No. SM5, 1967, p. 213.
3. Hooper, J. A., and Butler, F. G. Some Numerical Results Concerning the Shear Strength of London Clay. Geotechnique, Vol. 16, No. 4, 1966, p. 286.
4. Kay, J. N., and Krizek, R. J. Estimation of the Mean for Soil Properties. Proc. Conf. on Applications of Statistics and Probability to Soil and Structural Engineering, Hong Kong, Sept. 1971 (in press).
5. Terzaghi, K. Liner Plate Tunnels on the Chicago Subway. Trans. ASCE, Vol. 108, 1943, p. 970.
6. Warner, R. F., and Kabaila, A. P. Monte Carlo Study of Structural Safety. Jour. Structural Div., ASCE, Vol. 94, No. ST12, 1968, p. 2847.
7. Lumb, P. The Variability of Natural Soils. Canadian Geotechnical Jour., Vol. 3, No. 2, 1966, p. 74.
8. Miller, I., and Freund, J. E. Probability and Statistics for Engineers. Prentice-Hall, Englewood Cliffs, N.J., 1965.

CHART SOLUTIONS FOR ANALYSIS OF EARTH SLOPES

John H. Hunter, Department of Civil Engineering, Virginia Polytechnic Institute and State University; and

Robert L. Schuster, Department of Civil Engineering, University of Idaho

This paper compiles practical chart solutions for the slope stability problem and is concerned with the use of the solutions rather than with their derivations. Authors introduced are Taylor, Bishop and Morgenstern, Morgenstern, Spencer, Hunter, and Hunter and Schuster. Many of the solutions introduced appeared originally in publications not commonly used by highway engineers. In addition to the working assumptions and parameter definitions of each writer, the working charts are introduced, and example problems are included. The chart solutions cover a wide variety of conditions. They may be used to rapidly investigate preliminary designs and to obtain reasonable estimates of parameters for more detailed packaged computer solutions; in some cases, they may be used in the final design process.

•THE FIRST to make a valid slope stability analysis possible through use of simple charts and simple equations was Taylor (9). With the advent of high-speed electronic computers, other generalized solutions with different basic assumptions have been obtained and published. Unfortunately, these chart solutions have been published in several different sources, some of which are not commonly used by highway engineers in this country. This paper introduces several of these solutions that may prove useful and deals with how to use these solutions rather than with their derivations.

These chart solutions provide the engineer with a rapid means of determining the factor of safety during the early stages of a project when several alternative schemes are being investigated. In some cases they can be used in the final design procedure. Chart solutions such as these may very well serve as preliminary solutions for more detailed packaged computer software programs that are widely available (12).

Those chart solutions that appear to be most applicable to highway engineering problems involving stability of embankment slopes and cut slopes are presented here. In addition to introducing some solutions that may be unfamiliar, this compilation provides a quick means of locating various solutions so that rapid comparisons of advantages and disadvantages of each solution can be made.

The presentation of each solution includes pertinent references and contains sections on calculation techniques, working assumptions and definitions, limitations of the approach, and an example problem. In each case only a sufficient number of curves have been shown to indicate the scope of the charts and to illustrate the solutions. The reader should refer to the appropriate references for greater detail.

TAYLOR SOLUTION

The solution found by Taylor (9, 10) is based on the friction circle (ϕ circle) method of analysis and his resulting charts are based on total stresses. Taylor made the following assumptions for his solution:

1. A plane slope intersects horizontal planes at top and bottom. This is called a simple slope.

2. The charts assume a circular trace for the failure surface.

3. The soil is an unlayered homogeneous, isotropic material.

4. The shear strength follows Coulomb's Law so that $s = c + \tan \phi$.

5. The cohesion, c , is constant with depth as is shown in Figure 1(a).

6. Pore pressures are accounted for in the total stress assumption; therefore, seepage need not be considered.

7. If the cross section investigated holds for a running length of roughly two or more times the trace of the potential rupture surface, it is probable that this, a two-dimensional analysis, is valid.

8. The stability number in the charts is that used by Terzaghi and Peck (11) in presenting Taylor's solution. The stability number, N , is $\gamma H_C/c$.

9. The depth factor, D , as shown in Figure 2, is the depth to a firm stratum divided by the height of the slope.

The following limitations should be observed in using Taylor's solution:

1. It is not applicable to cohesionless soils.
2. It may not be applied to the partial submergence case.
3. Tension cracks are ignored.
4. According to Taylor, his analysis does not apply to stiff, fissured clays.

The charts presented by Terzaghi and Peck for Taylor's solution consist of the following:

1. A chart for soils with $\phi = 0$ deg with depth factors, D , varying from 1.0 to ∞ and slope angles, β , varying from 0 to 90 deg (Fig. 3),
2. A chart for materials having cohesion and friction with ϕ varying from 0 to 25 deg and β varying from 0 to 90 deg (Fig. 4), and
3. A chart for locating the critical circle of a slope failure (not presented in this paper).

Examples of use of Taylor's solution follow:

1. A cut is to be excavated in soft clay to a depth of 30 ft. The soil has a unit weight of 115 pcf and a cohesion of 550 psf. A hard layer underlies the soft layer at a depth of 40 ft below the original ground surface. What is the slope angle, if any, at which failure is likely to occur?

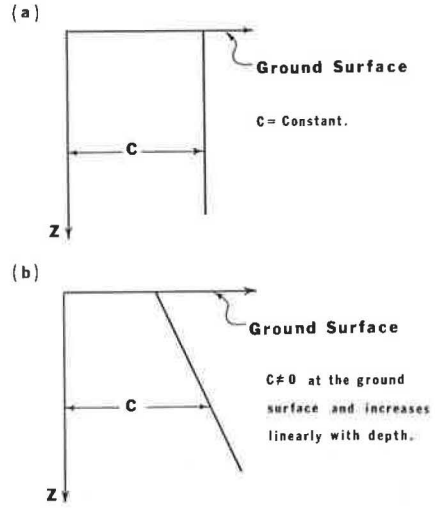


Figure 1. Comparison of assumptions for cohesion, c , as made by various investigators.

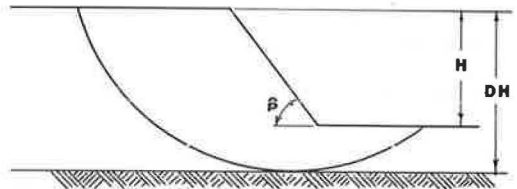


Figure 2. Elements of a simple slope.

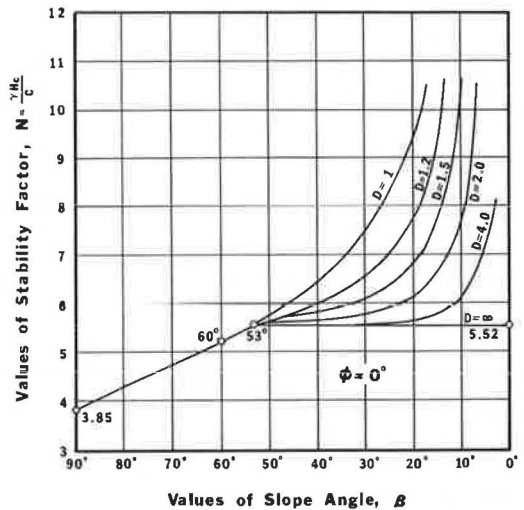


Figure 3. Relations between slope angle, β , and stability number, N , for different values of depth factor, D [after Terzaghi and Peck (11)].

Solution: Because the soil is a soft clay, ϕ is assumed to be zero and the chart of Figure 3 is applicable:

$$D = 40/30 = 1.33$$

If failure is to occur, the critical height, H_c , is 30 ft:

$$N = (\gamma H_c)/c = (115)(30)/550 = 6.28$$

From Figure 3, for $D = 1.33$ and $N = 6.28$, β may be read as 30 deg, which is the unknown that was to have been determined.

2. A cut is to be excavated in a material that has a cohesion of 250 psf, a unit weight of 115 pcf, and an angle of shearing resistance of 10 deg. The design calls for a slope angle of 60 deg. What is the maximum depth of cut that can be made and still maintain a factor of safety of 1.5 with respect to the height of the slope?

Solution: Because the soil has both cohesion and angle of shearing resistance, the chart of Figure 4 is applicable. The factor of safety (with respect to height) of 1.5 is the critical height, H_c , divided by the actual height, H . The depth factor, D , does not enter into the solution if the soil is a c, ϕ type of soil.

From Figure 4, for $\phi = 10$ deg and $\beta = 60$ deg, N may be read as 7.25. From the definition of stability number,

$$N = (\gamma)(H_c)/c$$

$$\text{or } H_c = (c)(N)/\gamma = (250)(7.25)/115 = 15.75 \text{ ft}$$

$$H = H_c/1.5 = 15.75/1.5 = 10.5 \text{ ft}$$

Thus, it would be possible to make a 60-deg cut at any depth up to 10.5 ft and still maintain a factor of safety that is equal to or greater than 1.5.

BISHOP AND MORGENSTERN SOLUTION

Bishop's adaptation of the Swedish slice method (1) was used by Bishop and Morgenstern (2) for their solution. Their charts are based on effective stresses rather than total stresses. Consequently, it is necessary to take pore pressures into consideration.

Bishop and Morgenstern made the following assumptions:

1. The geometry of the slope is simple, as was the case for Taylor's solution. The potential sliding surface is assumed to be cylindrical; the trace of the sliding surface is assumed to be a portion of a circle.

2. The pore pressure is accounted for by use of the pore pressure ratio, r_u . This ratio is defined as being equal to $u/(\gamma h)$, where h = depth of point in soil mass below the soil surface, γ = unit weight of the soil (bulk density), and u = pore pressure of water in the soil. The pore pressure ratio is assumed to be constant throughout the cross section; this is called a homogeneous pore pressure distribution. If there are minor variations in r_u throughout the cross section, an average value of r_u can be used.

3. For steady-state seepage, use a weighted average of r_u over the section.

4. The factor of safety, FS, is defined as $m - (n)(r_u)$, where m and n are determined by using charts in Figures 5 through 7.

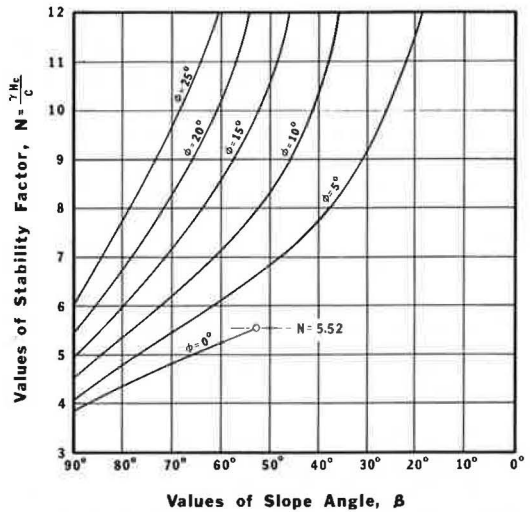


Figure 4. Relations between slope angle, β , and stability number, N , for materials having cohesion and friction, for various values of ϕ [after Terzaghi and Peck (1)].

5. Depth factors, D , of 1.0, 1.25, and 1.5 are used in this solution where the depth factor is defined as Taylor defined it: The depth to a hard stratum is the depth factor multiplied by the embankment height.

6. The solution implies that the cohesion is constant with depth as shown in Figure 1(a). An interesting feature of this solution is that pore pressures can be changed to see what effect this will have on the stability of the slope.

Bishop and Morgenstern's solution has the following limitations:

1. There is no provision for intermediate water table levels.
2. The averaging technique for pore pressure ratio tends to give an overestimation of the factor of safety. In an extreme case, this overestimation will be on the order of 7 percent.

In using this chart solution it is convenient to select the critical depth factor by use of the lines of equal pore pressure

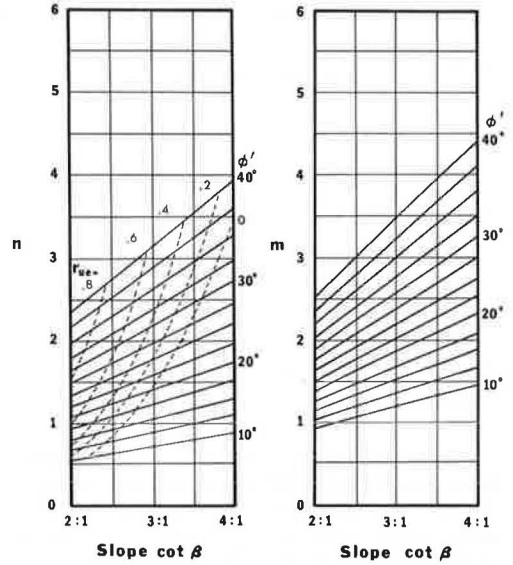


Figure 5. Stability coefficients, m and n , for $\frac{c'}{\gamma H} = 0.05$ and $D = 1.00$ [after Bishop and Morgenstern (2)].

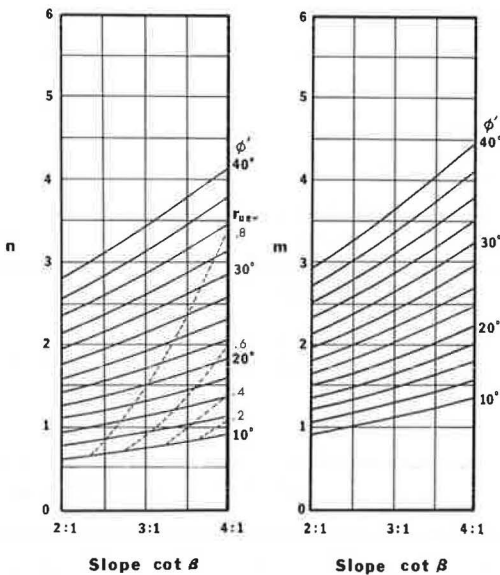


Figure 6. Stability coefficients, m and n , for $\frac{c'}{\gamma H} = 0.05$ and $D = 1.25$ [after Bishop and Morgenstern (2)].

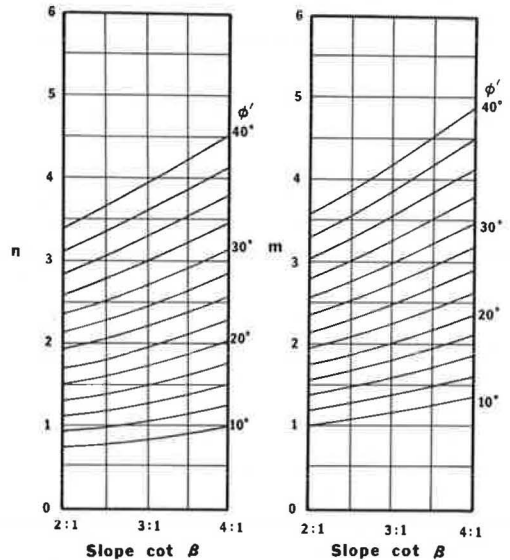


Figure 7. Stability coefficients, m and n , for $\frac{c'}{\gamma H} = 0.05$ and $D = 1.50$ [after Bishop and Morgenstern (2)].

ratio, r_{ue} , on the charts of Figures 5 and 6. The ratio, r_{ue} , is defined as $(m_2 - m_1)/(n_2 - n_1)$ where n_2 and m_2 are values for a higher depth factor, D_2 , and n_1 and m_1 correspond to a lower value of the depth factor, D_1 .

If the design value of pore pressure ratio is higher than r_{ue} for the given section and strength parameters, then the factor of safety determined with the higher depth factor, D_2 , has a lower value than the factor of safety determined with the lower depth factor, D_1 . This is useful to know when no hard stratum exists or when checking to see if a more critical circle exists not in contact with a hard stratum. The example problem will clarify this concept.

To determine the minimum factor of safety for sections not located directly on a hard stratum, enter the appropriate chart for the given $c'/(\gamma H)$ and, initially, for $D = 1.00$. Note that c' is the effective stress value of cohesion and H is the height of the slope while γ is the unit weight of the soil. The values of β and ϕ' define a point on the curves of n with which is associated a value of r_{ue} given by the dashed lines. If that value is less than the design value of r_u , the next depth factor, $D = 1.25$, will yield a more critical value of the factor of safety. If, from the chart for $D = 1.25$, the values are checked and r_{ue} is still less than the design value for r_u , move to the chart for $D = 1.50$ with the same value of $c'/(\gamma H)$.

Bishop and Morgenstern (2) show charts for values of $c'/(\gamma H)$ of 0.00, 0.025, and 0.05 with depth factor, D , values of 1.00, 1.25, and 1.50. Only enough charts are shown here to illustrate the solution.

An example of Bishop and Morgenstern's solution follows:

A slope is cut so that the cotangent of the slope angle, β , is 4.0. The cut is 140 ft deep. A hard stratum exists at a depth of 60 ft below the bottom of the cut. The soil has an effective angle of shearing resistance, ϕ' , of 30 deg. The effective cohesion, c' , is 770 psf. The unit weight is 110 pcf, and it is estimated that the pore pressure ratio, r_u , is 0.50 for the slope.

From the given conditions, $c'/(\gamma H) = 770/(110)(140) = 0.050$. From Figure 5, for $D = 1.00$ with $c'/(\gamma H) = 0.050$, $\phi' = 30$ deg, and $\cot \beta = 4.0$, it is seen that $r_{ue} < 0.5$. Therefore, $D = 1.25$ is the more critical value for depth factor. Using Figure 6, with the same value of $c'/(\gamma H)$ and with $D = 1.25$, it is found that $r_{ue} > 0.5$. In this case the maximum value that D could have is $(140 + 60)/140 = 1.43$. Therefore, within the limitations of the charts, $D = 1.25$ is the critical depth factor. From Figure 6 it is seen that $m = 3.22$ and $n = 2.82$ for the given values of $c'/(\gamma H)$, ϕ' , and $\cot \beta$. Accordingly, the following factor of safety is obtained:

$$FS = m - (n)(r_u) = 3.22 - 2.82(0.50) = 1.81$$

The chart for $D = 1.50$ for $c'/(\gamma H) = 0.050$ (Fig. 7) is not necessary for the solution to this example problem, but it is given to indicate the range in this particular sequence of charts.

MORGENSTERN SOLUTION

Morgenstern (6) used Bishop's adaptation of the Swedish slice method of analysis (1) to develop a solution to the slope stability problem that is somewhat different from the one he developed with Bishop. His solution is, again, based on effective stresses rather than total stresses. His solution is primarily for earth dams, but there are highway cuts and fills that nearly fulfill his assumptions. Morgenstern made the following assumptions:

1. The slope is a simple slope of homogeneous material resting on a rigid impermeable layer at the toe of the slope.
2. The soil composing the slope has effective stress parameters c' (cohesion) and ϕ' (angle of shearing resistance), both of which remain constant with depth.
3. The slope is completely flooded prior to drawdown; a full submergence condition exists.

4. The pore pressure ratio $\bar{\beta}$, which is $\Delta u/\Delta \alpha_1$, is assumed to be unity during drawdown, and no dissipation of pore pressure occurs during drawdown.

5. The unit weight of the soil (bulk density), γ , is assumed to be constant at twice the unit weight of water of 124.8 pcf.

6. The pore pressure can be approximated by the product of the height of soil above a given point and the unit weight of water.

7. The drawdown ratio is defined as L/H where L is the amount of drawdown and H is the original height of the slope.

8. To be consistent, all assumed potential sliding circles must be tangent to the base of the section. This means that the value of H in the stability number, $c'/(\gamma H)$, and in L/H must be adjusted for intermediate levels of tangency (see the example problem for clarification).

Morgenstern's solution is particularly good for small dams and consequently might be particularly applicable where a highway embankment is used as an earth dam or for flooding that might occur behind a highway fill. Another important attribute of the method is that it permits partial drawdown conditions.

This method is somewhat limited by its strong orientation toward earth dams. If a core exists, it is noted that this violates the assumption of a homogeneous material. Another limitation is the assumption that the unit weight is fixed at 124.8 pcf. Attention is also called to the assumption of an impermeable base.

Morgenstern's charts cover a range of stability numbers, $c'/(\gamma H)$, from 0.0125 to 0.050 and slopes of 2:1 to 5:1. The maximum value of ϕ' shown on his charts is 40 deg. Following are some example problems using Morgenstern's method:

1. An embankment has a height, H , of 100 ft. It is composed of a soil with an effective cohesion, c' , of 312 psf and an effective angle of shearing resistance, ϕ' , of 30 deg. The unit weight of the soil must be assumed to be equal to 124.8 pcf. The embankment is to have a slope so that the cotangent of the slope angle is 3.0. What is the minimum factor of safety for the complete drawdown condition?

Solution: The stability number, $c'/(\gamma H) = 312/[(124.8)(100)] = 0.025$. With this value and with $\cot \beta = 3.0$, $\phi' = 30$ deg, and the drawdown ratio $L/H = 1.0$, the factor of safety is directly obtainable from Figure 9 as $FS = 1.20$. By examining the charts in Figures 8 through 10, it can be seen that the critical circle is tangent to the base of the slope;

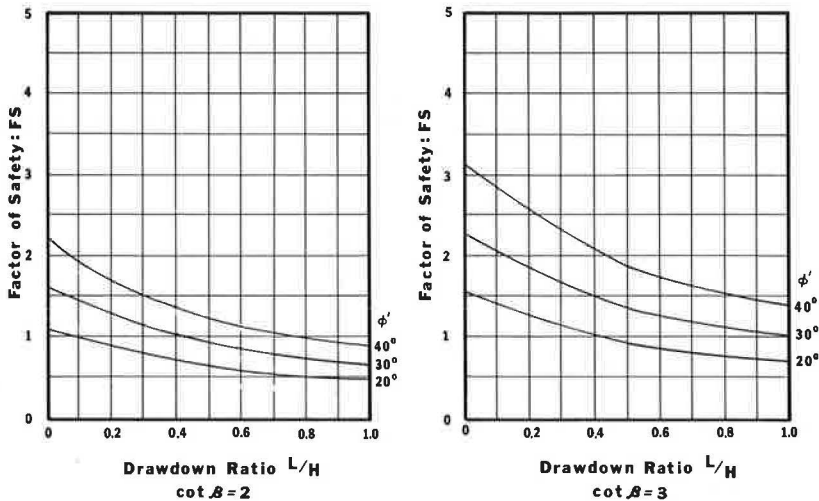


Figure 8. Relationship between factor of safety, FS , and drawdown ratio, L/H , for

$$\frac{c'}{\gamma H} = 0.0125 \text{ [after Morgenstern (6)]}.$$

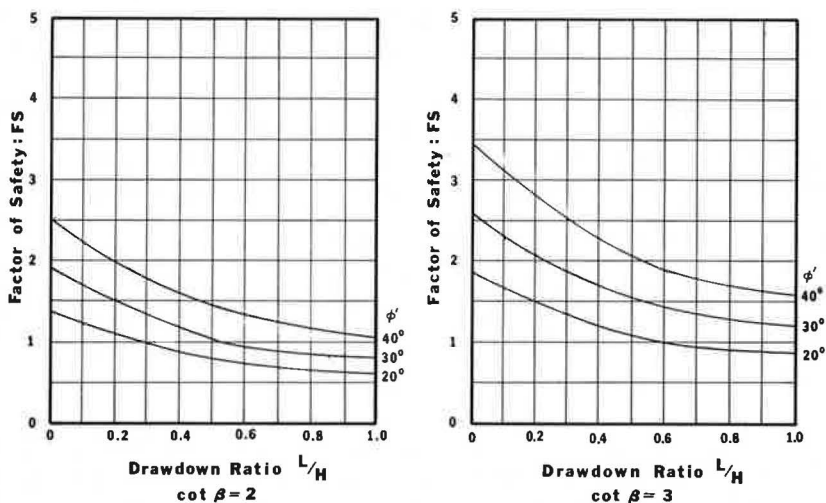


Figure 9. Relationship between factor of safety, FS, and drawdown ratio, L/H , for $\frac{c'}{\gamma H} = 0.025$ [after Morgenstern (6)].

if any other tangency is assumed, H would have to be reduced. If H is reduced, then the stability number is increased and this will, in all cases, result in a higher factor of safety.

2. It is now required to find the minimum factor of safety for a drawdown to mid-height of the section in the prior example.

Solution a: Considering slip circles tangential to the base of the slope, the effective height of the section, H_e , is equal to its actual height and the stability number remains

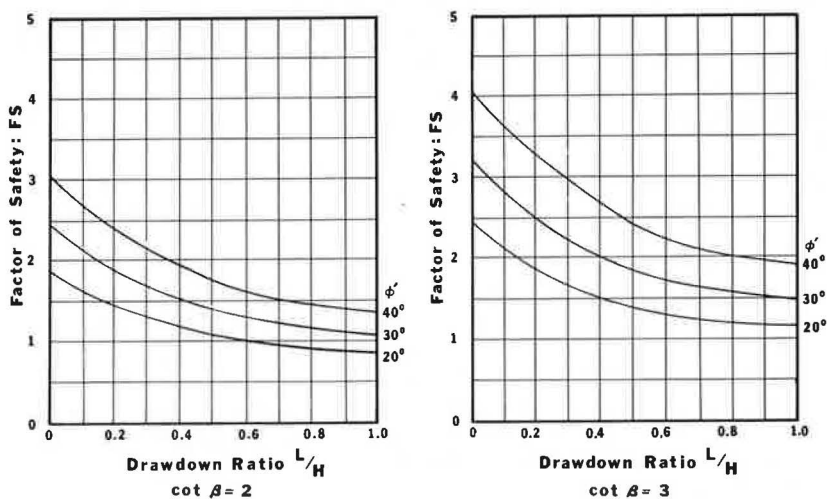


Figure 10. Relationship between factor of safety, FS, and drawdown ratio, L/H , for $\frac{c'}{\gamma H} = 0.050$ [after Morgenstern (6)].

unchanged as 0.024. With this value of stability number and $L/H_e = 0.50$, and with other conditions remaining the same, the factor of safety may be read from Figure 9 as $FS = 1.52$.

Solution b: Considering slip circles tangential to mid-height of the slope, the effective height is equal to one-half the actual height so that $H_e = H/2 = 100/2 = 50$ ft. Thus $c'/(\gamma H_e)$ is twice that of the previous solution or 0.05, and $L/H_e = 1.00$. The minimum factor of safety, as determined by Morgenstern's solution, can be read directly from Figure 10 as $FS = 1.48$.

Solution c: Considering slip circles tangential to a level $H/4$ above the base of the slope, H_e becomes $3H/4 = 75$ ft. Thus the stability number $c'/(\gamma H_e) = 0.033$, and $L/H_e = 0.67$. The minimum factor of safety for this family must be obtained by interpolation. From Figure 9 with $c'/(\gamma H_e) = 0.025$, the factor of safety is 1.31, and from Figure 10 with $c'/(\gamma H_e) = 0.05$, the factor of safety is 1.61. Interpolating linearly for $c'/(\gamma H_e) = 0.033$, the minimum factor of safety for this family is $1.31 + 0.30/3 = 1.41$.

These examples demonstrate that for partial drawdown the critical circle may often lie above the base of the slope, and it is important to investigate several levels of tangency for the maximum drawdown level. In the case of complete drawdown, the minimum factor of safety is always associated with circles tangent to the base of the slope and the factor of safety at intermediate levels of drawdown need not be investigated. This may not be the case if the pore pressure distribution during drawdown differs significantly from that assumed by Morgenstern.

SPENCER SOLUTION

Bishop's adaptation of the Swedish slice method has been used by Spencer (8) to find a generalized solution to the slope stability problem. Spencer assumed parallel interslice forces. His solution is based on effective stresses. Spencer defines the factor of safety, FS , as the quotient of shear strength available divided by the shear strength mobilized.

Spencer made the following additional assumptions and definitions for his solution:

1. The soils in the cut or embankment and underneath the slope are uniform and have similar properties.
2. The slope is simple and the potential slip surface is circular in profile.
3. A hard or firm stratum is at a great depth, or the depth factor, D , is very large.
4. The effects of tension cracks, if any, are ignored.
5. A homogeneous pore pressure distribution is assumed with the pore pressure coefficient, r_u , equal to $u/(\gamma h)$, where u = mean pore water pressure on base of slice, γ = unit weight of the soil (bulk density), and h = mean height of a slice.
6. The stability number N is defined as $c'/[(FS)\gamma H]$.
7. The mobilized angle of shearing resistance, ϕ'_m , is the angle whose tangent is $(\tan \phi')/FS$.

Spencer's method does not prohibit the slip surface from extending below the toe. His solution permits the safe slope for an embankment of a given height to be found rapidly.

Although the limitations of Spencer's method are few, it is noted that a simple trial and error solution is required to find the factor of safety with the slope and soil properties known. In addition, it is difficult to use his method for intermediate levels of the water table. Spencer provides charts for a range of stability number, N , from 0.00 to 0.12 with mobilized angle of shearing resistance varying from 10 to 40 deg and slope angles up to 34 deg. Charts are provided for pore pressure ratio, r_u , with values of 0.0, 0.025, and 0.50. Only one of these charts (Fig. 11) is shown for use in the example problem. Spencer furnishes charts for locating the critical surface.

An example of Spencer's solution follows:

An embankment is to be formed with a factor of safety of 1.5 and a height of 100 ft. The soil has an effective cohesion of 870 psf and an effective angle of shearing resistance of 26 deg. The unit weight of the soil is 120 pcf and the pore pressure ratio is 0.50. Find the slope that corresponds to this factor of safety.

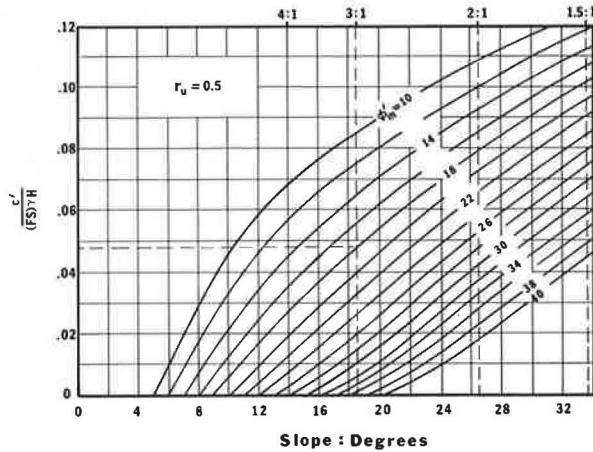


Figure 11. Relationship between stability number $\left[\frac{c'}{(FS) \gamma H} \right]$ and slope angle, β , for various values of ϕ'_m [after Spencer (8)].

Solution: The stability number,

$$N = c' / [(FS) \gamma H] = 870 / [(1.5)(120)(100)] = 0.048$$

$$\tan \phi'_m = (\tan \phi') / FS = \tan 26 \text{ deg} / 1.5 = 0.488 / 1.5$$

$$\tan \phi'_m = 0.325 \text{ or } \phi'_m = 18 \text{ deg}$$

Referring to Figure 11 for $r_u = 0.50$, the slope corresponding to a stability number of 0.48 and $\phi'_m = 18 \text{ deg}$ is $\beta = 18.4 \text{ deg}$. This corresponds approximately to a slope of 3:1.

Linear interpolation between charts for slopes for r_u values falling between the chart values is probably sufficiently accurate.

HUNTER SOLUTION

In 1968, Hunter (3) approached the slope stability problem with two assumptions that are different from the solutions previously presented in this paper. He assumed that the trace of the potential slip surface is a logarithmic spiral and the cohesion varies with depth. His charts are based on total stresses. Hunter's working assumptions and definitions follow:

1. The section of a cut is simple with constant slope, and top and bottom surfaces are horizontal.
2. The soil is saturated to the surface through capillarity.
3. The soil is normally consolidated, unfissured clay.
4. The problem is two-dimensional.
5. The shear strength can be described as $s = c + p \tan \phi$ where c varies linearly with depth, as is shown in Figure 1(b). It is assumed that the ratio c/p' is a constant, where p' is the effective vertical stress. Note that p' increases with depth.
6. If $\phi > 0 \text{ deg}$, the potential slip surface is a logarithmic spiral. If $\phi = 0 \text{ deg}$, the potential failure surface is a circle because the logarithmic spiral degenerates into a circle for this case.

7. The effective stresses immediately after excavation are the same as those before excavation. This describes the end-of-construction case.

8. The water table ratio, M , is defined as $(h/H)(\gamma_w/\gamma')$, where h = depth from top of slope to the water table during consolidation, H = height of cut, γ_w = unit weight of water, and γ' = submerged or buoyant unit weight of soil.

9. While c increases linearly with depth, the angle of shearing resistance, ϕ , is constant with depth.

10. A stability number, N , is obtained so that the factor of safety,

$$FS = \frac{c}{\gamma z_1 N}$$

where

$$z_1 = z + h \left(\frac{\gamma_w}{\gamma'} \right)$$

and z = depth below the original ground surface of cut to point where cohesion, c , is determined.

An equivalent and perhaps more convenient relationship is

$$FS = \left(\frac{c}{p'} \right) \left(\frac{\gamma'}{\gamma} \right) N$$

because often (c/p') can be estimated from Skempton's (7) formula,

$$\left(\frac{c}{p'} \right) = 0.11 + 0.0037(PI)$$

where PI = plasticity index of the soil in percent.

11. The depth ratio, D , is defined the same as in the description of Taylor's work. If $\phi > 0$ deg, the effects of a firm layer at any depth are negligible. If $\phi = 0$ deg, the depth factor can have a significant but small influence on the factor of safety, as is shown in Hunter's (3) work and also by Hunter and Schuster (4). Only when the stability number, N , is greater than about 25 and the slope angle, β , is less than about 15 deg is the small reduction in N important enough to be taken into account.

Hunter's solution permits realistic variation in the values of cohesion, c , for normally consolidated soils. It can easily handle the situation for the water table at any of a wide range of elevations. This solution should be used only for normally consolidated materials.

Numerous charts are furnished by Hunter. The charts show the slope angle, β , varying from 5 to 90 deg, and the angle of shearing resistance ϕ varying from 0 to 35 deg in steps of 5 deg. The water table ratio, M , is varied from 0.00 to 2.00 in steps of 0.25. In addition, many tables and graphs are shown that are useful in locating the critical failure surface. In this paper only one chart (Fig. 12) is shown to illustrate Hunter's solution. An example of Hunter's solution follows:

A 25-ft slope of 30 deg is to be cut in normally consolidated material with a unit weight of 112 pcf and the water table at a depth of 10 ft. The material has been tested (on a total stress basis) and found to have a ϕ of 10 deg with a plasticity index of 25 percent. It is required to estimate the factor of safety of this slope.

Solution: Using Skempton's relationship,

$$c/p' = 0.11 + 0.0037(PI) = 0.11 + 0.0037(25) = 0.2025$$

$$M = \left(\frac{h}{H} \right) \left(\frac{\gamma_w}{\gamma'} \right) = \left(\frac{10}{25} \right) \left(\frac{62.4}{112 - 62.4} \right) = \left(\frac{10}{25} \right) (1.26) = 0.502$$

Using $M = 0.50$, $\beta = 30$ deg, and $\phi = 10$ deg, find the stability number from the chart in Figure 12. Read $N = 17.1$. Thus, the factor of safety,

$$FS = \left(\frac{c}{p'}\right) \left(\frac{\gamma'}{\gamma}\right) N$$

$$FS = (0.2025) \left(\frac{49.6}{112}\right) (17.1) = 1.52$$

HUNTER AND SCHUSTER SOLUTION

Based on some of Hunter's original work (3), Hunter and Schuster (4) published a solution for the special case of $\phi = 0$ deg in normally consolidated clays. This solution is a total stress solution.

The assumptions are the same as those made by Hunter in the previous section, except that the potential sliding surface is a circular arc rather than a logarithmic spiral. In particular, this solution permits the cohesion, c , to increase linearly with depth, and the saturated soil may have a water table that can be anywhere within a wide range. The depth factor, D , is taken into account. The method ignores tension cracks.

The charts furnished by Hunter and Schuster show the water table ratio varying from 0.00 to 2.00 in steps of 0.25, and the depth ratio, D , varying from 0 to 4. Only those charts (Figs. 13 and 14) necessary to illustrate the example problem are shown. Some example problems using Hunter and Schuster's solution follow:

1. A cut 15 ft deep is to be made in a normally consolidated clay with a slope angle of 30 deg. The water table is 5 ft below the original ground surface. The soil weighs 104 pcf, and the c/p' ratio is 0.24 for the soil. What is the factor of safety for this cut?

Solution: The water table ratio M is

$$M = \left(\frac{h}{H}\right) \left(\frac{\gamma_w}{\gamma'}\right) = \left(\frac{5}{15}\right) \left(\frac{62.4}{41.6}\right) = 0.50$$

In Figure 13, with $M = 0.50$ and $\beta = 30$ deg, $N = 8.9$ (a possible shallow failure). Calculate the factor of safety, FS , as

$$FS = \left(\frac{c}{p'}\right) \left(\frac{\gamma'}{\gamma}\right) N = (0.24) \left(\frac{41.6}{104}\right) (8.9) = 0.855 < 1.00$$

It can therefore be concluded that this cut is impossible without failure occurring.

2. A cut at a slope angle of 10 deg is to be made 15 ft deep in a normally consolidated clay with the water table 15 ft from the surface. Underneath the clay at a depth of 30 ft is a harder, stronger stratum. When tested, the soil showed $\phi = 0$ deg on a total stress basis. The ratio c/p' for this soil is 0.24, and its unit weight is 104 pcf. Find the factor of safety for this proposed cut.

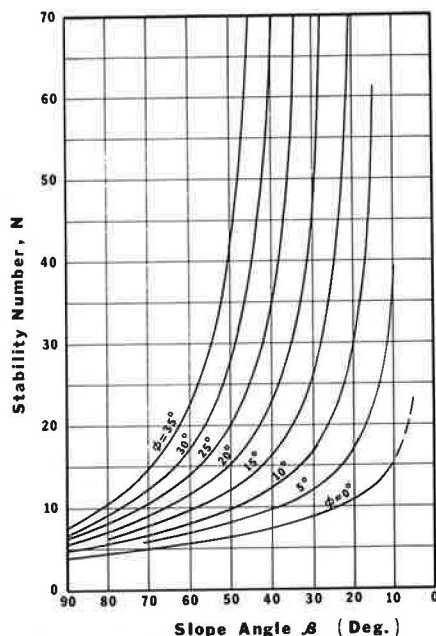


Figure 12. Relationship between slope angle and stability number, N , for $M = 0.50$ and unlimited depth of soil, for various values of ϕ . Solid lines indicate shallow surfaces and dashed lines indicate deep surfaces [from Hunter (3)].

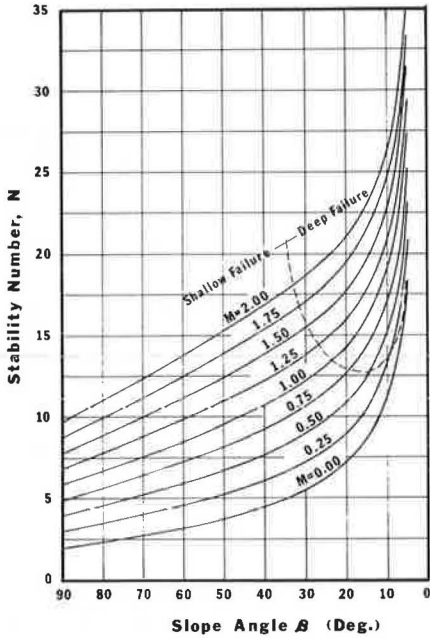


Figure 13. Relationship between slope angle, β , and stability number, N , for $\phi = 0$ and unlimited depth of clay [from Hunter and Schuster (4)].

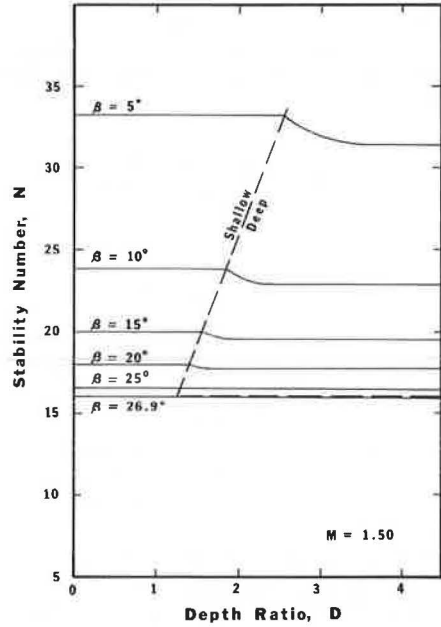


Figure 14. Relationship between depth factor, D , and stability number, N , for $\phi = 0$ for selected values of slope inclination [from Hunter and Schuster (4)].

Solution:

$$M = \left(\frac{h}{H}\right) \left(\frac{\gamma_w}{\gamma'}\right) = \left(\frac{15}{15}\right) \left(\frac{62.4}{41.6}\right) = 1.50$$

From Figure 13, with $\beta = 10$ deg and $M = 1.50$, the value of N plots up in the deep failure zone with a value of approximately 23.9. Because it is in the deep failure zone, $D = 30/15 = 2.0$ may be important.

From Figure 14, for $M = 1.50$, $D = 2.0$, and $\beta = 10$ deg, it is seen that N reduces slightly to 23.2. Thus, the factor of safety is

$$FS = \left(\frac{c}{p'}\right) \left(\frac{\gamma'}{\gamma}\right) N = (0.24) \left(\frac{41.6}{104}\right) (23.2) = 2.23$$

Note that the depth factor, in general, has only a negligible or quite small effect on the factor of safety.

One set of generalized solutions that should be mentioned is that developed by Janbu (5). His solutions are extensive and do not lend themselves to simple presentations as has been the case with the other solutions. Janbu's solutions are useful in analyzing the influence of drawdown conditions and the effect of water-filled tension cracks and surcharge. Janbu implies that both the cohesion, c , and the angle of shearing resistance, ϕ , are constant with depth. Although not reviewed here, Janbu's solutions are recommended to the engineer who frequently deals with stability analyses of slopes.

SUMMARY

The chart solutions developed by Taylor, Bishop and Morgenstern, Morgenstern, Spencer, Hunter, and Hunter and Schuster can be applied to a number of types of slope stability analyses. Some of the methods presented were originally developed only for cuts; some were developed especially for embankments or fills such as earth dams. Each solution presented, however, is applicable to some highway engineering situation. References have been given indicating more complex chart solutions not illustrated here, and an entry into the literature on computerized solutions has been given. Of the solutions introduced, those of Taylor, Hunter, and Hunter and Schuster are best suited to the short-term (end-of-construction) cases where pore pressures are not known and total stress parameters apply. The other methods are intended for use in long-term stability (steady seepage) cases with known effective stress parameters.

The methods make similar assumptions regarding slope geometry, two-dimensional failure, and the angle of shearing resistance being constant with depth. However, they vary considerably in assumptions regarding variation of cohesion, c , with depth, position of the water table, base conditions, drawdown conditions, and shape of the failure surface. Altogether, a wide range of conditions can be approximated by these available generalized solutions.

Each author has attempted to reduce the calculation time required to solve stability problems. The chart solutions alone may be sufficient for many highway problems; in other cases, chart solutions may save expensive computer time by providing a reasonable estimate as a starting point for computer programs that solve slope stability problems.

REFERENCES

1. Bishop, A. W. The Use of the Slip Circle in the Stability Analysis of Slopes. *Geotechnique*, Vol. 5, No. 1, 1955, pp. 7-17.
2. Bishop, A. W., and Morgenstern, N. Stability Coefficients for Earth Slopes. *Geotechnique*, Vol. 10, No. 4, 1960, pp. 129-150.
3. Hunter, J. H. Stability of Simple Cuts in Normally Consolidated Clays. PhD thesis, Dept. of Civil Engineering, Univ. of Colorado, Boulder, 1968.
4. Hunter, J. H., and Schuster, R. L. Stability of Simple Cuttings in Normally Consolidated Clays. *Geotechnique*, Vol. 18, No. 3, 1968, pp. 372-378.
5. Janbu, N. Stability Analysis of Slopes With Dimensionless Parameters. Harvard Soil Mechanics Series, No. 46, 1954, 81 pp.
6. Morgenstern, N. Stability Charts for Earth Slopes During Rapid Drawdown. *Geotechnique*, Vol. 13, No. 2, 1963, pp. 121-131.
7. Skempton, A. W. Discussion of "The Planning and Design of the New Hong Kong Airport." *Proc. Institution of Civil Engineers*, Vol. 7, 1957, pp. 305-307.
8. Spencer, E. A Method of Analysis of the Stability of Embankments Assuming Parallel Inter-Slice Forces. *Geotechnique*, Vol. 17, No. 1, 1967, pp. 11-26.
9. Taylor, D. W. Stability of Earth Slopes. *Jour. Boston Soc. of Civil Engineers*, Vol. 24, 1937, pp. 197-246.
10. Taylor, D. W. *Fundamentals of Soil Mechanics*. John Wiley and Sons, Inc., New York, 1948, pp. 406-476.
11. Terzaghi, K., and Peck, R. B. *Soil Mechanics in Engineering Practice*. John Wiley and Sons, Inc., New York, 1967, pp. 232-254.
12. Whitman, R. V., and Bailey, W. A. Use of Computers for Slope Stability Analysis. *Jour. Soil Mech. and Found. Div., ASCE*, Vol. 93, No. SM4, Proc. Paper 5327, July 1967, pp. 475-498; also in ASCE "Stability and Performance of Slopes and Embankments," 1969, pp. 519-548.

SPECIAL TESTS FOR DESIGN OF HIGH EARTH EMBANKMENTS ON US-101

Earl B. Hall, Geo-Testing, Inc., San Rafael, California; and
Travis Smith, Materials and Research Department, California Division of Highways

New highway routes through the mountains of California will necessitate the construction of several embankments approaching 400 ft in height. The testing for use in design of high embankments involving soil-rock mixtures cannot be accommodated in conventional triaxial equipment. In an attempt to simulate embankment stress conditions on materials that were of the same types and sizes as contemplated for the prototype, large-scale triaxial tests were conducted on 12-in. diameter by 28-in. high specimens of minus 3-in. material at confining pressures up to 125 psi. Higher confining pressures to 400 psi were also used but these specimens were approximately 6 in. in diameter by 14 in. high, and the maximum particle size was $1\frac{1}{2}$ in. Tests were conducted to obtain both total and effective stresses. Degradation of the materials under compaction, consolidation, and shearing was determined. The test data acquired have been used in design of one of the embankments with an overall height of 383 ft. The construction of this embankment was begun in June 1966 and was scheduled for completion in September 1968.

•DURING the next few years it will be necessary to relocate many miles of US-101 in northern California. This route is slightly inland from the Pacific Ocean and follows along Rattlesnake Creek and the Eel River. The terrain is very steep and much of the existing road is a two-lane road with rather sharp curves and low design speeds. The new route will be a four-lane highway with design speeds of the order of 60 mph.

To achieve these design standards, it will be necessary to construct at least one embankment that will be considerably higher than has been used in the construction of California highways. At least three creek crossings will have embankments in excess of 250 ft high. As an alternative it would be possible to build structures at these locations, but the cost of the structures would be considerably greater than the cost of embankments. Because of the proximity of the new road to Rattlesnake Creek and to the Eel River, it will be necessary to use slopes no flatter than 2:1 (2 horizontal to 1 vertical) and preferably as steep as $1\frac{1}{2}$:1 in order to avoid encroachment of the toe of the embankment into the nearby creek or river.

It was deemed necessary that studies should be made of the strength characteristics of the embankment material. Normally, highway embankments in California have been constructed of roadway excavation with $1\frac{1}{2}$:1 or 2:1 slopes and heights as great as 100 to 200 ft. It was decided to undertake a rather comprehensive testing program using typical materials that would be available from roadway excavation along the projects to be constructed.

SAMPLES

The materials in this area are derived from the large belt of sedimentary rocks of Upper Jurassic to Cretaceous age. The sedimentary rocks consist chiefly of coarse sandstones, shales, and minor conglomerates. A negligible amount of volcanic rocks

is interbedded with sandstone and shale at a few places along the proposed alignment. Basalt, greenstone, chert, and limestone are also present in minor quantities.

Three sites were selected for securing samples believed to be representative of the material that would be encountered in construction. A sample of material was secured from each of these sites and consisted of approximately 3 cu yd of material per site. The material was excavated with a small shovel or loader and transported from the sites to the laboratory in Sausalito, a distance of approximately 185 miles. In normal operations the material from these roadway cuts will be excavated by the use of loaders or rippers, with occasional blasting necessary in the zones of harder sandstone.

One of the samples, probably the one of the poorest quality, was primarily shale in a slightly weathered condition. The second sample consisted of somewhat weathered fractured sandstone with some shale. The third sample was primarily a combination of sandstone and shale with somewhat more severe weathering than was involved in the other two samples. The testing reported here involves only the third material. A fourth type of material will be available from roadway cuts in limited quantities. This material will consist of fairly fresh to weathered massive fractured sandstone. It was not felt that it was necessary to test this sandstone because its strength will be considerably higher than any of the three samples tested.

Four assumptions were made in formulating the testing program. First, it was assumed that the samples secured would be representative of the material that would be encountered in roadway excavation. Second, the materials would be handled in such a manner as to ensure a proper moisture placement range. Third, some selection of material would be possible, and hence the material could be zoned using the poorer quality in the areas where strength was not so critical and using the better quality where the higher strength was essential. Fourth, detrimental excess hydrostatic pressures would not develop if the material was placed somewhat dry of optimum.

TESTS

The principal parameters that were desired from the testing program performed by the U. S. Army Engineers Division Laboratory at Sausalito, California, were shear strengths obtained under varying molding moisture-density conditions. Further, these values were needed on materials containing appreciable quantities of large gravel sizes and under test conditions of high confining pressures.

In addition to the triaxial compression tests for strength determinations, permeability tests were performed on large specimens under varying confining pressures to determine the k value with change in void ratio as well as to observe the degree of degradation with change in confining pressure. The need for inclusion of permeability tests was immediately apparent when the magnitude of degradation was observed from the initial shear specimens. A study of degradation was made for the purpose of isolating the effect of compaction, consolidation, and shear, and may be noted in Figures 1 and 2. The percent compaction as noted in the various figures is a percent of the maximum as established from impact effort and is the Corps of Engineers Military Standard 621 CE55 (AASHTO T180-57, Method D). For most soils, the California impact test, as performed according to Test Method No. Calif. 216, gives approximately the same values of optimum moisture and maximum density as the Corps of Engineers test.

Three types of triaxial compression tests were conducted. The majority of tests were the Q_u or unconsolidated undrained type, in which the specimens were sheared at predetermined molding moistures and densities on application of the confining or lateral pressure and without admission of any water. A limited number of tests designated as R modified were made to detect the possible increase in strength from consolidation before shear. No additional water was added to these specimens to gain saturation. The conventional R_u or consolidated undrained tests, were conducted on remolded specimens that had been saturated and consolidated before shearing. All three types of tests were conducted with closed systems in which no water was allowed to drain from the specimen during shearing action. Figures 1 and 2 show the field grading of the minus 3-in. and minus 1½-in. portions of the material. All specimens tested at lateral pressures between 15 and 125 psi contained minus 3-in. particle sizes. Between lateral pressures of 125 and 400 psi, the maximum particle size was minus 1½ in.

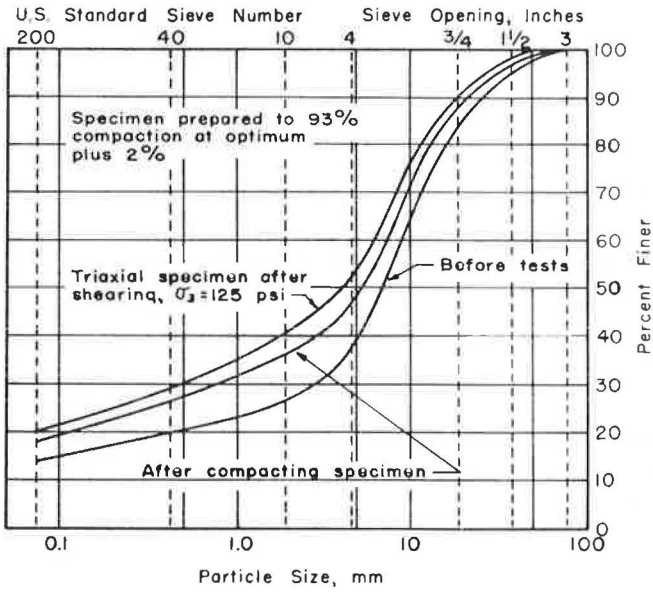


Figure 1. Particle size analysis of minus 3-in. material "before" and "after" tests.

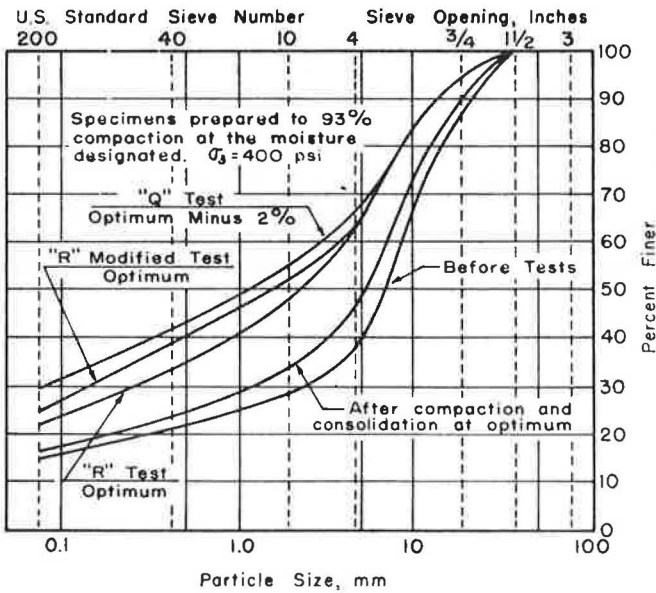


Figure 2. Particle size analysis of minus 1 1/2-in. material "before" and "after" tests.

The specimen size for minus 3-in. material was 12-in. diameter by 27.6 in. high and the minus 1½-in. material was tested in a 6-in. diameter by 13.8-in. high specimen. In the 12-in. diameter apparatus (2, 4), the pore pressure was measured at seven different locations along the central axis of the specimens. Five of the sensing points were within the specimen and one at either end. The minute coaxial cables to the transducers in the specimens were brought through the rubber membrane at the elevation of the transducer and a minimum of miniature cable was actually within the specimen. The cables were then lead through the base of the apparatus to a measuring console. The volume of each transducer was about 0.0015 cu ft and cylindrical in shape. In the apparatus used for the minus 1½-in. material at the higher lateral pressures, the pore pressure was sensed only at the ends of the specimen (6). Figure 3 shows the apparatus that accommodated the 12-in. diameter specimens.

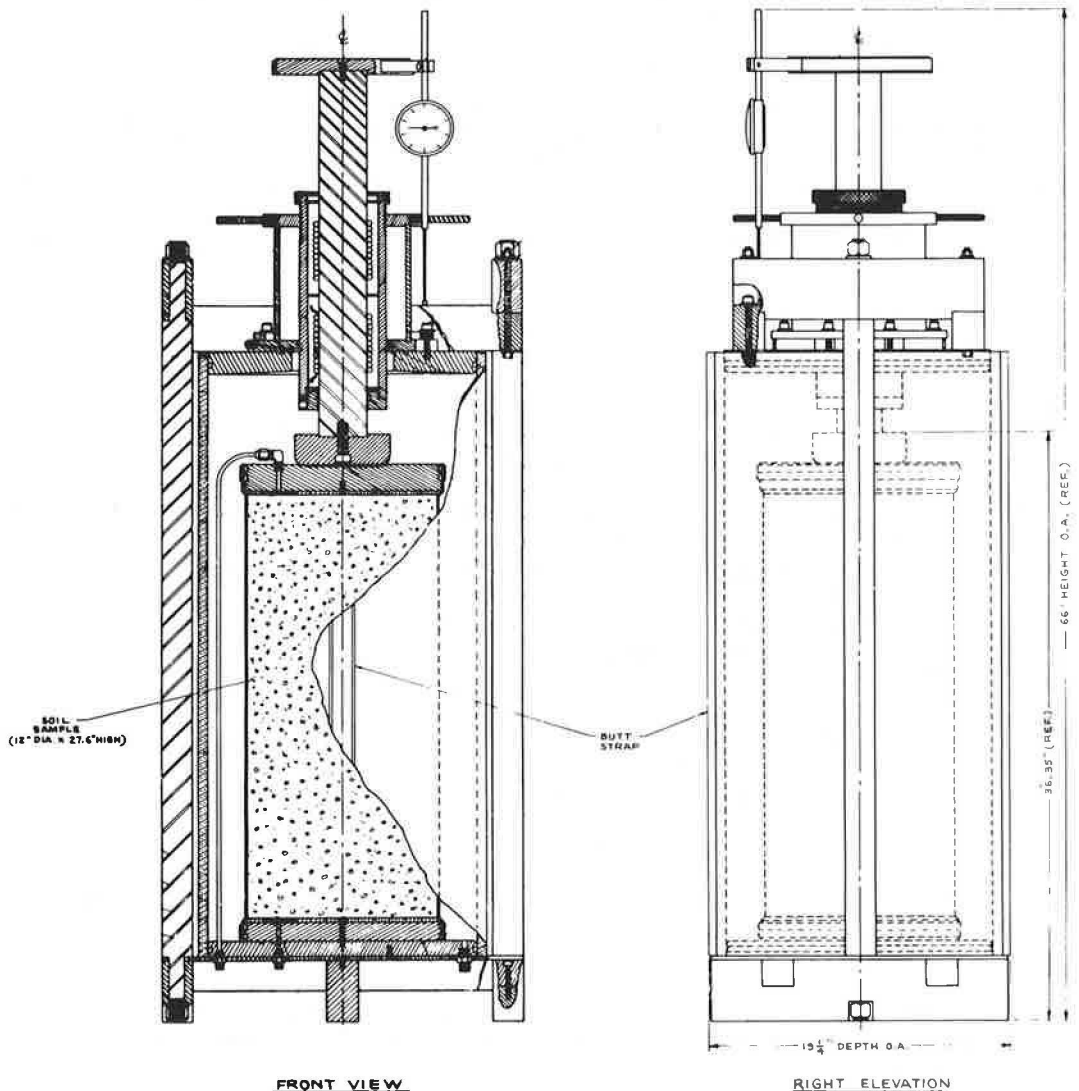


Figure 3. Large-scale triaxial apparatus.

All tests were performed under a controlled rate of strain. For the Q test, the rate was established by observing all of the pore pressure cells simultaneously to detect any development of a pressure gradient. The specimens were strained as fast as possible while still permitting the pore pressure to remain equal through the column of soil. This allowed strain rates varying between $\frac{3}{4}$ and 1 percent per minute. For all R tests, it was necessary to reduce the strain rate to about 0.2 percent per minute to eliminate the development of a pressure gradient. The test was stopped when both the maximum deviator stress and the maximum effective principal stress ratio had been reached. Volume changes during the shearing action were noted on pressure burettes connected to the water surrounding the specimen in the pressure chamber.

One of the principal difficulties experienced in large-scale and high-pressure triaxial testing is to fabricate membranes that will withstand high pressures and still bridge angular surface interstices without developing membrane restraints that are noticeably significant. On the specimens tested at the two highest lateral pressures in the 12-in. diameter apparatus, it was necessary to use double membranes. On several of the 6-in. diameter specimens, it was necessary to employ a series of overlapping polyethylene strips about $2\frac{1}{2}$ in. wide placed vertically between the two membranes. The thickness of the polyethylene strips was varied with the angularity of the material and the depth of the surface interstices.

Figure 1 shows the degradation results of a large-scale triaxial test performed with a lateral pressure of 125 psi. The large degree of degradation resulting only from compaction is somewhat the exception and not the rule. In Figure 2 it will be noted that the largest degree of degradation was attained for the specimen compacted 2 percent dry of optimum. This is in direct relationship to the magnitude of energy expended during the molding operations because the drier the material, the more effort is expended to meet a specific density. To demonstrate that degradation cannot be predicted with any degree of accuracy in a material of this type, it may be noted that the R modified test that was performed at placement moisture shows a greater degradation than the standard R test that was performed on a saturated specimen. It is, of course, impossible to separate the degradation due to compaction from that resulting from consolidation. It would appear, however, from observing the results in Figure 2 that about 10 percent of the gravel sizes (plus No. 4) was reduced to minus No. 4 particles when the permeability test at the 400-psi confining pressure was made. The permeability for a specimen molded to 93 percent compaction and at optimum moisture was 1×10^{-2} cm/sec or about 30 ft per day. After consolidation with a confining pressure of 400 psi, the permeability was reduced to 1.3×10^{-3} or about 3.5 ft per day.

The data in Figure 4 are presented to show the change in pore pressure with variation in placement moisture at comparable confining pressures. The figure further serves to demonstrate the magnitude of pore pressure when compared to a specific confining pressure. The percent compaction was the singular factor common to all specimens. The high pore pressure value for the R test with a confining pressure of 400 psi is not unexpected as it represents the only test that was saturated before shearing. In comparing the R modified test at optimum moisture and chamber pressure of 400 psi with the comparable Q test, it may be observed that the pore pressure is somewhat higher in the Q test (Table 1). This is a result of an appreciably larger void ratio at failure, which resulted in a dissipation of the pore pressure because both specimens had the same placement moisture content.

The Mohr failure envelopes for total stress and effective stress values are shown in Figures 5 and 6. The letter designation for the various envelopes is common to both figures and the test conditions for each envelope are given in Table 2. The envelopes were developed from a minimum of three tests and a maximum of five tests at confining pressures ranging between 15 and 400 psi. As anticipated, the highest strength envelope from the total stress plot was developed on materials prepared 2 percent dry of optimum and to 93 percent compaction. The lowest strength was at the lowest density investigated (85 percent compaction) and 2 percent wet of optimum. This produced a range of ϕ of 14 to 34 deg. The angles of the effective Mohr failure envelopes (Fig. 6) bracket a much smaller range of 30 to 38 deg.

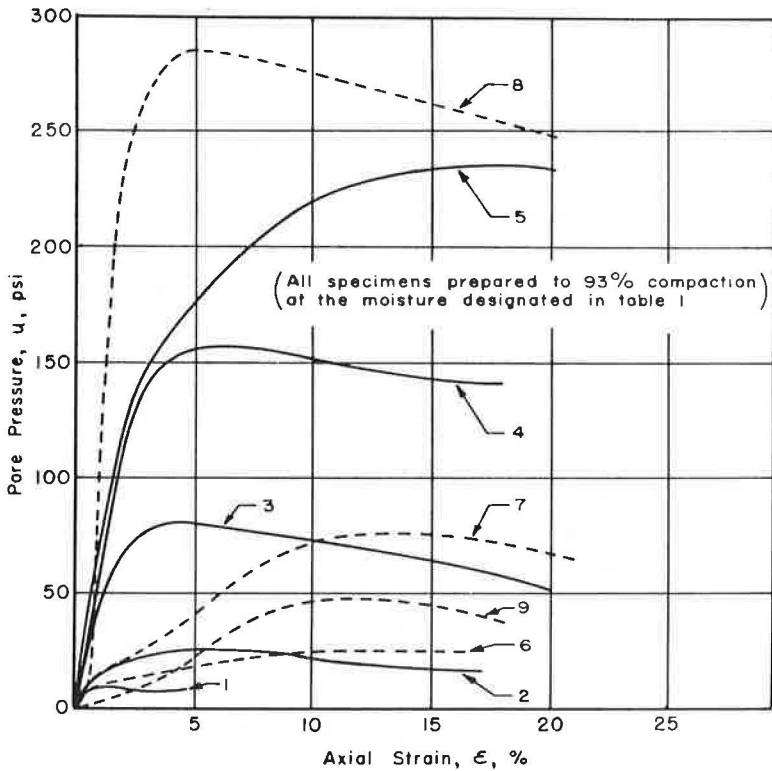


Figure 4. Plot of pore pressure and axial strain.

TABLE 1
TEST DATA FOR CURVES ON FIGURE 4

Curve No.	Type of Test	Lateral Pressure (psi)	Percent Compaction	Specimen Molding Moisture
1	Q	15	93	Optimum +2 percent
2	Q	60	93	Optimum +2 percent
3	Q	125	93	Optimum +2 percent
4	Q	200	93	Optimum +2 percent
5	Q	400	93	Optimum +2 percent
6	Q	400	93	Optimum -2 percent
7	Q	400	93	Optimum
8	R	400	93	Optimum
9	R (modified)	400	93	Optimum

TABLE 2
TEST DATA FOR FAILURE ENVELOPES ON FIGURES 5 AND 6

Envelope No.	Type of Test	Lateral Pressure (psi)	Percent Compaction	Specimen Molding Moisture
A	Q	400	85	Optimum +2 percent
B	Q	400	88	Optimum
C	Q	400	85	Optimum -3 percent
D	Q	400	93	Optimum +2 percent
E	Q	400	93	Optimum
F	Q	400	93	Optimum -2 percent
G	R (modified)	400	93	Optimum +2 percent
H	R (modified)	400	93	Optimum
I	R	400	93	Optimum

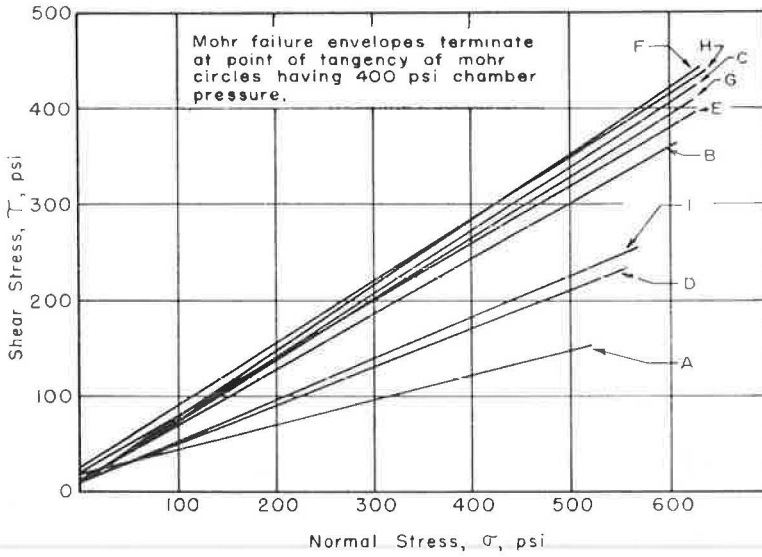


Figure 5. Failure envelopes for total stresses.

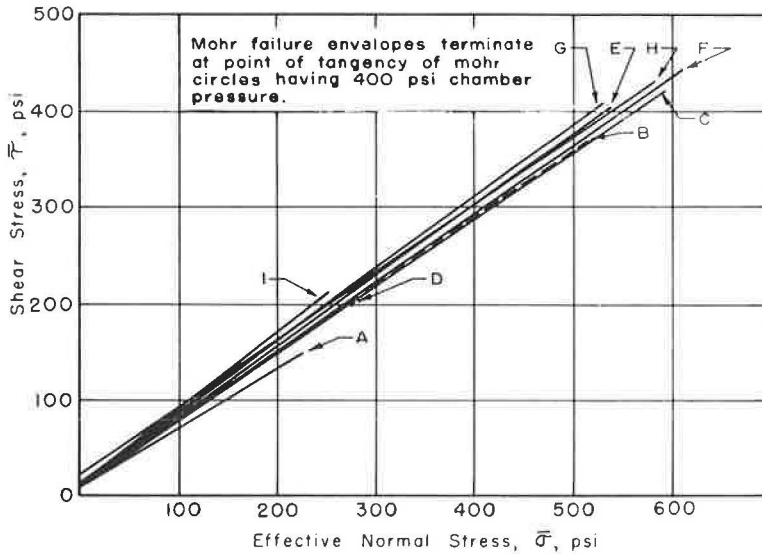


Figure 6. Failure envelopes for effective stresses.

DESIGN

In addition to this sampling and testing program, geologic studies were conducted and borings were made to further evaluate the material that would be available for construction of the 383-ft high embankments at Squaw Creek and to ensure that the testing program had included the available material. These studies consisted of geologic mapping, seismic surveys, and vertical and horizontal core and auger borings made in cuts in the vicinity of this embankment. From these data it was possible to determine roughly the percentages of the various types of material that would be available for embankment construction. The materials available could be classed in three general categories. The first category consisted of overburden and severely weathered material with a moderate to high percentage of clay as well as silt, sand, and gravel sizes. The second category consisted of somewhat weathered sandstone and shale of fair to good quality. The third category was primarily weathered and somewhat fractured and jointed sandstone.

Using the data available from this exploration and the testing program, a study was made of the possible zoning of materials in the embankment, and the stability of several typical sections was calculated. The following strength values, based on data from the testing program, were used in the various zones in the proposed section:

Zone	Cohesion (psf)	Angle of Friction (deg)	Percent Compaction
A	500	15	90
B	500	25	93
C (est. values)	0	35	95

Stability analyses were made with two computer programs that had been developed or modified for use on the IBM-704 electronic computer. It was evident from the borings and geologic investigation that there would be a shortage of the best quality material, that is, sandstone from the cuts; hence, the cross section of the sandstone portion of the proposed embankment was kept to a minimum that would still result in a stable embankment. The cross section for the embankment at Squaw Creek is shown in Figure 7.

Considerable selection of material from roadway excavation will be necessary to construct an embankment with the proposed cross section. This will necessitate long hauls and possibly stockpiling of material to ensure its placement at the proper location in the embankment.

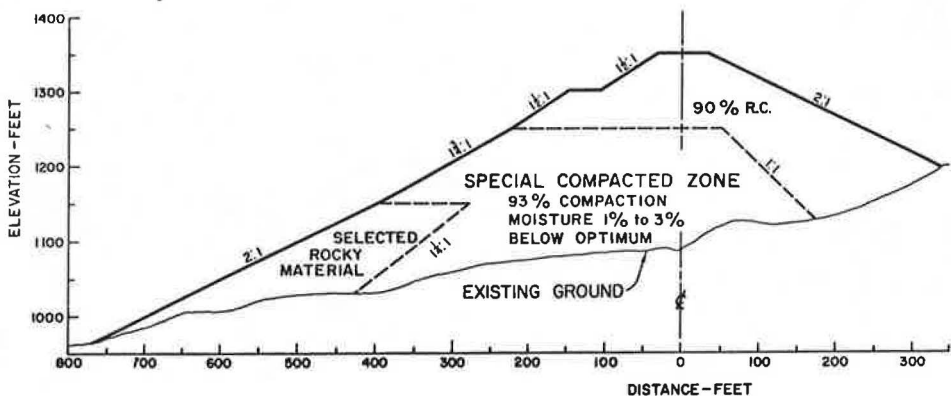


Figure 7. Typical section at Squaw Creek.

CONSTRUCTION

A \$6,000,000 contract for construction of the road in this area was awarded in June 1966 that included construction of an embankment with a maximum height of 383 ft across Squaw Creek. This embankment requires approximately $2\frac{1}{2}$ million of a total of approximately 3 million cu yd on the project. An aerial view of a portion of the project is shown in Figure 8 after the clearing and grubbing operations had been completed and a stabilization trench had been constructed in the bottom of Squaw Creek.

The specifications require the placement of selected material in Zones C and B. More rigid control of moisture content and higher relative compaction than is normally required is specified for construction of Zone B. Zone C consists of selected material and is the sounder and larger rock encountered in excavation of designated cuts. Likewise, the material for Zone B consists of selected rocky, granular material from designated cuts, and does not contain material that is normally classified as overburden nor does it contain an appreciable amount of shale, clay, soil, or vegetable matter. Zone B material is being compacted to a relative compaction of at least 93 percent, in lieu of the standard requirement of 90 percent, and at a moisture content of 1 to 3 percent less than optimum moisture as determined by the California impact test. (Relative compaction is defined as the ratio of the in-place density of a soil or aggregate to the test maximum density of the same soil or aggregate when compacted by a specific test method.)

This project is one of several on which nuclear gages are being used to determine relative compaction and in-place moisture of embankment material. In-place density is being determined by nuclear Test Method No. Calif. T-231 instead of the normal sand-volume method, which is part of Test Method No. Calif. 216.

The aerial view shown in Figure 8 reveals the ruggedness of the terrain through which this project passes. Most of the material is quite wet because of high groundwater table and springs. The average annual rainfall is about 70 in. and most of it falls between October and April. The existing road is well-known for its past history of

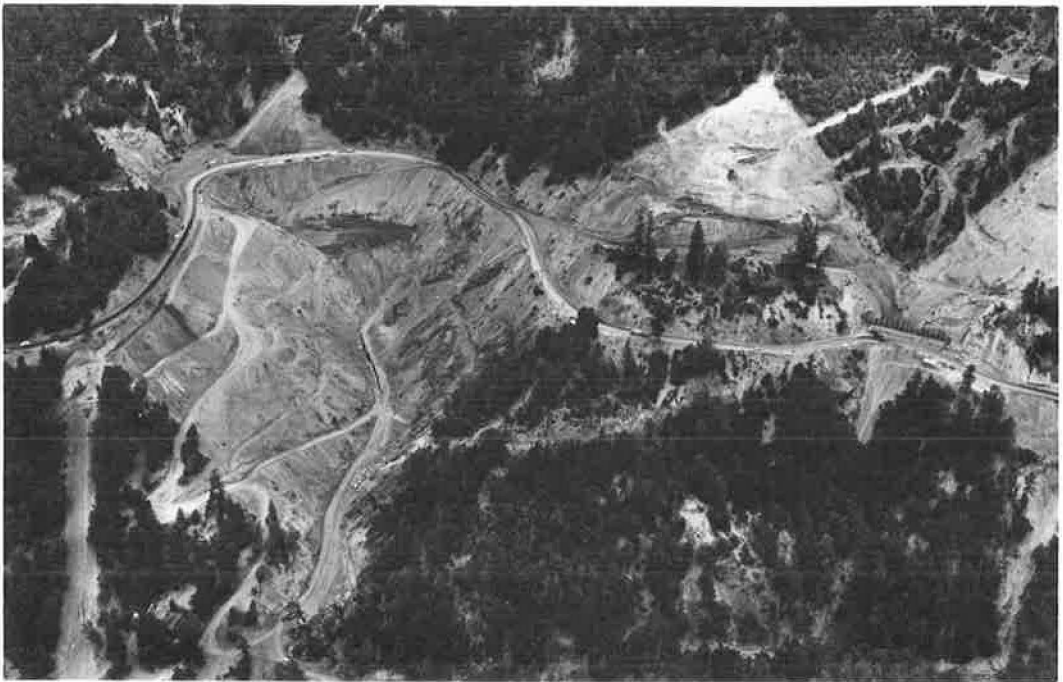


Figure 8. Aerial view after clearing and grubbing and stabilization trench construction at Squaw Creek.

landslides. Underdrains are being installed in all cut sections. Unsuitable material has been stripped from the embankment foundations and a 3-ft layer of permeable material placed beneath the embankments where needed. Supplemental funds in the amount of \$350,000 have been provided for possible slide removal and additional drainage work.

The time schedule provides for 300 working days with two winter shutdowns of approximately six months each. The estimated completion date was September 30, 1968. It is recognized that the time limit is insufficient for the contractor to accomplish the work by working the normal number of hours per day or week on a single-shift basis. The specifications require that additional shifts may be necessary to ensure that the progress of the work conforms to the progress schedule.

To observe the behavior of the embankment during and subsequent to construction, the embankment is being instrumented with settlement platforms, horizontal movement plates, strain gages, stress meters, and piezometers. These devices will warn the resident engineer of changes in conditions as the embankment is constructed. The locations of these devices are shown in Figure 9. The first level of devices near the bottom of Zone B were installed during September 1966.

Samples of the uncompacted material and compacted "undisturbed" samples from Zone B will be secured to perform other series of triaxial tests to check on the original design of the embankment.

This paper demonstrates the need for correlating sampling, exploration, and testing of a combination of soil and rock to a specific problem in engineering design and construction. It is believed that the information obtained from the types of special apparatus used and from the magnitude of the confining pressures employed will be of immediate value to other professional people in the field of soil mechanics.

ACKNOWLEDGMENTS

The authors are appreciative of the efforts of numerous employees of the California Division of Highways and the South Pacific Division of the U. S. Army Engineers in making this paper possible. They are especially indebted to A. W. Root, H. R. Cedergren, and C. B. Palmer for the planning, execution, and evaluation of the testing program.

REFERENCES

1. Gordon, B. B., and Hall, E. B. Triaxial Testing Using Large Scale High Pressure Equipment. Proc. on Laboratory Shear Testing of Soils, jointly sponsored by ASTM and National Research Council of Canada. Ottawa, 1963.
2. Hall, E. B. A Triaxial Apparatus for Testing Large Soil Specimens. ASTM Spec. Tech. Publ. 106, 1950, pp. 152-161.
3. Hveem, F. N. Maximum Density and Optimum Moisture of Soils. HRB Bull. 159, 1957, pp. 1-23.
4. Leslie, D. D. Large-Scale Triaxial Tests on Gravelly Soils. Proc. Second Pan-American Conf. on Soil Mech. and Found. Eng., Vol. 1, 1963, pp. 181-202.
5. Noell, O. A. Triaxial Shear Equipment for Gravelly Soils. Proc. Third Internat. Conf. on Soil Mech. and Found. Eng., Vol. 1, 1953, pp. 165-169.
6. Warlam, A. A. Recent Progress in Triaxial Apparatus Design. Research Conf. on Shear Strength of Cohesive Soils, Boulder, Colorado, ASCE, June 1960, pp. 859-876.

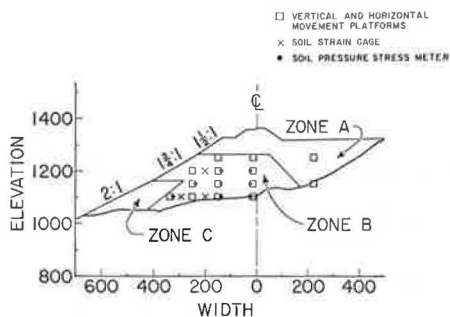


Figure 9. Typical section at Squaw Creek showing location of construction control devices.

BEHAVIOR OF HIGH EARTH EMBANKMENT ON US-101

Travis Smith and William F. Kleiman, Materials and Research Department,
California Division of Highways

Moisture and density requirements and zoning of three types of materials taken from roadway excavation were necessary for construction of a 383-ft highway embankment. Strength tests were performed on samples of the embankment obtained during construction to compare "as-built" strength with the strength values used in design. Compression within the embankment to date is on the order of 3 ft. Strength tests were performed on specimens measuring 12 in. in diameter by 27 in. high containing 3-in. maximum size particles. The maximum confining pressure was 400 psi. The triaxial test results obtained when subjecting a single test specimen to three increments of confining pressure compare favorably with the results when testing three separate specimens at different confining pressures. The materials used in construction proved to be stronger than assumed, thereby allowing a relaxation of the restriction on quality.

•IN THE north coastal region of California, US-101 traverses very rugged and unstable terrain. This terrain consists primarily of weathered sandstone and shale that are derived from the sedimentary rocks of the Upper Jurassic to Cretaceous age. The soils and rocks in this area constitute one of the largest masses of unstable material thus far encountered in highway construction in the State of California. The highway maintenance department and the traveling public have been aggravated for many years by numerous landslides and embankment slipouts that have closed the highway at times.

Planning engineers spent several years studying alternate alignments to determine the most feasible route for construction of a four-lane freeway with an all-paved section and design speeds of 60 to 70 mph.

To satisfy design standards of long radii curves and maximum grades of three percent, several embankments in excess of 250 ft in height were constructed. The embankment across Squaw Creek has a maximum height of 383 ft with variable side slopes ranging from $1\frac{1}{2}$:1 to 2:1.

This paper deals primarily with the construction and performance of the Squaw Creek embankment and is a sequel to the paper by Hall and Smith (1), which emphasized the problems associated with the design of high embankments that are built with normal roadway excavation. This paper describes strength parameters obtained during construction. Also included is a discussion of behavior of the embankment, pore pressures, settlement, and modification of design. A procedure for determination of strength parameters for more than one lateral pressure applied to a single test specimen is presented.

CONSTRUCTION

Construction of the project began in June 1966. A major portion of a \$6,000,000 contract consisted of placing approximately 2.5 million cu yd of roadway excavation in

the Squaw Creek embankment. Weather conditions in this construction area compel winter shutdowns of approximately six months each year. Approximately one-third of the embankment material was placed during the 1966 construction season. The remainder of the embankment, except for the structural section of the roadway, was completed during the 1967 construction season. The road was opened to traffic in late 1968. Since that time the road has functioned satisfactorily with no signs of distress appearing in the embankment.

Foundation for the embankment consisted of fairly good weathered interbedded sandstone and shale. Some surface weathering had occurred to the extent that removal was necessary. Most of the removal was made in the bottom of the rather steep-sided creek or canyon. Depths of removal in no case exceeded 20 ft. Material was stripped to expose somewhat better quality weathered sandstone and shales. Several seepage areas were exposed in the bottom of the creek as well as on the flanks of the canyon. A 3-ft layer of permeable material, 20 to 50 ft wide, was placed in the bottom of the creek. Projections of permeable material extended from this system to many seepage areas that were exposed or existed in the foundation area. A perforated metal pipe was placed in the permeable material in the bottom of the creek. This subsurface drainage system has produced large quantities of water throughout the history of the project and continues to flow at a fairly high rate, particularly in the winter. Total flows have ranged from a maximum of approximately 500,000 gal/day to a minimum in the late summer of 63,000 gal/day. Observations indicate that this system has effectively prevented the development of pore pressure in the lower part of the embankment or in the foundation materials. Some investigation was done during construction to determine if groundwater or pore pressures existed. Generally, this information appeared favorable. There were some indications of local pockets of perched water, but these were believed to be of minor consequence.

At the planning and design stages it was decided to transfer the surface water normally carried by the creek to a culvert to be installed relatively high in the embankment and on one of the slopes of the canyon. The culvert was to extend from the top of the area designated "fill for drainage" through the fill and would discharge on the natural ground rather than the side of the embankment. To accomplish this task, additional roadway excavation was deposited in the area designated as "fill for drainage." Thus, the surface water and water in the creek were handled with a culvert of relatively light construction in contrast with an exceedingly heavy culvert that would have been required had it been placed in the bottom of the embankment.

Settlement platforms were installed in the embankment near original ground and at 50-ft vertical increments during the two construction seasons. Units were also installed on the downhill slope of the embankment during the 1967 construction season. A typical section showing vertical movement platforms and other construction control devices is shown in Figure 1. Settlement data to date indicate the embankment has compressed or consolidated approximately 3 ft, and the foundation soils have settled approximately 1 to 2 ft. Most of this settlement occurred in a period of about 1 yr during construction (1966-1967).

The indicating units installed on the downhill slope of the embankment show horizontal movements on the order of $\frac{1}{2}$ to 1 ft and most of this movement occurred during the 1967 construction season.

Three general zones of material were used in the embankment. Figure 1 shows a cross section through the more massive portion of the embankment. Zone C was composed of the sounder and larger rocky material that was encountered in excavation of designated cuts and was relatively free of clay. No special compaction of this material was specified or required. The material, being relatively free of fines, compacted readily with heavy-duty hauling, spreading, and compacting equipment. Most of the material contained such a high percentage of plus $\frac{3}{4}$ -in. material that standard compaction tests were impractical. Zone B consisted of selected rocky, granular material containing no material normally classified as overburden and containing no appreciable amounts of shale, clay, soil, or vegetable matter. The gradings of the material tested for design are shown in Figure 2.

APPROXIMATE STATION 424+50
Road Ol-Men-101-83.8/88.3

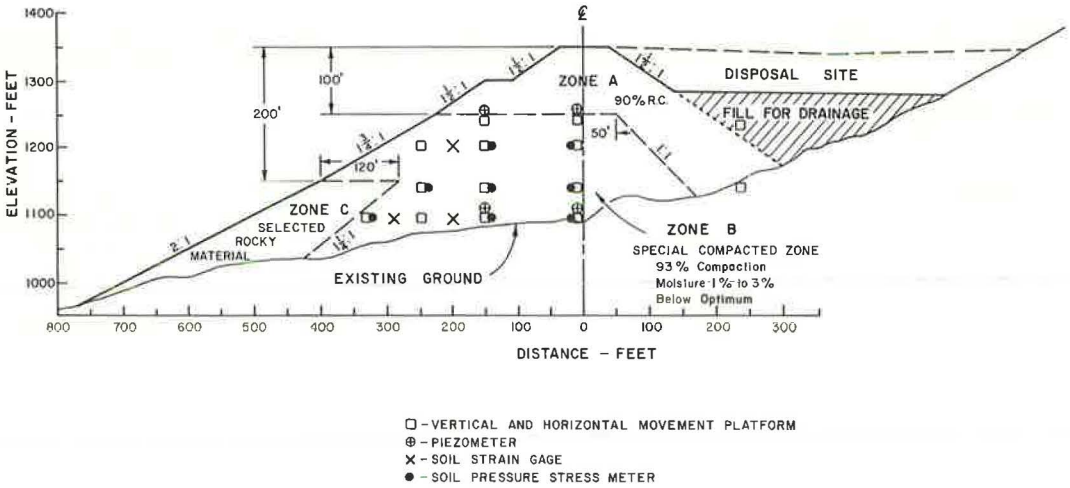


Figure 1. Typical section at Squaw Creek.

Specifications required that the Zone B material be compacted to 93 percent relative compaction. Test Methods Calif. Nos. 216 and 231 were used. The maximum density results from these test methods are comparable to results from AASHTO T-188. The Corps of Engineers, who did the testing for design, used the AASHTO test for determining maximum density. Specified moisture was 1 to 3 percent below optimum. Density requirements were met with reasonable compactive efforts. Some special efforts were

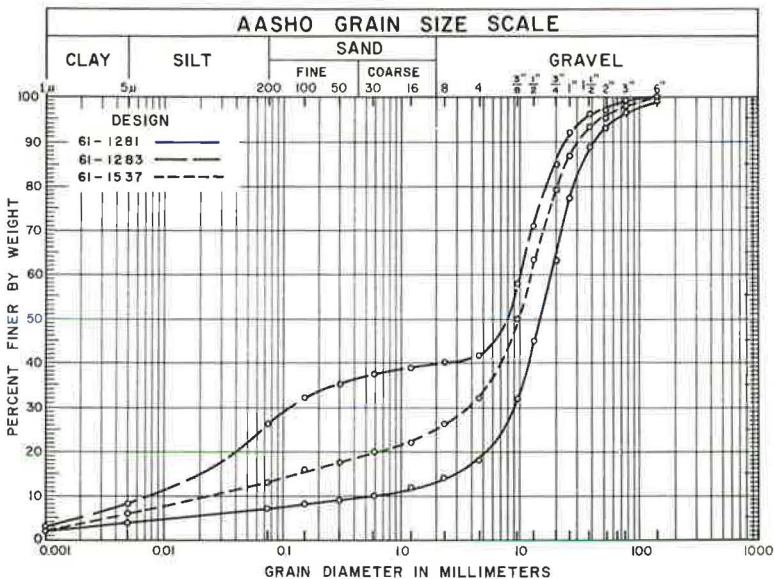


Figure 2. Mechanical analysis of material used in design.

required to lower the moisture content to the required level. Compaction and moisture requirements for Zone A material were in conformance with standard specifications for construction of California highways. The only moisture requirement contained in the California Standard Specifications for the construction of embankments states "the moisture content of embankment material shall be such that the specified relative compaction will be obtained." The normal compaction requirement is 90 percent relative compaction.

STRENGTH TESTS

The quantity of Zone C material was limited during the early months of construction. Visual inspection of material being placed in Zone B indicated that the material contained more clay than was anticipated during the design stage (Figs. 2, 3, and 4). Index properties of design samples are given in Table 1. The strength values used for design of the three construction zones are given in Table 2. Late in 1966 several large samples, approximately 2 tons each, were taken from the material being placed in the embankment. Gradings of these samples are shown in Figure 3. Based on visual observations, these samples were believed to be representative of the range in quality of material being placed. Test results from five of these samples are given in the left side of Table 3. This table also gives the results of tests performed on samples secured during the 1967 construction season. Grading curves of these samples are shown in Figure 4. A comparison of the strength test results (Table 3) and those used in design (Table 2) shows that the quality of the material being used in construction of both Zones B and C was slightly better than the values based on test results used for design. Shear strength of the Zone A material was consistently better than was anticipated. Consequently, restrictions on quality for materials in Zones B and C were slightly relaxed. It was possible to use material in these zones that was finer than was anticipated during design. Generally, the 1967 strength data show better quality material than was obtained in 1966. This is probably explained by the fact that, as the project neared completion, most of the material was being excavated from the lower portions of the cuts, and the quality of the material generally improved.

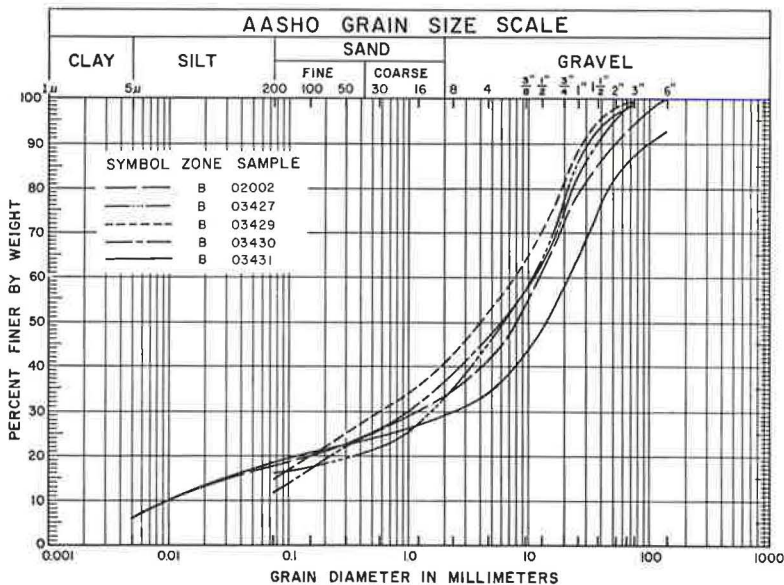


Figure 3. Mechanical analysis of material placed in embankment, 1966.

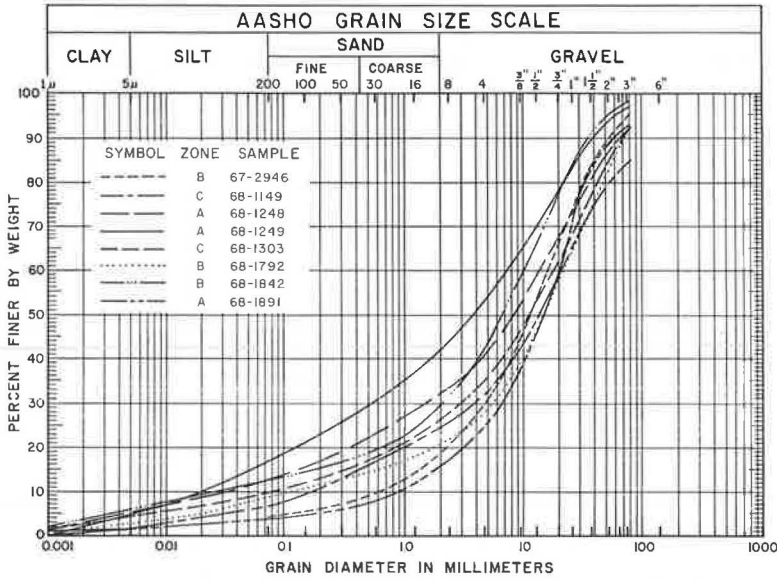


Figure 4. Mechanical analysis of material placed in embankment, 1967.

As a result of the favorable strength values obtained during construction and the satisfactory behavior of the embankment, it was agreed that unexpected slide material could be placed on the area designated "fill for drainage." This has been accomplished during the last 2 years subsequent to completion of the project. This area also served as a disposal site for excess material from additional nearby construction (Fig. 1).

TABLE 1
INDEX PROPERTIES OF PROPOSED EMBANKMENT SOILS

Description	Sample ^a		
	No. 61-1281	No. 61-1283	No. 61-1537
Identifying properties	Dark gray shale; very crumbly; breaks down readily on handling	Brown, highly weathered shale and sandstone; breaks down very readily	Gray sandstone and shale; appears rather durable, but also degrades; the best of the three samples
Liquid limit	45	28	28
Plastic limit	26	24	23
Plasticity index	19	4	5
Sand equivalent	22	14	20
R-value	33	40	81
Compaction (Mod. AASHO)			
Maximum density (pcf)	129.3	126.3	132.9
Optimum moisture (percent)	9.8	8.7	8.1
Strength data			
Effective stress			
Cohesion (psi)	5	11	20
Angle of internal friction (deg)	36	34	34
Total stress			
Cohesion (psi)	20	15	20
Angle of internal friction (deg)	28	33	33

^aAll samples compacted to 93 percent relative compaction at 2 percent less than optimum moisture.

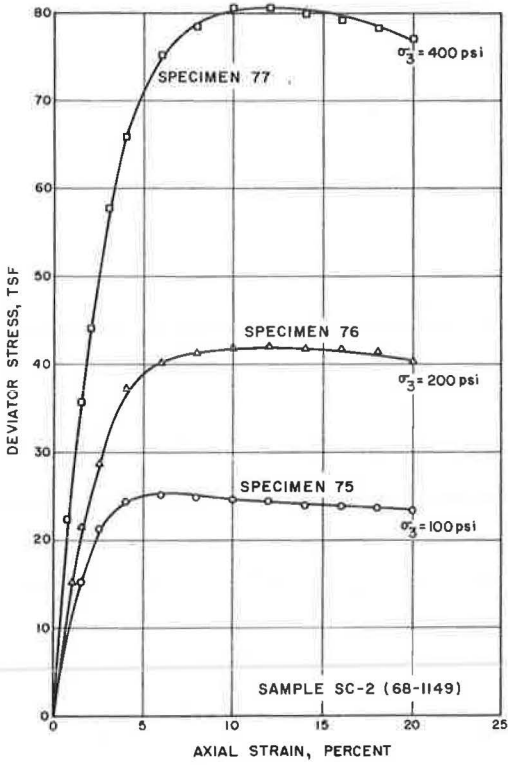


Figure 5. Stress-strain curves from conventional triaxial tests, typical Zone C material.

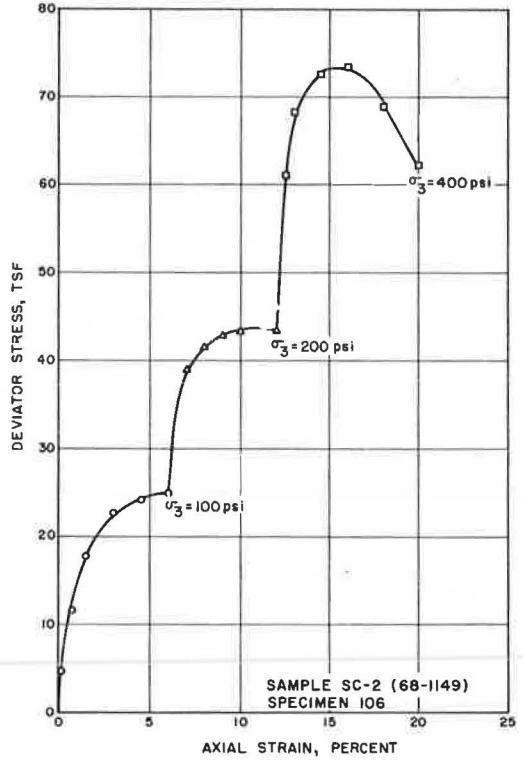


Figure 6. Stress-strain curves from multiple stage triaxial test, typical Zone C material.

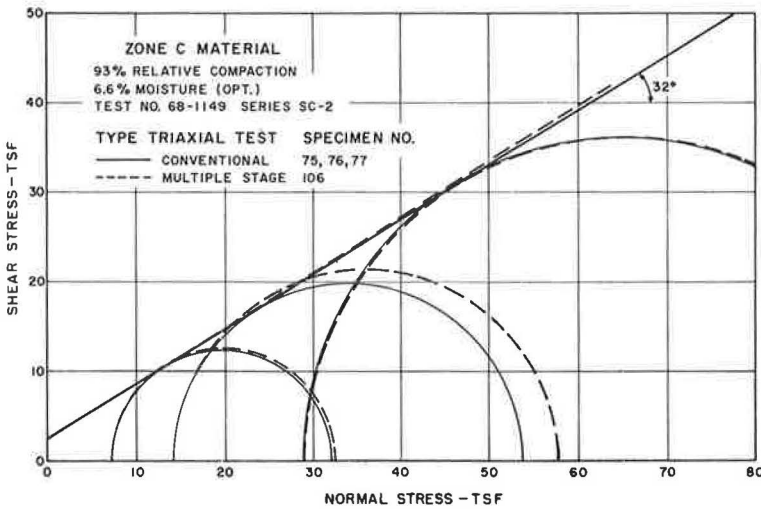


Figure 7. Comparison of Mohr's envelopes obtained with conventional and multiple stage triaxial tests, typical Zone C material.

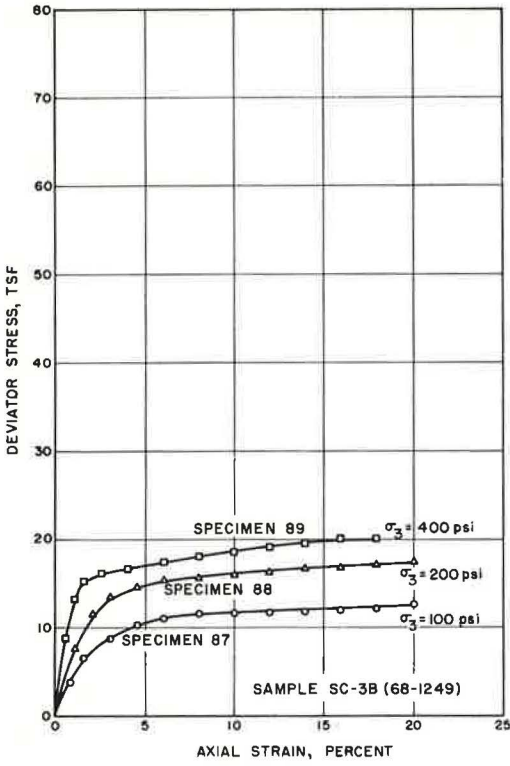


Figure 8. Stress-strain curves from conventional triaxial tests, weakest Zone A material.

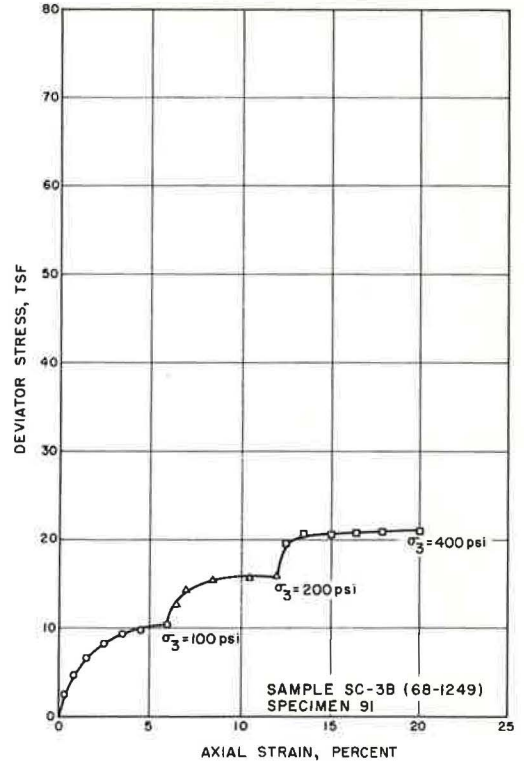


Figure 9. Stress-strain curves from multiple stage triaxial test, weakest Zone A material.

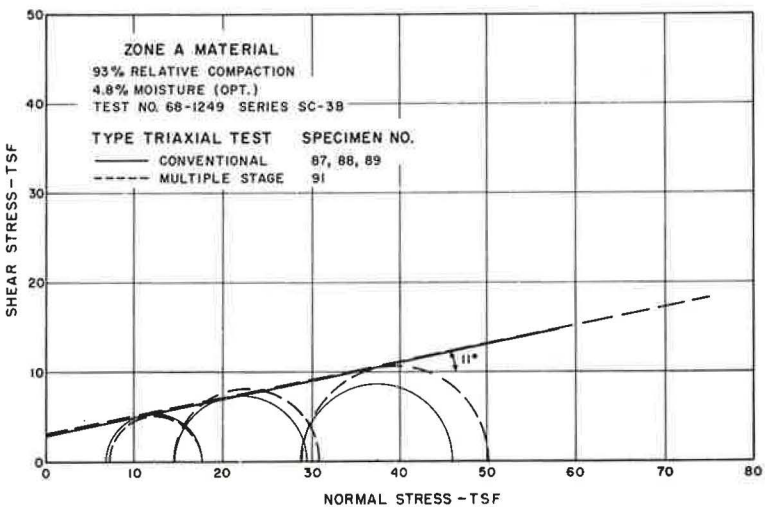


Figure 10. Comparison of Mohr's envelopes obtained with conventional and multiple stage triaxial tests, weakest Zone A material.

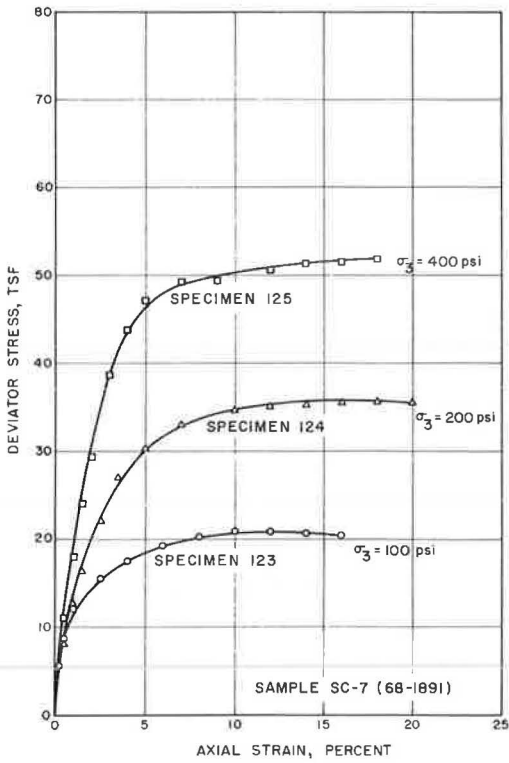


Figure 11. Stress-strain curves from conventional triaxial tests, typical Zone A material.

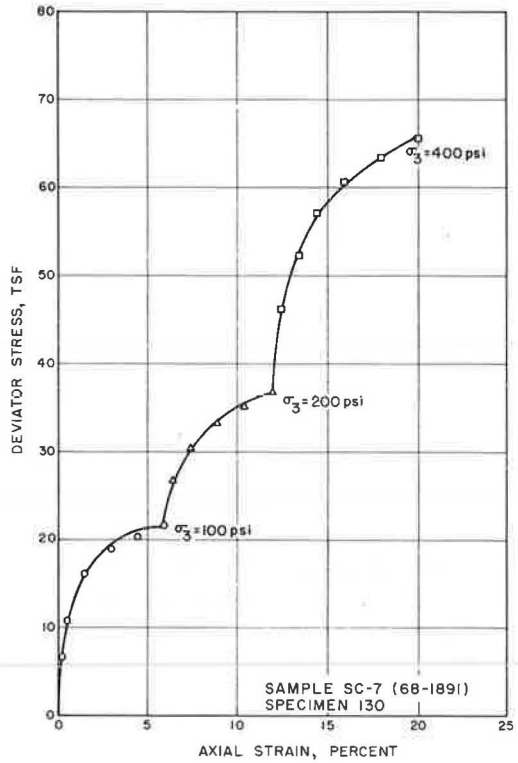


Figure 12. Stress-strain curves from multiple stage triaxial test, typical Zone A material.

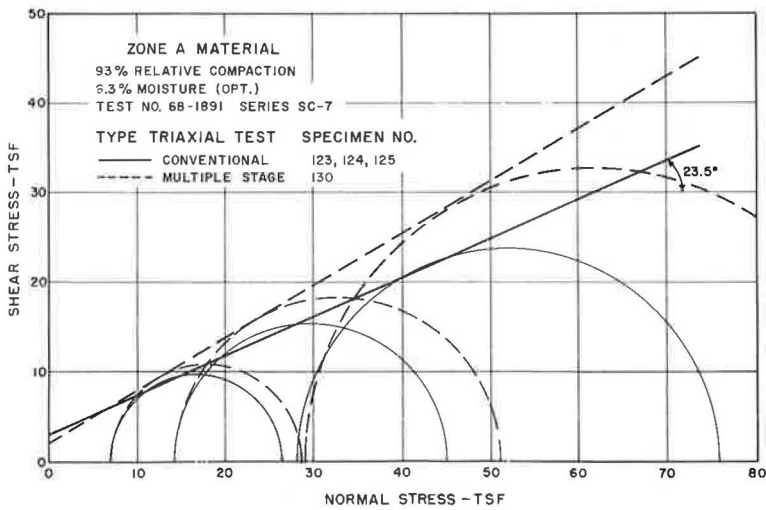
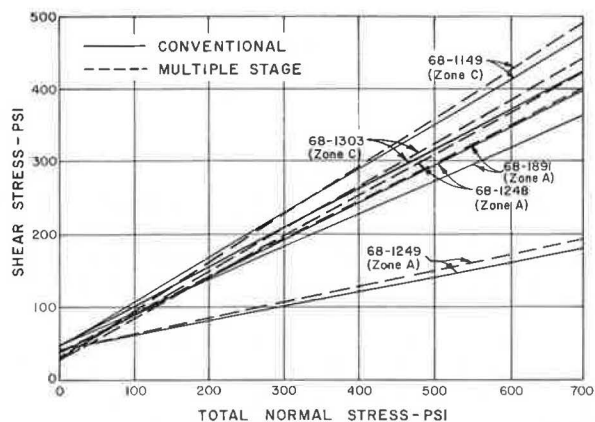
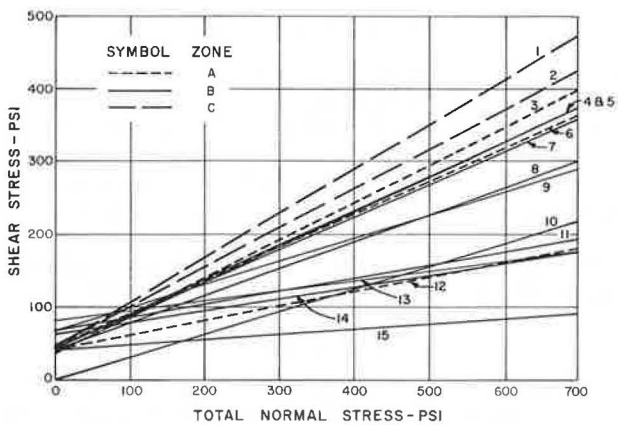


Figure 13. Comparison of Mohr's envelopes obtained with conventional and multiple stage triaxial tests, typical Zone A material.



TYPE TEST	COHESION (PSI)					ANGLE OF INTERNAL FRICT. (ϕ)				
	68-1149	68-1248	68-1249	68-1303	68-1891	68-1149	68-1248	68-1249	68-1303	68-1891
CONVENT.	45	35	42	45	45	31°	27°	11°	28°	24°
MULTIPLE STAGE	29	28	42	31	37	33°	29°	12°	30°	27°

Figure 14. Comparison of Mohr's envelopes obtained with conventional and multiple stage triaxial tests.



ENVELOPE	ZONE	C (PSI)	ϕ (DEG.)	TEST NO.
1	C	45	31	68-1149
2	C	45	28	68-1303
3	A	35	27	68-1248
4	B	42	25	68-1792
5	B	35	25.5	E
6	A	45	24	68-1891
7	B	43	24	67-2946
8	B	42	20	68-1842
9	B	69	17	F
10	B	0	17	C
11	B	69	10	68-1792
12	A	42	11	68-1249
13	B	83	7.5	5
14	B	63	9	68-1842
15	B	42	4	B

Figure 15. Comparison of Mohr's envelopes of materials sampled from different construction zones (conventional triaxial tests).

SUMMARY

The design studies for this project have been described (1). Construction of the project was accomplished during 1966 to 1968 using the controls established during design.

No serious problems were encountered during construction, and the facility has performed in a highly satisfactory manner since construction. A satisfactory installation for groundwater control was incorporated in the project. Rather large quantities of water have been removed by this installation. From observation it appears that hydrostatic pressures have not developed and groundwater has not constituted a serious problem.

During construction, various tests, including triaxial compression tests, were made to compare the design strengths with actual strengths being achieved during construction. Generally, the strengths achieved during construction were higher than had been predicted, based on tests made during design. Hence, some relaxation in the quality of material incorporated in the various zones was permitted. Selection of the material to be used in the various zones was based on visual observations, and changes were made by using material that appeared to be of slightly poorer quality than was originally intended for the various zones.

A novel testing technique was used for some of the triaxial compression tests. Rather than perform a test at a single lateral pressure for each specimen, tests were made using three different lateral pressures on a single specimen. The compressive load was increased to a predetermined strain or until evidence of incipient failure occurred. The confining load was then increased to the next increment, and the procedure repeated. Results of these tests indicate that, for this material and for the testing conditions used, this testing procedure produced results comparable to the normal test method where a single confining load is used for each specimen. The savings to be accrued by this alternate test method may prove to be substantial on future projects.

ACKNOWLEDGMENTS

The authors are most appreciative of the efforts of numerous employees of the California Division of Highways who made this manuscript possible. The construction of the Squaw Creek embankment was done under the supervision of District 01, Eureka, personnel.

Particular thanks are extended to District Engineer Sam Helwer; Resident Engineer H. W. Benedict; Materials and Research Engineer John L. Beaton; and Ben Zeiler for analysis of field and laboratory test data.

The opinions, findings, and conclusions expressed in this report are those of the authors and not necessarily those held by the Federal Highway Administration.

REFERENCES

1. Hall, E. B., and Smith, T. Special Tests for Design of High Earth Embankments on US-101. Presented at HRB 46th Annual Meeting and included in this Record.
2. California Division of Highways, Standard Specifications, July 1964.
3. California Division of Highways, Materials Manual, Testing and Control Procedures, Vol. 1.
4. Beaton, J. L. Embankment Testing With the Menard Pressuremeter. Interim Rept. M. and R. 632509-2, California Division of Highways, May 1968.
5. Beaton, J. L. Movement Within Large Fills, San Luis Reservoir, Relocation Project. Research Rept. M. and R. 632509-1, California Division of Highways, December 1966.
6. Beaton, J. L. Movement Within Large Fills, Ridge Route Project. Research Rept. M. and R. 632509, California Division of Highways, March 1969.

DETERMINATION OF STRESS DISTRIBUTION AROUND CIRCULAR TUNNELS USING CONFORMAL MAPPING TECHNIQUE

William E. Green, Industrial Engineering Division, SMMAE,
McClellan Air Force Base

The purpose of this paper is the application of complex variables to a special stress analysis problem. The resolved state of stress is in agreement with what would be expected from the physical geometry of the domain under investigation. The complete investigation is studied as a two-dimensional plane strain problem.

• THE INTENT of this paper is to present an illustrative method using conformal mapping to determine the state of stress surrounding two parallel circular tunnels due to internal pressure loading as shown in Figure 1. The tunnels are cut through an assumed homogeneous and isotropic engineering material that obeys Hooke's Law. The tunnels have parallel longitudinal axes with radii r_1 and r_2 , where r_1 is not equal to r_2 . The loading in each tunnel is assumed to be an arbitrary normal pressure acting around the whole circumference of the tunnel. To obtain a solution for the state of stress around the tunnels, the geometry of this space is conformally mapped into a finite transformed domain conducive to analytical solution as shown in Figure 2. The problem is then solved analytically in the finite transformed domain for the stress field. These stresses are summed up over arbitrarily small intervals of the transformed space to yield forces that are associated with specified points and directions.

The force vectors with their associative magnitudes, points of action, and directions are then transformed back into the original space to yield an array of oriented forces that are the resultant of the stress distribution in the investigative domain. Using the force array, the state of stress for the investigative domain is thus determined.

NOTATION

- a = a constant = 2.906;
- \bar{F}_1, \bar{F}_2 = vectors in the investigative and transformed domains;
- ID = investigative domain, Figure 2(a);
- $\lambda(\phi), \lambda(\theta)$ = intervals in the transformed and investigative domains respectively;
- p = centerline distance between two tunnels in Figure 3(c);
- P_1, P_2 = resultant forces obtained from stresses σ_R and σ_ϕ ;
- p_j = pressure at a given point or over a given area j ;
- R, ϕ = a given radius and angle in the annulus, Figure 3(b);
- TD = transformed domain, Figure 2(b);
- u, v = coordinates in the transformed domain, Figure 3(b);
- x, y = coordinates in the investigative domain, Figure 3(a);
- $\theta, a, r; q$ = angles and radii in the investigative domain, Figure 3(a);
- σ_R, σ_ϕ = radial and tangential stresses in annulus, Figure 5;
- σ_1, σ_2 = principal stresses in the investigative domain; and
- $\tau_{R\phi}$ = shearing stress in annulus.

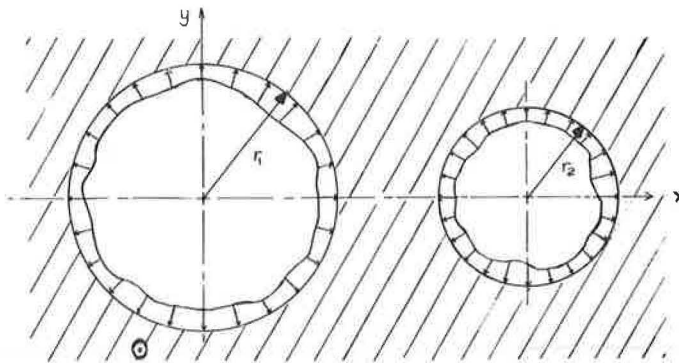


Figure 1. Investigative domain with arbitrary pressure loading.

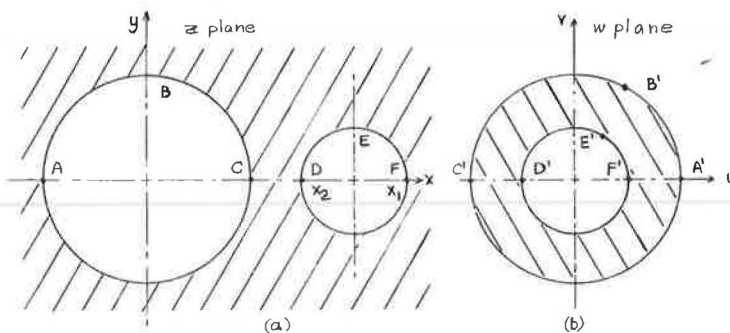


Figure 2. (a) Investigative domain, two-tunnel cross section; (b) transformed domain annulus.

PRELIMINARY CONSIDERATIONS

The determination of the state of stress for the problem with the configuration shown in Figure 1 is accomplished through the utilization of conformal mapping. The purpose of this particular example is to illustrate the technique. All coordinate systems used in this paper are two-dimensional.

To demonstrate the simplicity of the complex variable technique in the solution of the stress analysis problems, the following problem is investigated. Two tunnels of radii r_1 and r_2 ($r_1 \neq r_2$) are considered within an infinite homogeneous, isotropic, linear elastic material; they are subjected to normal loads (pressures) of arbitrary magnitude along their complete circumference. A stress distribution due to this loading is desired around the tunnels. A cross section of this configuration is shown in Figure 1.

The geometry in Figure 1 presents many difficulties that inhibit direct and reasonable solution of the problem leading to a description of the stress field in the domain of interest. Therefore, a conformal mapping transformation is sought that would conformally map the geometry described in Figure 1 into a more convenient geometric cross section that allows the determination of stress distribution over any area of interest.

From Churchill (1, Fig. 16, Appendix 2) the following transformation is written:

$$w = \frac{z - a}{az - 1}; \quad a = \frac{1 + x_1x_2 + \sqrt{(x_1^2 - 1)(x_2^2 - 1)}}{x_1 + x_2} \tag{1}$$

and

$$R_0 = \frac{x_1 x_2 - 1 - \sqrt{(x_1^2 - 1)(x_2^2 - 1)}}{x_1 - x_2} \quad (2)$$

where $x_2 < a < x_1$; $0 < R_0 < 1$ when $1 < x_2 < x_1$. (See Fig. 2 for a reproduction of Churchill's Fig. 16.)

From Figure 2 and Eq. 1 it is seen that the investigative domain can be mapped conformally into a convenient geometric cross section, i. e., an annulus. From Love (2, p. 144) it is known that the problem of the annulus subjected to boundary loading is readily soluble providing the loading on each boundary is self-equilibrating.

Consider the complex number

$$z = x + iy \quad (3)$$

where $i = \sqrt{-1}$. Equation 1 can be written as

$$w = \frac{(x + iy) - a}{a(x + iy) - 1} \quad (4)$$

Separating the real and the imaginary parts yields

$$w = \frac{(x - a)(ax - 1) + ay^2}{(ax - 1)^2 + a^2 y^2} + i \frac{(a^2 - 1)y}{(ax - 1)^2 + a^2 y^2} \quad (5)$$

or

$$w = u + iv = f_5(a, x, y) \quad (5a)$$

where

$$u = \frac{(x - a)(ax - 1) + ay^2}{(ax - 1)^2 + a^2 y^2} \quad (6a)$$

and

$$v = \frac{(a^2 - 1)y}{(ax - 1)^2 + a^2 y^2} \quad (6b)$$

From Figure 2(b) and Eq. 2 it is deduced that the condition

$$R_0 < \frac{1}{a} < 1 \quad (7)$$

must hold if the infinite point is to be included within the annulus, as assumed.

Choosing

$$r_1 = 1 \text{ and } r_2 = \frac{1}{2} \quad (8)$$

in Figure 1 and

$$x_1 = 3.5 \text{ and } x_2 = 2.5 \quad (9)$$

in Figure 2(b) and substituting these values into Eqs. 1 and 2 yields

$$a = 2.906 \quad (10)$$

and

$$R_0 = 0.06479 \quad (11)$$

At this point it is easy to check the reciprocal single-valuedness of the selected transformation.

Reviewing Figures 1 and 2, it is noted that all configurations are bounded by circles. Thus, for the sake of convenience Eq. 5 is transformed into polar coordinates.

In polar coordinates,

$$x = r \cos \theta \text{ and } y = r \sin \theta \quad (12)$$

for which Eq. 5 can be written in the form

$$w = \frac{(r \cos \theta - a)(ar \cos \theta - 1) + ar^2 \sin^2 \theta}{(ar \cos \theta - 1)^2 + a^2 r^2 \sin^2 \theta} + i \frac{(a^2 - 1)r \sin \theta}{(ar \cos \theta - 1)^2 + a^2 r^2 \sin^2 \theta} \quad (13)$$

or

$$w = f_6(a, r; \theta) \quad (14)$$

The following identities are noted in Figures 3(a), (b), and (c):

$$\theta + \beta + \gamma = \pi \quad (15)$$

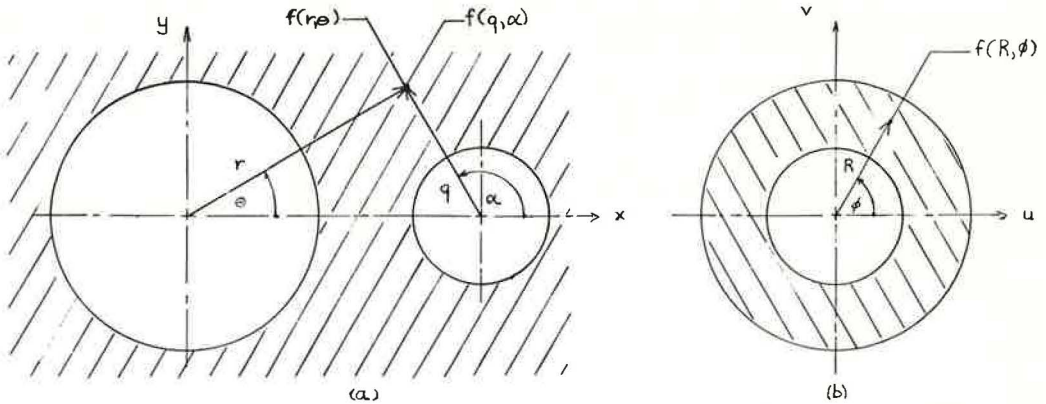
$$\beta = \pi - \alpha = \pi - \theta - \gamma \quad (16)$$

$$\frac{q}{\sin \theta} = \frac{r}{\sin \beta} \quad (17)$$

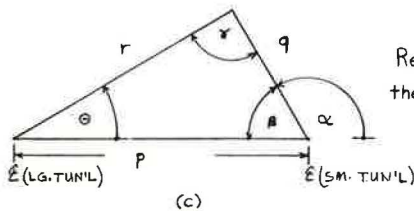
$$\sin \theta = \frac{q}{r} \sin \alpha = \frac{q \sin \alpha}{\sqrt{p^2 + q^2 + 2pq \cos \alpha}} \quad (18)$$

and

$$\begin{aligned} \cos \theta &= \frac{\sqrt{p^2 + 2pq \cos \alpha + q^2(1 - \sin^2 \alpha)}}{r} \\ &= \frac{p + q \cos \alpha}{\sqrt{p^2 + q^2 + 2pq \cos \alpha}} \end{aligned} \quad (19)$$



Relations Between Rectangular and Polar Coordinates.



Relations Between Center Lines of the Two Tunnels.

Figure 3. (a and b) Relations between rectangular and polar coordinates; (c) relations between centerlines of the two tunnels.

Substitution of Eqs. 18 and 19 into Eq. 13 yields

$$w = \frac{(p + q \cos \alpha - a) [a(p + q \cos \alpha) - 1] + aq^2 \sin^2 \alpha}{[a(p + q \cos \alpha) - 1]^2 + a^2 q^2 \sin^2 \alpha} + i \frac{(a^2 - 1)q \sin \alpha}{[a(p + q \cos \alpha) - 1]^2 + a^2 q^2 \sin^2 \alpha} \quad (20)$$

or

$$w = f_7(a, p, q; \alpha) \quad (20a)$$

For the following specific values,

$$r = 1.000 \quad (21a)$$

$$p = 3.000 \text{ and } q = 0.500 \quad (21b)$$

According to Kantorovich and Krylov (6, p. 36), "Any doubly connected region can be transformed, conformally and with reciprocal single-valuedness, into an annulus with the ratio of the radii of its bounding circumference finite or infinite." This suggests that the two-tunnel configuration [Fig. 2(a)] transforms conformally into the annulus [Fig. 2(b)].

Earlier the loading was defined as normal in direction, arbitrary in magnitude, and acting on the boundaries of the two tunnels in the investigative domain. The arbitrary

character of the loading on the boundaries is selected such that, when transformed into the annulus, it is self-equilibrating on each boundary. The loading on the boundaries of the investigative domain will also be selected so as to permit a convenient loading on the boundaries of the transformed domain.

The specific loading on the annulus (transformed space) is now chosen for ease of solution and for illustration of the technique. One of the most elementary cases of loading and one that yields a well-known elastic solution is that of uniform pressures. This particular case is covered by Wang (4, p. 54).

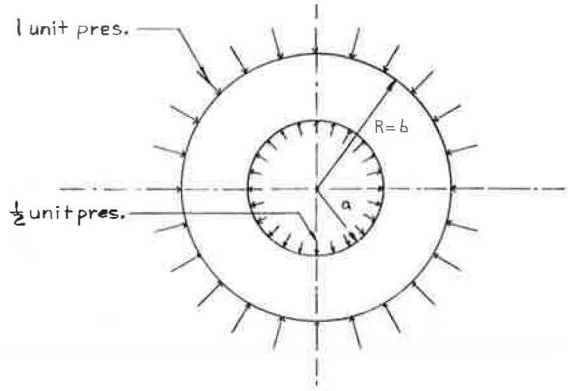


Figure 4. Annulus with loading pressures.

THEORETICAL ANALYSIS

The problem is to determine the state of stress surrounding the two tunnels shown in Figure 2(a). Conformal mapping functions are used to transform the given geometry into a geometry having known solutions. The stress field is calculated for the annulus acted on by the transformed loads, in this case assumed to be uniform pressure on each boundary. The stress values are then cast in suitable form (vectors) for transformation back into the investigative domain. The vector form satisfies the condition that requires invariance with respect to the original and transformed space.

The transformed domain is mapped with its associative, reciprocal, and invariant vector functions back into the investigative domain. Locations and lines of action of the force vectors are also mapped back to the investigative domain. The resulting stress field for the investigative domain is the solution sought.

The transformed domain consists of an annulus with internal and external pressures as shown in Figure 4. The following solution is taken from Timoshenko and Goodier (5, p. 58) with minor modifications. For the boundary conditions

$$\sigma_R = -p_i \text{ at } R = a \tag{22}$$

and

$$\sigma_R = -p_o \text{ at } R = b \tag{23}$$

the stresses are given by the expressions

$$\sigma_R = \frac{a^2 b^2 (p_o - p_i)}{b^2 - a^2} \frac{1}{r^2} + \frac{p_i a^2 - p_o b^2}{b^2 - a^2} \tag{24}$$

$$\sigma_\theta = \frac{-a^2 b^2 (p_o - p_i)}{b^2 - a^2} \frac{1}{r^2} + \frac{p_i a^2 - p_o b^2}{b^2 - a^2} \tag{25}$$

$$\tau_{R\theta} = 0 \tag{26}$$

where p_i = internal pressure, p_o = external pressure, a = inside diameter, and b = outside diameter.

Using Eqs. 24 and 25 in conjunction with the following values,

$$p_i = \frac{1}{2}, p_o = 1 \tag{27}$$

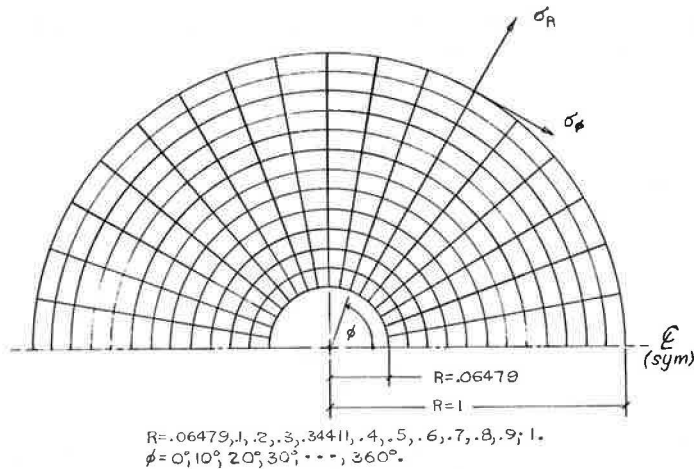


Figure 5. Radial lines and circular arcs superimposed on annulus (top half shown).

$$a = 0.06479 \text{ and } b = 1.00000 \quad (28)$$

the values for the radial and tangential stresses in the annulus can be calculated as given in Table I of the Appendix.¹ Figure 5 shows a network of radial lines and circular arcs. Stresses along the radial lines vary, whereas along the circular arcs these stresses remain constant.

In the following paragraphs the terms investigative domain and two-tunnel cross section with the terms transformed domain and annulus are used interchangeably [Figs. 2(a) and (b)].

Having obtained solutions for the stresses and their distributions in the annulus, it is now necessary to express them in a form that is invariant under transformation. It is known from the theory of vectors that a vector is such an invariant. To facilitate use of this principle, stresses in the annulus may be expressed by equivalent force vectors at a discrete number of points. An axisymmetric dimensional problem permits representation of the forces in the radial and tangential directions for a unit thickness as follows:

$$F_1 = \int_{\phi_1}^{\phi_2} \sigma_R d\ell = \sigma_R \ell(\phi) \quad (29)$$

and

$$F_2 = \int_{\phi_1}^{\phi_2} \sigma_\phi d = \sigma_\phi \ell(\phi) \quad (30)$$

where $\ell(\phi)$ is length. F_1 and F_2 are approximate values. The accuracy of F_1 and F_2 will increase as the value of $|\phi_2 - \phi_1|$ decreases.

¹This paper as originally prepared included an Appendix containing Illustrative Examples I and II, Tables I and II, and Computer Programs for Tables I and II. Because of space limitations, these have not been printed here. This Appendix is available in Xerox form from the Highway Research Board at cost of reproduction and handling. When ordering, refer to XS-36, Highway Research Record 345.

For convenience, each of the circular arcs in the annulus is divided into equal lengths as shown in Figure 5. It follows that

$$l(\phi) = \frac{\pi R}{18} \tag{31}$$

Substituting Eq. 31 in Eqs. 29 and 30 yields

$$F_1 = \frac{\pi R \sigma_R}{18} \tag{32}$$

and

$$F_2 = \frac{\pi R \sigma_\phi}{18} \tag{33}$$

F_1 is perpendicular to F_2 . Figure 6 is a graphic representation of these force vectors. Values for F_1 and F_2 are given in the Appendix.

Using Eqs. 32 and 33, σ_R and σ_ϕ values are summed along the contours and are defined as F_1 and F_2 . These forces are assumed located at the geometric center points of the intervals. This summation redefines the stresses as an array of forces having location, magnitude, and direction, as shown in Figure 6(b). It is possible to shift all F_1 and F_2 forces, located at the center point of the intervals, to the intersection points of the intervals. This rotation along the circular arcs is shown in Figure 7.

Each of the F_1 and F_2 forces has an associative point location and a directional angle. The force quantities are now written as, \bar{F}_1 and \bar{F}_2 , where the quantity is a vector. In the annulus there exists an array of force vectors located at the intersection of the radial lines and circular arcs. The point angle relationship is in general uniquely maintained under conformal transformation (6, Theorems 1 and 2, pp. 626 and 628). Consequently, the force vectors, \bar{F}_1 and \bar{F}_2 , after transformation maintain the same point-angle relationship that they held in the original space.

Writing the force vectors, \bar{F}_1 and \bar{F}_2 , in a general form for the annulus,

$$\bar{F}_1 = \bar{F} [P_1, f(u,v); \phi(u,v)] \tag{34}$$

and

$$\bar{F}_2 = \bar{F} [P_2, f(u,v); \phi(u,v) + 90^\circ] \tag{35}$$

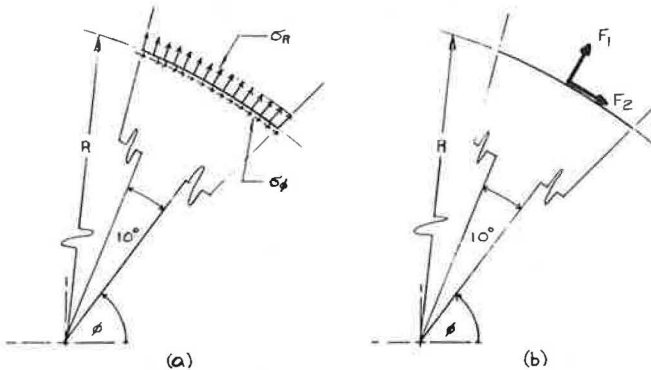


Figure 6. (a) Representations of σ_R and σ_ϕ acting along a 10-deg interval of an arc; (b) F_1 and F_2 force vectors acting through a center point of the interval of arc.

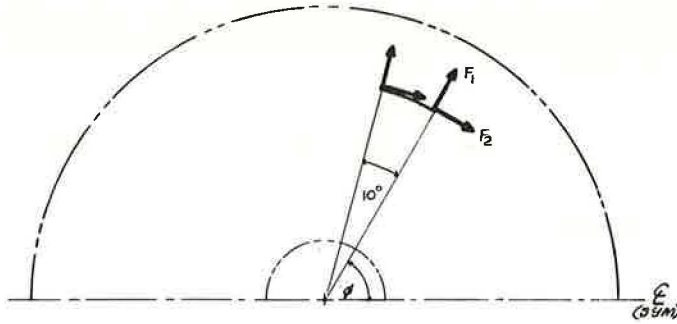


Figure 7. Transition of force vectors to intersection points on the circumferential curve.

where

$$P_1, P_2 = \text{resultant forces obtained from the stresses} \quad (36)$$

$$f(u,v) = \text{a nodal point through which } \bar{F}_1 \text{ and } \bar{F}_2 \text{ act in the w plane} \quad (37)$$

$$\phi(u,v) = \text{the angle between the line of action of } \bar{F}_1 \text{ and the u-axis of the w plane} \quad (38)$$

and

$$\phi(u,v) + 90^\circ = \text{the angle between the line of action of } \bar{F}_2 \text{ and the u-axis of the w plane} \quad (39)$$

It is observed that under transformation, Eq. 36 remains constant, while Eqs. 37, 38, and 39 undergo transformation. Conformally mapping Eqs. 37, 38, and 39, in a general form, into the original space (investigative domain) yields

$$f(u,v) \rightarrow f(x,y)$$

and

$$\phi(u,v) \rightarrow \psi(x,y)$$

where $f(x,y)$ and $\psi(x,y)$ define the nodal points and directional angles associated with the investigative domain. Consequently, a general definition of the transformed vector pair, \bar{F}_1 and \bar{F}_2 , in the investigative domain, is written as follows:

$$\bar{F}_1 = \bar{F} [P_1, f(x,y); \psi(x,y)] \quad (40)$$

and

$$\bar{F}_2 = \bar{F} [P_2, f(x,y); \psi(x,y) + 90^\circ] \quad (41)$$

where

$$f(x,y) = \text{a nodal point through which } \bar{F}_1 \text{ and } \bar{F}_2 \text{ act in the z plane} \quad (42)$$

$$\psi(x,y) = \text{the angle between the line of action of } \bar{F}_1 \text{ and the x-axis in the z plane} \quad (43)$$

and

$$\psi(x,y) + 90^\circ = \text{the angle between the line of action of } \bar{F}_2 \text{ and the x-axis in the z plane} \quad (44)$$

From Kantorovich and Krylov (3, p. 36), the principle of "reciprocal single-valuedness" is now invoked for the original transformation given by Eq. 1, in which z is written in terms of w to yield

$$z = \frac{w - a}{aw - 1} = \frac{(u - a)(au - 1) + av^2}{(au - 1)^2 + a^2v^2} + i \frac{(a^2 - 1)v}{(au - 1)^2 + a^2v^2} \quad (45)$$

Using the polar relationships,

$$u = R \cos \phi \quad (45a)$$

$$v = R \sin \phi \quad (45b)$$

Eq. 45 is now written

$$z = \frac{(R \cos \phi - a)(aR \cos \phi - 1) + aR^2 \sin^2 \phi}{(aR \cos \phi - 1)^2 + a^2R^2 \sin^2 \phi} + i \frac{(a^2 - 1)R \sin \phi}{(aR \cos \phi - 1)^2 + a^2R^2 \sin^2 \phi} \quad (46)$$

Equation 46 may also be expressed in the form

$$z = x + iy = f(a, R; \phi) \quad (47)$$

where

$$x = \frac{(R \cos \phi - a)(aR \cos \phi - 1) + aR^2 \sin^2 \phi}{(aR \cos \phi - 1)^2 + a^2R^2 \sin^2 \phi} \quad (48)$$

and

$$y = \frac{(a^2 - 1)R \sin \phi}{(aR \cos \phi - 1)^2 + a^2R^2 \sin^2 \phi} \quad (49)$$

Note that $R = |w| = \sqrt{u^2 + v^2}$ and $|z| = \sqrt{x^2 + y^2}$.

In the transformed domain each point of intersection is a nodal point associated with the vector pair, \overline{F}_1 and \overline{F}_2 , and the corresponding directional angles $\phi(u, v)$ and $\phi(u, v) + 90$ deg. Now invoking the principle of "reciprocal single-valuedness" it can be assumed that a similar relationship to that in the transformed domain will exist in the investigative domain. Therefore, in the investigative domain at each intersection point (x, y) there exist force vectors, \overline{F}_1 and \overline{F}_2 , with the directional angles $\psi(x, y)$ and $\psi(x, y) + 90$ deg.

Equation 46 can be written as

$$z = z_n(a, R; \phi) = z_n(x, y) \quad (50)$$

where n identifies a specific subset of transformed points selected from the annulus at a given radius R . Equation 50 yields a complete set of equations describing all transformed points of intersection (nodal points) as follows:

$$z_1(a, R = 0.06479; \phi = 0, 10, 20, \dots, 360 \text{ deg}) \quad (50a)$$

$$z_2(a, R = 0.1; \phi = 0, 10, 20, \dots, 360 \text{ deg}) \quad (50b)$$

$$z_3(a, R = 0.2; \phi = 0, 10, 20, \dots, 360 \text{ deg}) \quad (50c)$$

$$z_4(a, R = 0.3; \phi = 0, 10, 20, \dots, 360 \text{ deg}) \quad (50d)$$

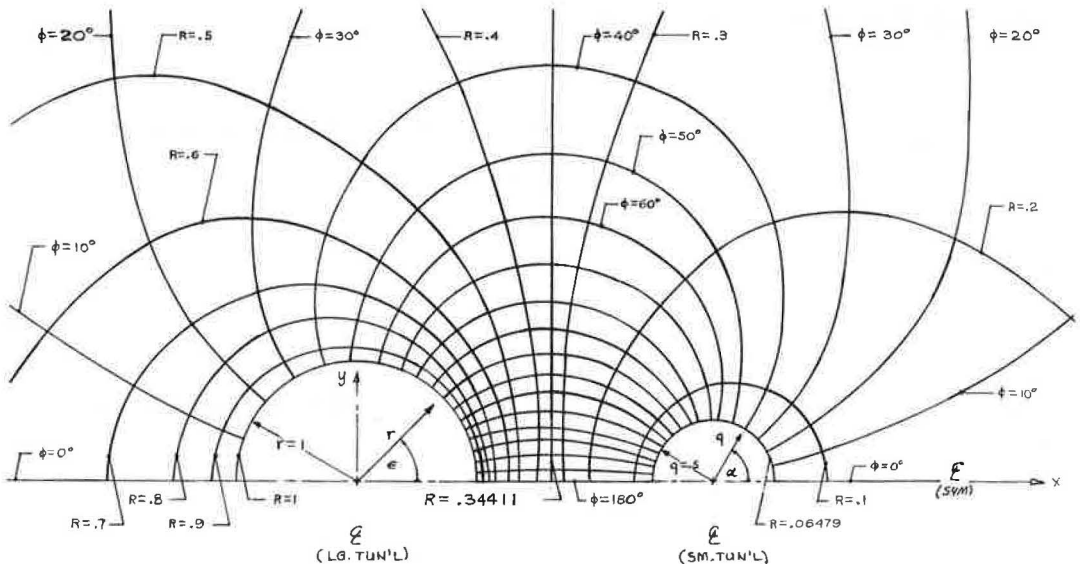
$z_5(a, R = 0.34411; \phi = 0, 10, 20, \dots 360 \text{ deg})$	(50e)
$z_6(a, R = 0.4; \phi = 0, 10, 20, \dots 360 \text{ deg})$	(50f)
$z_7(a, R = 0.5; \phi = 0, 10, 20, \dots 360 \text{ deg})$	(50g)
$z_8(a, R = 0.6; \phi = 0, 10, 20, \dots 360 \text{ deg})$	(50h)
$z_9(a, R = 0.7; \phi = 0, 10, 20, \dots 360 \text{ deg})$	(50i)
$z_{10}(a, R = 0.8; \phi = 0, 10, 20, \dots 360 \text{ deg})$	(50j)
$z_{11}(a, R = 0.9; \phi = 0, 10, 20, \dots 360 \text{ deg})$	(50k)
$z_{12}(a, R = 1.0; \phi = 0, 10, 20, \dots 360 \text{ deg})$	(50l)

This set of equations represents a map of the intersection points (nodal points) for the investigative domain. If the points defined by Eq. 50 are joined by a free curve, a map (as shown in Fig. 8) results that represents the transformed radial lines and circular arcs. The directional angles, $\psi(x,y)$ and $\psi(x,y) + 90 \text{ deg}$, may be obtained by determining the normal and tangent to the transformed circular arcs—R curves in Figure 8—at the point of interest. It may be of interest to note that the force vectors, \bar{F}_1 and \bar{F}_2 , act normal and tangential to the curves in both the investigative and transformed domains.

Figure 9 shows some typical vectors \bar{F}_1 and \bar{F}_2 located at various points of intersection in the investigative domain. Note: \bar{F}_1 is rotated 180 deg in direction at the transformed radial point $R = 0.34411$ defining the infinite point in the investigative domain. A complete picture of the loading apposite to the investigative domain will show \bar{F}_1 and \bar{F}_2 vectors located at each point of intersection in Figure 9.

In summary:

1. The stresses, σ_R and σ_ϕ , belonging to the transformed domain have been resolved into force vectors, \bar{F}_1 and \bar{F}_2 .
2. The magnitude, location and lines of action of the vector pair have been defined in the transformed domain.
3. The vector pair, \bar{F}_1 and \bar{F}_2 , have been transformed into the investigative domain in which their magnitude, location, and lines of action have been defined.



Notes:

1. x, y, r, ϕ, q and α indicate the Rectangular and Polar Coordinates relevant to the Investigative Domain.
2. R and ϕ indicate the Transformed Radial Lines and Circular Arcs

Figure 8. Transformed radial lines and circular arcs.

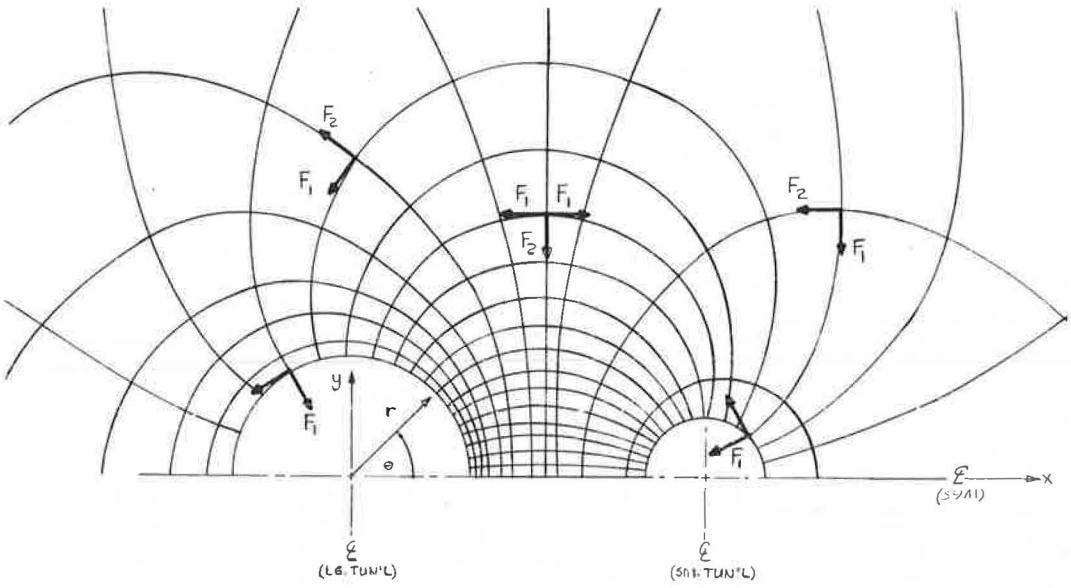


Figure 9. F_1 and F_2 shown at different intersection points in the investigative domain.

It is now possible to describe the stresses in the investigative domain. In the transformed domain the circumferential curves are divided into equal intervals for each given R (Fig. 5), and the stresses are summed over these intervals to yield the vector quantities, \bar{F}_1 and \bar{F}_2 .

Examination of Figure 8 reveals that the transformed intervals assume differing lengths.

Recalling Eqs. 29 and 30, and noting that

$$l(\phi) \rightarrow l(\sigma)$$

i. e., $f(\phi)$ yields $f(\theta)$ under transformation, the following expressions result:

$$\sigma_1 = \frac{F_1}{l(\phi)} \tag{51}$$

and

$$\sigma_2 = \frac{F_2}{l(\phi)} \tag{52}$$

In Eqs. 51 and 52, σ_1 and σ_2 are the principal stresses in the investigative domain, where

$$\bar{F}_{1,2} = |F_{1,2}| \tag{53}$$

and $l(\phi)$ is the corresponding interval length in the investigative domain.

In this case the principal stresses σ_1 and σ_2 act in directions normal and tangent to the transformed circular arcs, $R = R_1$, in Figure 8. It is known from the study of stress analysis that the state of stress at any point is completely determined by the magnitude and direction of the two principal stresses.

An approximation for $\ell(\theta)$ is obtained from

$$\begin{aligned} \ell(\theta) &= |z_m - z_{m+1}| + |z_{m+2}| + \dots + |z_{m+9} - z_{m+10}| \\ &= \sum_{k=m}^{m+9} |z_k - z_{k+1}| \end{aligned} \quad (54)$$

where z_k is defined by Eq. 50 with the following changes:

$$m = \phi = 0, 10, 20, \dots, 350 \text{ deg} \quad (55)$$

i. e., k indicates the actual degree value at which z_k is evaluated.

The accuracy of the principal stresses, σ_1 and σ_2 , in the investigative domain is dependent on the length $\ell(\phi)$.

Defining the polar coordinates for all points in the investigative domain, it follows that

$$r = |z| \quad (56)$$

and

$$\theta = \text{Arctan}(y/x) \quad (57)$$

where z , x and y are defined by Eqs. 46, 48, and 49 respectively. Consequently, the principal stresses, σ_1 and σ_2 , with associative polar coordinates may be determined.

The equations define x , y , r , θ , and σ_1 and σ_2 in the investigative domain at locations indicated in both rectangular and polar coordinates. Each coordinate location in the table represents the common point to the two adjacent intervals. The distance between any two consecutive points is written in the complex form $|z_j - z_{j+1}|$. In Appendix Table II, ℓ represents the approximate distance along the transformed curve between z_j and z_{j+1} . In the table, the principal stresses, $(\sigma_1)_j$ and $(\sigma_2)_j$, represent average values over an interval defined by (x_j, y_j) and (x_{j+1}, y_{j+1}) . The stresses σ_1 and σ_2 are taken constant over this interval ℓ . Also included in the table are the related values of R and ϕ indicating the location in the transformed domain. F_1 and F_2 are constant in both domains.

Two examples using Table II and Figure 8 are included in the Appendix.

Earlier, the investigative domain's boundary loading is defined arbitrarily. For convenience of calculation, the loadings selected in this paper are those that, when transformed to the annulus, permit easy solution and satisfy the condition of being self-equilibrating.

Consider first the case of the large tunnel (Fig. 8), $r = 1$. From Appendix Table II-L, the stresses σ_1 and σ_2 and the interval $\ell(\theta)$ over which they act are readily determined. Each interval $\ell(\theta)$ on the boundary of the large tunnel is a circular arc having a specific constant value of stress. It is assumed that a uniform pressure, p_j , acts on the outer boundary of each interval, equal in intensity to the stress, $(\sigma_1)_j$. It is noted that σ_1 acts normal to the boundaries, $r = 1$ and $q = 1/2$ in Figure 8. For the large tunnel the beginning and end points of the intervals are defined:

$$r = r_1 = 1.0 \quad (58)$$

and

$$\theta = \theta_1, \theta_2, \theta_3, \dots \quad (59)$$

The values of θ_j are given in Appendix Table II-L. At the boundary of the large tunnel $\theta(x,y) = \psi(x,y)$.

Consideration of the small tunnel leads to the same conclusions except that (a) the stress σ_1 and the interval $\iota(\theta)$ are taken from Appendix Table II-A and (b) the beginning and end points of an interval, z_j and z_{j+1} , are defined as follows:

$$q = q_1 = \frac{1}{2} \quad (60)$$

and

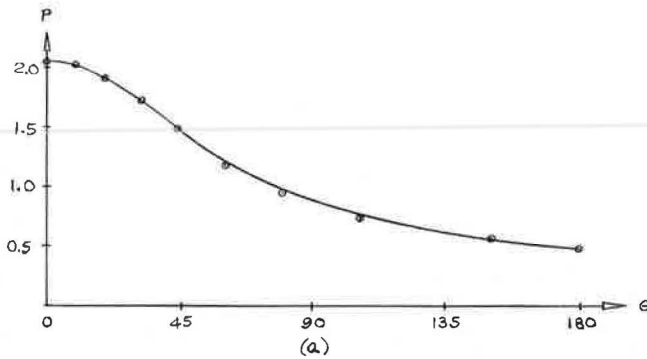
$$\alpha = \alpha_1, \alpha_2, \alpha_3, \dots \quad (61)$$

where

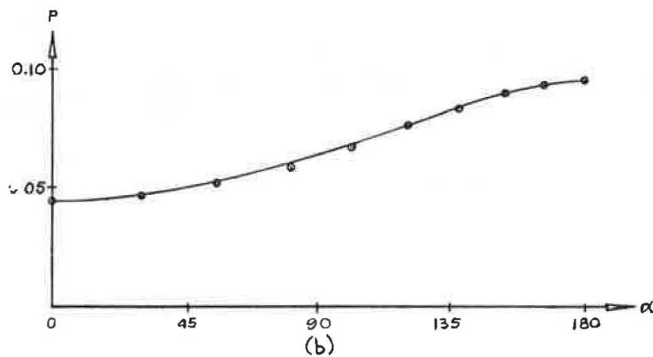
$$\alpha = \text{Arccos}(2x - 6) \quad (62)$$

in which x is determined by Eq. 48. At the boundary of the small tunnel $\alpha(x,y) = \psi(x,y)$.

Figure 10 shows a plot of the loadings on the top half of the boundaries of the two tunnels. Figure 10(a) is constructed by using σ_1 and θ values from Appendix Table II-L.



Pressure Loading on Boundary of Large Tunnel



Pressure Loading on Boundary of Small Tunnel

Note: σ_1 is Equal and Opposite to the Normal Pressure

Figure 10. Normal pressure distribution on the boundaries, investigative domain.

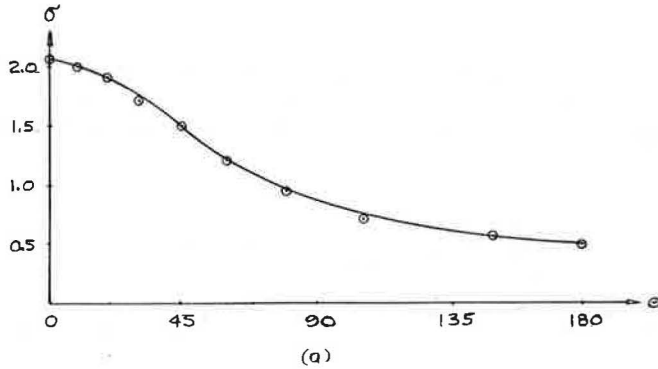
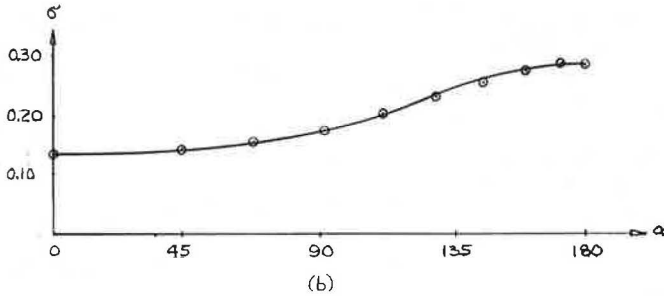
Principal Stress σ_2 on Boundary of Large TunnelPrincipal Stress σ_2 on Boundary of Small TunnelFigure 11. σ_2 distribution on the boundaries of the investigative domain.

Figure 10(b) is a combination of σ_1 and x values from Appendix Table II-A in conjunction with Eq. 62. Principal stress σ_1 is equal and opposite in intensity to the boundary loadings.

The distribution of the tangential stress σ_2 on the boundaries of the investigative domain is shown in Figure 11.

CONCLUSIONS

The intent of this paper is to illustrate a method by which the technique of conformal mapping is used as a vehicle in the determination of the state of stress surrounding the two tunnels as shown in Figure 1. In Appendix Table II, the principal stresses, σ_1 and σ_2 , with the associated intervals over which these values are considered constant, are given. The beginning and end points of the intervals coincide with the points of intersection on the transformed circular arcs. The actual path of the intervals can be determined analytically from the transformation equations.

Figure 8 shows the transformed radial lines and circular arcs in the immediate area surrounding the two tunnels. The path of the intervals is established graphically by tracing the path of the transformed circular arcs, i. e., the R-curves in Figure 8.

The principal stresses σ_1 and σ_2 act in normal and tangential direction respectively to the intervals $\ell(\theta)$.

The loadings on the two tunnels are segmented uniform normal pressures equal to the boundary stresses σ_1 given in Appendix Tables II-A and II-L. For instance, a uniform pressure p_j acts over the interval $\ell_j(\theta)$ associated with stress $(\sigma_1)_j$, such that

$$p_j = (\sigma_1)_j \quad (63)$$

where p_j acts uniformly over the interval $\ell_j(\theta)$ for which the stress $(\sigma_1)_j$ on the boundaries of the investigative domain is constant. Figure 10 shows a distribution of the loadings and σ_1 stresses on the boundaries of the investigative domain. Similarly, the distribution of σ_2 stresses on the boundaries of the investigative domain are shown in Figure 11.

Primary consideration in this paper is given to the technique of solution. For practical application of the results, consider Figure 10 and Eq. 63, from which loading diagrams for the tunnels can be constructed. These diagrams then determine the acceptable external load arrangement for the tunnels.

REFERENCES

1. Churchill, R. V. Complex Variables and Applications. McGraw-Hill Book Co., Inc., New York, 1960.
2. Love, A. E. H. A Treatise on the Mathematical Theory of Elasticity, 4th Ed. Dover Publications, New York, 1927.
3. Kantorovich, L. H., and Krylov, V. I. Approximate Methods of Higher Analysis. Interscience Publishers Inc., New York, 1958.
4. Wang, C. T. Applied Elasticity. McGraw-Hill Book Co., Inc., New York, 1953.
5. Timoshenko, S., and Goodier, J. N. Theory of Elasticity. McGraw-Hill Book Co., Inc., New York, 1951.
6. Wylie, C. R. Advance Engineering Mathematics. McGraw-Hill Book Co., Inc., New York, 1960.